Photonic devices in solitonic waveguides

Massimo Alonzo

SAPIENZA
UNIVERSITÀ DI ROMA

Dottorato di ricerca in Elettromagnetismo, Sapienza Universitá di Roma
Grade de Docteur en Physique spécialité optoélectronique de l'Université Paul Verlaine de Metz

PhD Thesis

Photonic devices in solitonic waveguides

Massimo ALONZO

Final discussion: 7 Mai 2010

Commission:

Roberta Ramponi	Professor, Politecnico di Milano
Ivo Rendina	Professor, I.M.M - C.N.R., Naples
Eric Louvergneaux	Professor, Université de Lille
Marc Fontana	Professor, Univesité de Metz
Delphine Wolfersberger	Professor, Supélec Metz
Eugenio Fazio	Professor, Sapienza - Universitá di Roma

Contents

Introduction

The always increasing amount of data exchanged for communication purposes, Internet and networks in general, requires technology to provide new solutions to reduce all the bottlenecks affecting the nowadays state of the art. For example, while many efforts have been done to carry informations using optical fibres (so in an optical way), it is still necessary to convert signals using an electronic device at its input and output endpoints. A laser, a transducer and routers must be employed. This represents a strong drawback that limits the real advantage of the fibre: to carry data at light speed from one user to another. Furthermore, considering the proper scale factor, this implies huge electrical power consumption. In fact, all the transducers, switchers and routers to address each data packet to the proper final user, require a power supply. To quantify this in numbers, an analysis done at Berkeley University states that the overall electricity consumption for servers in the world changed from 60 billion kW/h in 2000 to 130 billion kW/h in 2005. Clearly, this is just a statistics but it is evident that this trend cannot be sustained. The problem is so critical that research is required to move towards all-optical devices at any stage of the chain, so towards transparent optical networks.

The overall performance improvement that an all-optical device can provide, would be desirable for all the applications requiring for example high speed calculus, like numerical processing. The improvement would be huge, as operation time would be directly related to light speed instead of the speed of one electron moving into a wire with its resistivity. Is it possible to starts thinking to an all-optical computer processor?

This PhD thesis has been developed following the basic idea of realizing a circuit based on all-optical single elements having functionalities and performances that a classic electronic one cannot provide. So, in the following, solutions for such a circuit will be proposed. I will analyse in details inte-

grated sources at infrared (third windows for telecommunications) and blue wavelengths, interconnections and optical switchers (as signal elaboration device).

Actually, these structures have already been realized but only close to a proper substrate surface and with techniques which are very expensive because of the many and complex processes that must be applied. The element of novelty that will be introduced with this thesis is the use of nonlinear optics as a tool to write photorefractive spatial solitons and photorefractive soliton waveguides. Such new approach would overpass all the limitations that restrict the applicabilities of more standard waveguide fabrication technologies.

With "soliton" it is intended a beam propagating inside a medium in which compensation of broadening in space and time is achieved, as a consequence of light interaction with the material. In other words it is the light itself that modifies the material properties to compensate its spatial diffraction and temporal dispersion.

In the following I will refer only to the spatial diffraction compensation so to spatial solitons.

Once self-diffraction compensation is completed, a (bright) spatial soliton will leave a waveguide written in the material and its durability is function of the material relaxation time.

In the first chapter, the photorefractive origin and properties of these waveguides (or interconnections) will be discussed also in comparison to the other physical mechanisms that can originate other kind of spatial solitons and that are not suitable for this thesis purposes. Interconnection formation is analysed in details with reference to one of the most promising photorefractive materials, lithium niobate. I have been working with spatial solitons in lithium niobate since the beginning of my Master degree thesis and during this period I investigated their realizability and properties in function of wavelength, injected power and input waist, providing a full characterization about them.

Here an optical circuit realization is proposed, consequently other aspects must be considered, first of all optimization for light propagation.

In collaboration with the University of Besançon, the combined effects of light polarization and material anisotropy on light confinement have been considered, both experimentally and numerically. In fact, up to this moment, light propagation along the two directions perpendicular to the $\hat{c}$ axis was considered equivalent for self-confinement purposes. In the following,

I propose experimental and numerical investigations about this aspect in function of the injected light polarization to determine if some combinations can provide better performances.

Once a waveguide has been written, it provides peculiar properties for the beam propagating inside it. In fact, its undiffracted and solitonic nature can be used to create an integrated emitting source. In the following, two solutions will be presented, one for a lasing device in the third window for telecommunications (chapter 2) and one for the blue region (chapter 3).

In the second chapter, lithium niobate volume doping with erbium ions is taken into consideration. These ions are interesting as they can be used for infrared laser realization. Solitonic waveguides will be employed to improve lasing performances. Solitonic waveguiding in erbium doped media were never studied before, so doping effects on the main photorefractive parameters of lithium niobate is investigated. The extraordinary electro-optic coefficient and the photovoltaic field will be analysed as well as the beam self-confinement in function of erbium concentration and for injected light wavelengths not resonant with erbium absorption transitions. Finally, erbium ions will be directly excited and soliton formation will be studied also in these conditions.

In the third chapter, second harmonic generation from a near infrared beam is considered to achieve a blue radiation source inside such guides that improve conversion efficiency. As element of novelty, this will be done in lithium niobate. The emitted blue radiation will be used to write solitonic waveguides that trap also the fundamental beam which would not be able to directly induce a refractive index contrast. Physical properties about the generated second harmonic beam with reference to the fundamental one will be investigated.

To complete the “circuit”, in the fourth chapter, a solution to realize an all-optical router will be presented. The problem in this case is to dynamically reconfigure beam geometry at high speed rates.

To increase the overall speed for signal switching, a different photorefractive material is used: indium phosphide doped with iron ions. It is a semiconductor sensitive to the third window frequencies and it provides a response to an optical beam in a time of the order of micro-milliseconds. Firstly, the material and the photorefractive process inside it will be discussed. The latter differs from what previously shown for lithium niobate as a consequence of the presence of two free carriers and the influence of temperature too. Then the photorefractive interaction between two coherent

parallel beams will be investigated. The influence of light intensity, temperature and mutual distance will be taken into account both for the repulsion and fusion cases, corresponding to the out-of-phase and in-phase conditions, respectively. These measurements have been performed at 1.064μm to work in a regime for which material absorption is stronger in order to enhance the photorefractive response.

At the end of this thesis, finally, measurements that are not directly related to my PhD main topic are added in form of papers. They regard Z-scan measurements about the nonlinear (Kerr) refractive index in GaN and nonlinear absorption in Zinc-phthalocyanines.

Chapter 1

Solitonic waveguides as optical 3D interconnections

To satisfy the necessity of transmitting/elaborating data at speed rates that electronic devices grant but at the price of an always increasing power consumption, research activity is trying to move towards integrated all-optical devices. Structures like beam splitters, electro-optic or acousto-optic modulators, logical ports, laser sources, just to cite some example, have been successfully integrated on dielectric substrates. In order to make all of them work in the same circuit, the very first "brick" is the realization of an interconnection between them.

Such interconnections must propagate the light from one device to an another, like for example from a source to an elaborating one that must manipulate the information contained in the beam. To propagate such an optical signal, a waveguide is necessary and thus a good interconnection is provided by an optimized waveguide.

Waveguide state of the art up to nowadays is characterized by the necessity of surrounding a dielectric material with another one having a lower refractive index and thus allow the propagation of light by total reflections inside them. Although the basic idea is quite simple, these structures are affected by many drawbacks which can be divided in two categories according to performance issues and realization costs.

All the integrated waveguides available in the market are realized just on the dielectric material surface or few tens of micron below it. According to the realizative technology, they present light propagation and electro-optic

properties which can be very different. Common guiding structure realization requires extremely expensive ($\simeq 10^6$\$) tools and machineries besides the involved tricky chemical/technological processes. An exception is provided by the silicon-based technology. Thanks to its extensive use in electronics, integrated waveguide realization costs can be lowered by order of magnitude and complex guiding structures characterized by very low propagation losses can be achieved. In any case, the surface limitation cannot be overpassed and because of silicon gap energy ($\simeq 1.11$eV@300K), these guides are suitable only for infrared radiation propagation.

An example about the production of a planar or channel waveguide over a substrate is the layer over layer growth which can be obtained either by deposition or by epitaxy. While the first one is characterized by the deposition of a film over a substrate (whose refractive index is slightly lower than the film one), epitaxy is based on the growth of one or more crystalline layers of different materials having lattice constants similar to the substrate one. These layers are grown with very controlled thicknesses, good crystalline uniformity and doping profiles as well. In order to grow a layer over another, many approaches have been used, for example: chemical vapor deposition (CVD), vapor or liquid phase epitaxy (VPE and LPE respectively) etc....

One of the more employed substrate is lithium niobate, as it provides a strong electro-optic response besides many other nonlinear properties. Because of these reasons, in the following sections this material will be analysed in details.

To create waveguides extending few microns below the substrate surface (so 3D structures), typical methodologies successfully employed in lithium niobate are titanium indiffusion [1, 2] and protonic exchange ones [3]. The latter is preferred when the optical damage (i.e. photorefractive effect) must be reduced. Both of them rely on the necessity of photolitographing the wanted geometry over the substrate.

Photolithography allows to write a "map", the desired guiding structure design, on the employed substrate. This procedure is accomplished by "spinning" the substrate surface with a chemical light-sensitive material called "photoresist", which is then shaped or via an ultraviolet source or an electron beam. By etching the photoresist, or chemically or via a "dry" methodology, the desired geometry remains written.

To make titanium diffuse into the substrate, the application of a high temperature (in the order of $1000 - 1300°$C) is required. This technique

provides some benefits like the linear increasing of the extraordinary refractive index in lithium niobate without altering the electro-optic and nonlinear coefficients. On the contrary, the protonic exchange one requires lower temperatures $< 250°C$ to make hydrogen, provided by a proper acid, exchange lithium ions in the lattice. While also in this case the extraordinary refractive index of the material increases and the ordinary one remains almost constant, the electro-optic and nonlinear coefficients degenerate.

To write waveguides deeper in the bulk, direct writing techniques have been developed. They are based on the high power laser beam focusing inside the medium so to permanently modify the refractive index in the illuminated region. In this way the chemical treatment is avoided reducing the overall cost but this technique remains quite expensive because of the necessity of having powerful lasers and extremely precise translation stages ($\simeq 10^5$\$).

Two approaches are possible depending on the employed source and the host material absorption lines. For example, in lithium niobate, a continuous wave source in the ultraviolet region [4, 5] or a pulsed infrared one working in the femtosecond regime [6, 7] can be employed to take advantage of the very high intensity in the focus. With these techniques a very small focus dimension can and must be achieved. The aim is to locally increase light intensity and thus the refractive index in the focus. At the same time, it is necessary to reduce as much as possible the refractive index variation induced in the solid cone (centred in the focus) provided by the focusing optical system. These techniques can make light propagate with very low propagation losses.

These different approaches grant a guided light propagation, but neither the electro-optic properties nor the refractive indices achieved inside them are optimized for light propagation, only the direct writing allows better performances. This in turn means that propagation losses are not minimized and in general refractive index profiles are not symmetric.

Being the final aim a fully integrated light guiding structure, the ideal solution is to realize real volumetric waveguides for which electro-optic properties can be overworked. In this PhD work, interconnections based on the realization of photorefractive spatial optical solitons will be deeply investigated both as stand alone element and as basic device to realize integrated sources, as it will be demonstrated in the present and in the following two chapters respectively.

Photorefractive spatial solitons allow to overpass all the limitation char-

acterizing the previously described techniques. It is the light itself that induces the refractive index variation necessary to guide the light, taking advantage of the electro-optic properties of the host material.

As a consequence, these structures can be induced in any point of the material volume providing, at the same time, extremely low propagation losses. From a qualitative point of view, both of these properties are consequence of the physical process based on the spatial charge configuration induced by the propagation of a nonuniform light intensity profile, a laser beam for example, inside the material. Consequently, refractive index profile results optimized for its propagation and for all the longer wavelengths. Alongside to light propagation benefits, waveguides realization via spatial optical solitons is much less expensive (few hundreds dollars) than all the other techniques. The whole of these properties make them a very attractive alternative for real 3D waveguides realization.

During last years many different materials, known as photorefractive, have been found to be able to produce a light induced self-confinement behaviour. Some typical examples are strontium barium niobate (SBN) [8], lithium niobate ($LiNbO_3$) [9], potassium lithium tantalate niobate (KTLN) [10], potassium niobate ($KNbO_3$) [11], barium titanate ($BaTiO_3$) [12] as dielectric insulators. Iron doped indium phosphide ($InP:Fe$) [13, 14] and recently also cadmium zinc telluride (CdZnTe) [15] have been successfully used for the semiconductor group. Each of them can provide self-confinement but with different time scales, wavelengths and waveguide durability.

In the following sections two cases will be analysed: lithium niobate and iron doped indium phosphide. The first offers a very long dielectric relaxation time that allow waveguides to be used for very long time without the necessity of fixing them. The latter instead, exhibits a very fast space charge field building up time that make it ideal for fast, all-optical, beam reconfiguration in the infrared, and specifically in the third telecommunication window. $InP:Fe$ will be studied with more details in section 4 both describing the physics for the photorefractive effect and experimentally investigating coherent interactions with the aim of the realization of an all-optical router.

As the two following chapters deal with $LiNbO_3$, in this section the details for the photorefractive process in lithium niobate will be discussed along with its properties giving also some introductory informations about spatial soliton formation obtained by stimulating the Kerr ($\chi^{(3)}$) and the cascading effects (quadratic solitons). Some emphasis will be given to the mathemat-

ical formulation for the photorefractive effect in relation to the equations describing light propagation as an introduction to a new (2+1)D numerical model that well fit the experimental measurements about self-trapping. This model takes into account the different combinations between propagation direction and light polarization so to deepen the material anisotropy effects on soliton formation.

1.1 Spatial optical solitons: alternatives to photorefractivity

Spatial optical solitons deal with the achievement of the complete diffraction compensation for a beam propagating inside a medium. It is the light itself that modifies its phase profile by exciting a proper material nonlinearity which acts as a focusing medium. This double directional action, light-medium and vice versa, establishes a feedback mechanism that allows the light to propagate without diffraction, like if a distributed positive lens appeared all along the propagation distance inside the material. The final material behaviour that this self-focusing effect induces, depends strictly on the medium and on the nonlinearity it can provide.

Different typologies belong to the spatial soliton family and they are identified according to the physical process that originates them. They are the Kerr, the quadratic and the photorefractive spatial solitons. For sake of completeness, the interconnections realization drawbacks associated to the first two typologies will be emphasized. On the contrary, photorefractivity will be extensively used.

The three typologies are consequence of the nonlinear polarization, eq. 1.1, that light electric field can induce in the material by exciting an anharmonic atomic oscillation-like behaviour.

$$P^{NL} \propto \chi^{(1)}E + \chi^{(2)}EE + \chi^{(3)}EEE + ... \tag{1.1}$$

It is worth noting that in the whole thesis the terms self-confinement and soliton will be used as synonyms, also if this is not strictly true as with “soliton” is meant the exact mathematical solution. Actually, it has been also experimentally demonstrated [9] that along with the formation of a bright photorefractive spatial soliton, the beam shape changes from a gaussian to a hyperbolic profile, typical of the mathematical solutions.

1.1.1 Kerr effect based spatial soliton

The Kerr effect is characterized by a material instantaneous response time and by a linear dependency of the induced refractive index variation on the injected laser beam intensity. While it can exist in any medium, for a pure Kerr (centro-symmetric) material, like glass [16], this effect requires a very high light intensity ($GW\,cm^{-2}$) to be excited. It is consequence of a weak symmetric anharmonicity that provides a refractive index variation proportional to the laser beam intensity according to $\delta n = n_0 + n_2 I_{em}$, being n_0 the material refractive index, I_{em} the injected light intensity and n_2 a coefficient that depends on the sign of the anharmonicity and on the $\chi^{(3)}$ term for the nonlinear polarization. Self-focusing can be achieved if n_2 is positive, otherwise a defocusing effect will be obtained. Although this effect is responsible for a refractive index variation that could guide the light, it presents a strong drawback for interconnections realization. In fact, Kerr spatial solitons [17] are unstable and can provide a stable self-confinement only in (1+1)D configurations, so preventing from inducing circular self-trapping in the material. In literature many papers exist about the breaking up and filamentation occurring in (2+1)D self-trapping experiments and first reports date to 60′s years, for example [18,19]. The analytical solution for the refractive index is achievable only in the case of Kerr nonlinearity [20] and as it will be seen in the section 1.4, the expression for the photorefractive case can be found only with a set of strong approximations. Although it cannot be used to write circular waveguides, its instantaneous response time for self-confinement allows the realization of high speed devices, like for example femtosecond lasers working in modelocking regime. In the chapter 3, devoted to second harmonic generation based measurements, a Titanium Sapphire laser is used in such a regime and is able to provide pulses whose duration is in the order of 65fs. The modelocking technique “Kerr-lens modelocking” is based on the generation of a Kerr soliton is the oscillator cavity [21, 22] and in correspondence to the self-confinement achievement, pulses results locked in phase. In the appendix of this thesis, a Kerr nonlinearity Z-scan measurement at 800 nm in a gallium nitride thin film will be also presented.

1.1.2 Cascading-effect-based quadratic spatial solitons

The first predictions for quadratic solitons date to the 70′s years [23,24], but they could be experimentally demonstrated only during the 90′s [25,26]. Al-

though belonging to the spatial soliton family, they don't share the same properties that the others, Kerr or photorefractive, exhibit. They don't modify the medium inside which the light propagates. Neither the material refractive indices, nor the trap state densities are affected, so they cannot provide any guiding structure in the material bulk. These peculiar properties are consequence of the physical mechanism that gives rise to self-trapping: the cascading effect, for which an easy explanation has been provided in [27]. It relies with a radiation propagating inside the medium with a frequency ω that can generate a second wave having a doubled frequency. The process takes place in the framework of a $\chi^{(2)} : \chi^{(2)}$ interaction, so via a two photon absorption in non-centrosymmetric materials. These two waves feel the material dispersion and propagate with different speeds. During propagation they will acquire a phase shift which is responsible for self-trapping to occur, in fact if a down-conversion process occurs on the beam propagating at 2ω, a new contribution at ω will be created and summed to the injected one. This continuous energy exchange between the beams, and, at the same time, phase shift addition, can make the fundamental and the generated beams self-trap by distorting their wavefronts. Self-trapping can occur only if the fundamental beam intensity is above a threshold value. On the contrary of what happens in the photorefractive one, which is based on charge accumulation, it is almost instantaneous as frequency conversion does. In literature, the contemporary spatial self-confinement of the ω and 2ω components, without temporal dispersion compensation, is usually indicated as a simulton. In this thesis, in section 3.6, this aspect will be deepened by experimentally studying the formation of a simulton via the photorefractive nonlinearity in lithium niobate, so with the formation of a real guiding structure with very peculiar properties.

1.2 Lithium niobate

As anticipated in the introduction, lithium niobate is the material we chose to realize optical interconnections using the photorefractive nonlinearity. Actually, it represents an ideal candidate because of the many properties owned and this material is already one of the most employed in the market, being considered as the equivalent of silicium for electronics. It is, *de-facto*, a standard for device realization, like for example optic and acousto-optic modulators, Q-switching devices, optical parametric oscillators (OPO), laser

frequency doubling and many others. Because of its versatility, it has been studied for many years, so many reviews have been written, for example [28–31].

Lithium niobate belongs to the trigonal crystallographic group, with symmetry 3m, and is a dielectric material with uniaxial anisotropic behaviour. Its optical axis, the ĉ axis, is the direction along which the three symmetry planes lie forming an angle of 60° between them.

This material is grown via the Czochralski technique [32, 33] that allows to achieve a very high optical quality, so with a very low defect amount, and is characterized by an hexagonal unit cell. This in turn is formed by two planes occupied by three oxygen atoms (centred along the optical axis) a lithium ion (Li^+) which usually occupies a position on an oxygen plane and a niobium ion (Nb^{5+}) that takes place in between the two oxygen planes, see for example fig.1.1 or Weis et al. [28] and [34] for a graphical representation.

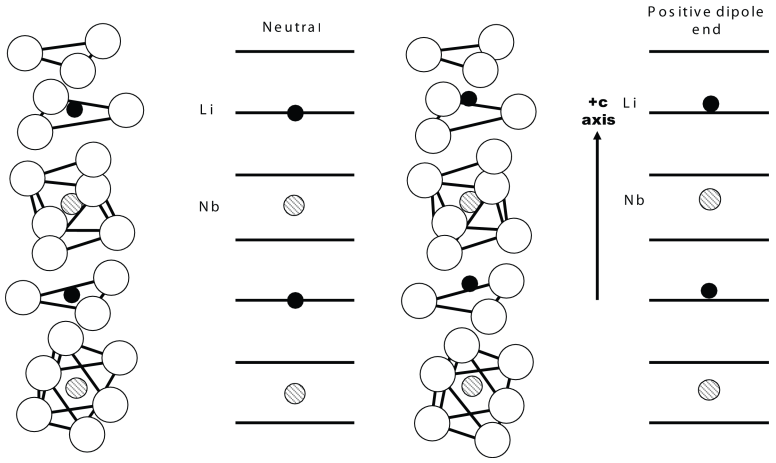

Figure 1.1: Sketch for the lithium niobate unit cell in the paraelectric (on the left) and ferroelectric (on the right) phases. Ref. [28].

In fig.1.1 are reported both the configurations for the paraelectric and ferroelectric phases for lithium niobate. The latter, the one I will refer to in the whole thesis, can be achieved for temperatures below the limit value of about 1210°C (Curie temperature). Lithium niobate boules are grown from an orientated crucible. In the whole thesis the z-cut configuration (optical axis parallel to the z direction) will be used. Typically, commercial lithium

niobate wafers are distinguished according to the lithium and niobium concentration ratios, in fact it is very difficult to obtain samples having the same concentrations for both: the stoichiometric case. Usually grown samples present a high number of lithium vacancies that, for the typical case ([Li]/[Li] + [Nb] = 48.6%) is in the order of 6%. This lithium vacancies have been demonstrated to be responsible for many changes in the photorefractive effect. For example, lithium niobate refractive indices n_e and n_o, extraordinary (along the $\hat{c}$ axis) and ordinary respectively, depend on the material composition besides the temperature. It has been demonstrated that the photorefractive effect (or the optical damage) induces a stronger refractive index variation when the lithium concentration is increased [35, 36]. Refractive index values can be estimated, according to these two parameters (lithium concentration and temperature), using the Sellmeier equation [37]. In the following chapter, this aspect will be deepened by investigating the erbium incorporation effects in the lattice.

Lithium niobate is a ferroelectric material and before using it for photorefractive purposes it is necessary to orient all the ferroelectric domains which, after the growth process, are randomly directed. For this, a strong electric field must be applied so to make it overpass the material coercitive field value. This, in turn, depends again on the lithium concentration and can range between 40kV/cm for the stoichiometric case, and 210kV/cm for a standard congruent one [38]. Once a ferroelectric monodomain sample is obtained, photorefractive properties can be accessed to obtain spatial solitons inside it. Being ferroelectric, when an electric field is applied, a significant change in the spontaneous polarization can be induced and in turn nonlinear optical phenomena can be excited. The non-centrosymmetric nature of $LiNbO_3$ allows to access the $\chi^{(2)}$ contribution for the nonlinear polarization, eq.1.1, so the Pockels effect that together with the photorefractive one is responsible for beam self-confinement.

Self-focusing in this material is mediated by the photovoltaic effect, characteristic of lithium niobate. It is concurrent to the photorefractive effect, but being a critical parameter, it will be explained separately in 2.3

Alongside with these main favourable effects provided by lithium niobate, many other are exhibited, for example the pyroelectric one. It consists in the generation of electric fields, or better in a modification of the spontaneous polarization inside the material by heating the sample [28, 39]. In section 3.6 this effect will be used to study the photorefractive simulton formation.

1.2.1 Electro-optic coefficient

The noncentrosymmetric nature of lithium niobate allows to access the electro-optic component ($\chi^{(2)}$) in the nonlinear polarization expression eq.1.1. It requires that besides the injection of an electromagnetic wave into the sample, also a bias, so static, electric field must be employed. In terms of the optical impermeability tensor η, the Pockels effect can be written as:

$$\eta_{\alpha\beta}(E^{bias}) - \eta_{\alpha\beta}(E^{bias}=0) = \sum_{\gamma} r_{\alpha\beta\gamma} E^{bias}_{\gamma} \tag{1.2}$$

so the coefficients can be expressed as $\mathrm{r}_{\alpha\beta\gamma} = \left[\partial\eta_{\alpha\beta}/\partial \mathrm{E}^{\mathrm{bias}}_{\gamma}\right]_{\mathrm{E}^{\mathrm{bias}}=0}$. The electro-optic tensor contains 27 elements, but adopting the contracted notation and the fact that $LiNbO_3$ belongs to a 3m symmetry group and has only few non-zero components, they can be reduced to 18. The final formulation for this tensor in $LiNbO_3$ is:

$$\begin{bmatrix} 1=(11)=(\alpha\alpha) \\ 2=(22)=(\beta\beta) \\ 3=(33)=(\gamma\gamma) \\ 4=(23)=(32)=(\beta\gamma)=(\gamma\beta) \\ 5=(12)=(21)=(\alpha\beta)=(\beta\alpha) \end{bmatrix} \Longleftrightarrow \tilde{r} = \begin{bmatrix} 0 & -r_{22} & r_{13} \\ 0 & r_{22} & r_{13} \\ 0 & 0 & r_{33} \\ 0 & r_{51} & 0 \\ r_{51} & 0 & 0 \\ -r_{22} & 0 & 0 \end{bmatrix} \tag{1.3}$$

with the following values ($@\lambda = 632.8$nm [40]): r_{13}=8.6 pm/V, r_{33}=30.8 pm/V r_{22}=3.4 pm/V and r_{51}=28 pm/V. The application of the bias electric field causes the deformation of the index ellipsoid so introducing a variation on the material refractive index values. If $\mathrm{n_e}$ is the extraordinary refractive index, for light polarized along the ĉ axis, and if $\mathrm{n_o}$ corresponds to an ordinary polarized radiation, along the â direction, when the bias field is applied, the impermeability tensor changes as:

$$\tilde{\eta} = \begin{bmatrix} \frac{1}{n_o^2} & 0 & 0 \\ 0 & \frac{1}{n_o^2} & 0 \\ 0 & 0 & \frac{1}{n_e^2} \end{bmatrix} + \begin{bmatrix} -r_{22}E_2^{bias} + r_{13}E_3^{bias} & -r_{22}E_1^{bias} & r_{51}E_1^{bias} \\ -r_{22}E_1^{bias} & -r_{22}E_2^{bias} + r_{13}E_3^{bias} & r_{51}E_2^{bias} \\ r_{51}E_1^{bias} & r_{51}E_2^{bias} & r_{33}E_3^{bias} \end{bmatrix} \tag{1.4}$$

To take advantage of the highest value of these coefficients (r_{33}) for the spatial soliton realization, the bias electric field is applied only along the ĉ direction. This is the case for all the measurements that will be discussed in

the following. So being only $E_3^{bias} \neq 0$, it is possible to deduce the consequent refractive index variation:

$$\frac{1}{n_x^2} = \frac{1}{n_o^2} + r_{13}E_z^{bias} \Rightarrow n_x \simeq n_o - \frac{1}{2}n_o^3 r_{13}E_z^{bias} \tag{1.5}$$

$$\frac{1}{n_y^2} = \frac{1}{n_o^2} + r_{13}E_z^{bias} \Rightarrow n_y \simeq n_o - \frac{1}{2}n_o^3 r_{13}E_z^{bias} \tag{1.6}$$

$$\frac{1}{n_z^2} = \frac{1}{n_e^2} + r_{33}E_z^{bias} \Rightarrow n_z \simeq n_e - \frac{1}{2}n_e^3 r_{33}E_z^{bias} \tag{1.7}$$

having indicated with $1 \rightarrow$ x, $2 \rightarrow$ y the two crystallographic directions perpendicular to the ĉ axis and with $3 \rightarrow$ z the one parallel to it.

1.2.2 Photovoltaic effect

Lithium niobate, as the whole family of noncentrosymmetric (pyro-piezo electric) materials, exhibits the photovoltaic effect when shined by a light, no matter if uniform. It relies on the generation of an electric current also in absence of an applied bias electric field and, as will be shown further on, has a very important role in photorefractivity and spatial soliton formation.

This effect was initially discovered by Glass et al. [41] performing current measurements in lithium niobate and barium titanate. They found that a current flow along the direction antiparallel to the ĉ optical axis of the material. Furthermore, they found that the amplitude of this current was proportional to the absorbed power density by means of a proportional factor, the Glass constant k, which contains information about the microscopic effect of the material. The first formulation for this current, measured in conditions of closed circuit, is then:

$$J_{ph} = k\alpha I_{em} \tag{1.8}$$

being α the material absorption corresponding to the injected light wavelength, and I_{em} the light intensity. Further investigations were performed by Belinicher et al. [42] who injected circular polarized light for hologram recording. They found that this current has a tensorial character that can be resumed as:

$$J_{ph} = \beta_{ijk}e_j e_k I_{em} = \alpha k_{ijk}e_j e_k I_{em} \qquad i,j,k = 1,2,3 \tag{1.9}$$

β_{ijk} is the bulk photovoltaic tensor, it is complex so that $\beta_{i,j,k} = \beta^*_{ikj}$ and its complex part plays a role only in case of circular/elliptical polarized light.

e_j, e_k represent the unit vectors for light polarizations. For lithium niobate many terms of the tensor vanish and (using the contracted notation) the equation (1.9) can be written in an explicit way:

$$\begin{bmatrix} J_{ph1} \\ J_{ph2} \\ J_{ph3} \end{bmatrix} = \alpha I_{em} \begin{bmatrix} 0 & 0 & 0 & 0 & k_{15} & -k_{22} \\ -k_{22} & k_{22} & 0 & k_{15} & 0 & 0 \\ k_{31} & k_{31} & k_{33} & 0 & 0 & 0 \end{bmatrix} \begin{bmatrix} e_1^2 \\ e_2^2 \\ e_3^2 \\ 2\hat{e}_3 \cdot \hat{e}_2 \\ 2\hat{e}_3 \cdot \hat{e}_1 \\ 2\hat{e}_1 \cdot \hat{e}_2 \end{bmatrix} \tag{1.10}$$

Values for an iron doped lithium niobate sample are [43]: $k_{31} = 3.3 \cdot 10^{-9}$ A cm/W, $k_{22} = 0.3 \cdot 10^{-9}$ A cm/W, $k_{33} = 2.7 \cdot 10^{-9}$ A cm/W. For a linearly polarized beam, this current is generally considered having just one component along the $-\hat{c}$ axis and this is justified by the fact that the coefficient relative to the perpendicular direction is one order of magnitude smaller.

J_{ph} is strongly dependent on the doping ions introduced in the melt. For example in the case of Cu doping these coefficients are about one forth of those for iron, but J_{ph} depends on the light intensity as well. Above a light intensity threshold which is in the order of $I = 10^7 W\,m^{-2}$ [44–46], other active centres can influence this current. They are provided by the intrinsic defects in the lattice of the material and will be analysed in some more details in section 1.3.1. From a microscopic point of view and for moderate light intensity, this current is completely defined by the filled traps in the band gap. The mechanism causing the current to flow is consequence of electronic-ionic ionization/relaxation and recombination processes. This approach, suggested by Lines and Glass [30], proposes that in correspondence to light excitation, the charge transfer from an impurity towards the closest cation has different probabilities p_+, p_- to occur with respect to a direction or another. The electron mean free paths are indicated with: l_+, l_-. These charges relax to different positions so the recombination probabilities p'_+, p'_- will differ from p_+, p_-. This defines a steady state current to which also the ionic contribution should be added, also if usually can be neglected. If Z_i is

the ion charge and δl_i its displacement, then:

$$J_{ph} = \frac{\alpha I_{em}}{h\nu}\left[e[l_+(p_+ + p_+^{'}) - l_-(p_- + p_-^{'})] + (Z_i - Z_i^{'})\delta l_i\right] = k\alpha I_{em} \tag{1.11}$$

$$k = \frac{1}{h\nu}\left[e[l_+(p_+ + p_+^{'}) - l_-(p_- + p_-^{'})] + (Z_i - Z_i^{'})\delta l_i\right] \tag{1.12}$$

So k is a function of the material and depends on the concentration of an eventual dopant introduced inside it.

On the contrary, if the sample is in open circuit condition and if it is shined, charges will start moving defining a capacitor like behaviour. They are accumulated in correspondence to the +c and −c facets of the sample. An electric field is then generated proportionally to the material conductivityσ, so that:

$$J = k\alpha I_{em} + \sigma E \tag{1.13}$$

When the stationary regime is reached then the total current in the sample must be zero and consequently the photovoltaic field value can be found:

$$E_{ph} = -\frac{k\alpha I_{em}}{\sigma} \tag{1.14}$$

and is directed parallel to the $\hat{c}$ axis.

In the next chapter an experimental investigation about the effects of the rare earth erbium on photovoltaic field will be done, proving the existence of a dependency on its concentration in the lattice.

1.3 From photorefractivity to bright spatial solitons, application case: $LiNbO_3$

Up to now no details have been yet done about the nonlinearity that is able to provide photorefractive beam self-trapping.

This process deals with the refractive index variation induced by the light excitation and recombination of charges, typically electrons in the more common models for $LiNbO_3$. Photorefractive materials usually possess a wide band-gap ($\simeq$ 4eV for $LiNbO_3$), but are also characterized by the presence of impurity atoms or defects which add energetic levels inside it. It is thank to them that photorefractivity can take place. Light propagating inside the material, excites charges (electrons) from the donors states to

the conduction band, donors density is indicated with N_D. Being free to migrate because of various mechanisms (further on described), they finally recombine with the uncompensated traps, acceptors (having density N_A), after a material specific propagation mean path. The recombined charges define dipoles whose final effect is to create an electric field in correspondence to the illuminated region in the bulk. In turn, this resulting field (space charge field E_{SC}), induces the refractive index variation necessary to make the beam self-trap and form the photorefractive spatial soliton. Photorefractivity is thus a nonlocal process. On the contrary of what happens for Kerr solitons, here the refractive index increasing is obtained via the electro-optic effect according to the equality $\delta n = -1/2 r_{eff} n_{eff}^3 E_{SC}$, so the $\chi^{(2)}$ contribution in the expression for nonlinear polarization. r_{eff} represents the electro-optic coefficient excited by the injected light polarization and n_{eff} is the corresponding refractive index.

If the induced variation is positive ($\delta n > 0$), then a guide is created and light can propagate inside it experiencing all the benefits previously indicated and a bright soliton is formed. As a consequence of the photovoltaic effect in $LiNbO_3$, if this variation is negative, then a light defocusing is obtained and for proper conditions it can take to a photovoltaic soliton formation.

Photorefractive spatial soliton birth dates to years 90′s when Segev et al. [47] predicted their existence. They were then experimentally observed by Duree et al. in 1993 [48] under the hypothesis that a two wave mixing induced gain was responsible for light self-confinement. Starting from these observations, many kind of photorefractive solitons have been investigated: screening [8, 49, 50], photovoltaic [51–55] and screening-photovoltaic [56–58] solitons. The fundamental difference existing between screening and photovoltaic solitons is that, in the first case, a bias (external) electric field E_0 is necessary to induce a positive refractive index variation, so a profile able to guide the light. In the second, this bias field is not required and charges don't move along random directions but are forced to displace along the crystalline axis of the material. Actually, this behaviour is known to be consequence of the bulk photovoltaic effect and, as said, cannot take place in any material, but only in noncentrosymmetric (piezoelectric and pyroelectric) crystals.

In this thesis, all the presented investigations in lithium niobate are performed in presence of both the effects, so with reference to the screening-photovoltaic approach, for which a more detailed characterization will be

formulated.

At the very beginning, it was not yet possible to establish real differences between the photorefractive solitons and the Kerr one, as only (1+1)D experiments had been performed. Once also (2+1)D measurements were realized [8], it became clear that photorefractivity owned quite peculiar properties. Not only the power necessary to make beams self-compensate their natural diffraction was order of magnitude lower, but stable self-confinement along both the transverse dimensions could be achieved. In addition, spatial solitons sustain waveguides (temporary or permanent according to the material specific dielectric relaxation time) able to guide a radiation at longer wavelengths than the one used to write them. These benefits enhanced research activity in this field. Another aspect which characterize a bright photorefractive spatial screening, or screening-photovoltaic, soliton is the so said "bending". Its effect consists in making the self-trapped beam move along the $-\hat{c}$ direction, and this displacement can be large. This in turn implies that the soliton, so its associated waveguide, does not propagate straight along the sample. Chauvet et al. [59] demonstrated that this effect is consequence of a not high enough amount of acceptors in the material and that can be reduced or balanced by adding an additional uniform background illumination to the nonlinear medium.

To the mentioned spatial solitons categories, another one can be added. It differs from the previous for the fact that the physical mechanism is based on the presence of two carriers (electrons and holes) instead of one (electrons), and both are free of moving along both the bands (conduction and valence). As $InP:Fe$ belongs to this group, it will be treated with much more details in chapter 4 where the problem of coherent interactions between solitonic beams inside this material will be analysed.

1.3.1 One carrier model for photorefractivity in lithium niobate

Photorefractive effect in lithium niobate has been extensively studied because of the many application for which it is suitable. Actually, at the very beginning it was used for holografic purposes, so the necessity of writing stable, durable and high contrast induced gratings in the bulk arose. Consequently, different working regimes have been tried to maximize their performances. Measuring the main parameters involved in a photorefractive process, like for example birefringence or photovoltaic current [44–46], it has been demonstrated that, in addition to the trap states in the band gap, other

microscopic active centres may play an important role. According to light intensity, doping and extrinsic/intrinsic defect effects must be considered. Accordingly, different models have been developed to explain the different behaviours.

All the measurements that will be presented in this thesis can be explained in terms of the easiest developed model, the one-carrier one-band, so a more accurate theoretical introduction will be devoted to it. In the following section, the mathematical approximations usually done to achieve an analytical (strongly approximated) solution will be presented.

The very first formulation for the "optical damage", as this process was initially considerated as a drawback for the material, must be addressed to Ashkin and Amodei [60, 61]. The final and most used model today is the one proposed by Kukhtarev [62], and for it the usual equation set, for the 1D case, is:

$$\frac{\partial N_D^+}{\partial t} = s(I_{em} + I_d)(N_D - N_D^+) - \xi n N_D^+ \tag{1.15}$$

$$\frac{\partial(\epsilon_0 \epsilon_r E_{SC})}{\partial x} = \rho \tag{1.16}$$

$$\rho = q(N_D^+ - N_A - n) \tag{1.17}$$

$$\frac{\partial J}{\partial x} = -\frac{\partial \rho}{\partial t} \tag{1.18}$$

$$J = e\mu n E_{SC} + \mu K_B T \frac{\partial n}{\partial x} + \beta_{PV} I_{em}(N_D - N_D^+) \tag{1.19}$$

The idea is that when a non-uniform intensity profile light beam (I_{em}) propagates inside a photorefractive material, charges (electrons) can be excited to the conduction band from still available donors $N_D - N_D^+$ present in the trap states. Along with this contribution, also the thermal effect must be addressed via the dark intensity I_d and the photoexcitation coefficient s. These free electrons define a current J, being forced to move by three contemporary effects. The free electron density (n) in the illuminated region defines a strong concentration gradient with the remaining part of the sample so a diffusion component appears proportionally to the temperature (T): $J = \mu K_B T \partial n / \partial x$. These displaced electrons (having charge e) force a space charge field (E_{SC}) to build up. In fact, they locally modify the material spontaneous polarization, so making a drift component arise: $J = e\mu n E_{SC}$. In addition lithium niobate is also photovoltaic, so also a component directed

along its optical (ĉ) axis must be considered: $J = \beta_{PV} I_{em}(N_D - N_D{}^+)$. Finally the free electrons can be trapped by the acceptors in the band-gap, proportionally to the recombination coefficient ξ: $\xi n N_D{}^+$.

The generated charges must satisfy also the current continuity equation (1.18) and the Poisson equation, eq. (1.16), which provide a way to deduce the value for the induced space charge field according to which, the refractive index is locally changed via the electro-optic effect. The total charge is provided by the (1.17) where N_A represents the acceptors concentration.

This model is accepted for light intensities [44, 46] less than $10^6 \div 10^7$ $W\,m^{-2}$, for which only the extrinsic active centres provide charge photo-excitation. Typically, these centres are identified in the iron ions Fe^{2+}, Fe^{3+} which can act as donor or acceptors according to the expression:

$$Fe^{2+} + h\nu \Longleftrightarrow Fe^{3+} + e \tag{1.20}$$

Above that light intensity threshold, other centres start to play a role and they are related to the intrinsic defects in the material. So for example, in a congruent lithium niobate sample, where a large number of lithium vacancies are present, niobium ions tend to move on these empty positions (niobium antisite). In this situation the model must be improved by adding a second set of energetic levels related to these defects ($Nb_{Li}^{4+}, Nb_{Li}^{5+}$), so a two centres - one band charge transport model must be considered, for example [29, 45].

In the following chapter a characterization of erbium doping effects on the photorefractive properties of lithium niobate will be proposed, but as light intensities are much lower than the reported threshold, then the simplified scheme is considered. Furthermore, as erbium is known to occupy lithium positions, at least for the investigated *"low"* doping concentrations, the number of extrinsic defects should decrease so confirming this assumption.

1.4 Classical mathematical approximations

Photorefractive models don't allow analytical solutions, so many approximations are necessary to obtain an easiest expression that can be used to describe photorefractive processes, and in this specific case, beams self-trapping. The problem is that also in the approximated form, its numerical computation is extremely expensive in terms of calculation time and the

provided results are strongly affected by the used approximations, so often they don't fully match the experimental observations.

Along with the discovery of the various categories of photorefractive spatial solitons, different theoretical models have been developed to describe the temporal evolution of such structures. Models relative to generic photorefractive solitons or screening solitons, for example [63, 64], and after for the photovoltaic one as in [51, 65] have been unified for the screening-photovoltaic typology [56, 57]. Thanks to these models it is possible to distinguish between two solitonic regimes: the steady state and the quasi-steady-state. The first condition implies that once formed, the solitonic beam keeps its undiffracted structure for an infinite time (ideally). The latter is relative to solitonic configuration that remains unchanged for a very short time after which the beam starts diffracting again and eventually to re-trap. In the following of this thesis I will refer to this condition for the measurements in lithium niobate.

In the following, two sections are devoted to a brief introduction of the classical approximations, so to identify the more critical points that characterize this kind of analysis. Afterwords, a novel and much more complete (2+1)D approach, developed at the University of Besançon (France), will be used to analyse the experimental results about the optimization of the written waveguides, last section of this chapter.

1.4.1 Space charge field derivation: time dependency and stationary regime

The equations written for the Kukhtarev model, (1.15)-(1.19), can be manipulated to provide an expression for the photorefractive induced space charge field. In this section, its expression will be elaborated and all the required simplifications will be indicated with the aim of finding the temporal dependency for E_{SC} and its steady state expression. To do this the formalism adopted by [63, 66] is used.

With reference to the equations relative to the current J induced in the material, eq. (1.19), and the charge conservation law, eq. (1.18), one single equation depending both on space and time can be obtained. By deriving the (1.19) with respect to x and according to the equalities (1.18) and (1.16), the following equation can be written:

$$-\epsilon_0\epsilon_r\frac{\partial^2 E_{SC}}{\partial x\partial t} = e\mu\frac{\partial(nE_{SC})}{\partial x} + \mu k_B T\frac{\partial^2 n}{\partial x^2} + \frac{\partial}{\partial x}\left[\beta_{ph} I_{em}(N_D - N_D^+)\right] \quad (1.21)$$

which can be integrated with respect to the x parameter, so to obtain:

$$-\epsilon_0\epsilon_r\frac{\partial E_{SC}}{\partial t} = e\mu nE_{SC} + \mu k_B T\frac{\partial n}{\partial x} + \beta_{ph}I_{em}(N_D - N_D^+) + J_0 \qquad (1.22)$$

J_0 is an integration constant which can be derived by means of experimental considerations. In fact, as the transverse dimension for a self-trapped beam is much narrow than the sample width, it can be stated that far enough from the beam centre, light intensity is uniform. This makes all the spatial derivatives negligible. This intensity value will be indicated as I_∞.

As previously indicated, in order to induce a positive variation for the refractive index in lithium niobate, it is necessary to apply an external bias electric field E_0. This can be obtained closing the sample, having thickness d, on a voltage (V) generator so to obtain an electric field value $E_0 = V/d$. In correspondence to the position for which the intensity I become uniform, the total electric field acting on the sample $E_{tot} = E_{SC} \simeq E_0$, so $\partial E_{tot}/\partial t \simeq 0$, and in turn:

$$J_0 = -e\mu nE_{SC} - \beta_{ph}I_\infty(N_D - N_D^+) \qquad (1.23)$$

J_0 will result completely known if the electron and the ionized donor density, n and N_D^+ respectively, can be found.

The photorefractive process is non-instantaneous, in the sense that it is based on the accumulation of ionic charges, so it is related to the dielectric response time which is much longer than the electron generation time, $\frac{\epsilon_0\epsilon_r}{e\mu n}$ the first and $\frac{1}{\xi N_A}$ the latter. Because of this, the time necessary to generate electrons can be neglected. Being $n \ll N_D^+, N_A$ for moderate light intensities, then both the parameters can be found. For N_D^+ equations (1.16) and (1.17) must be used, while for the electron density, the (1.15) with the hypotesis $\partial N_D^+/\partial t \simeq 0$ is to be taken into account, so to find:

$$N_D^+ = N_A\left[1 + \frac{\epsilon_0\epsilon_r}{eN_A}\frac{\partial E_{SC}}{\partial x}\right] \qquad (1.24)$$

$$n = \frac{s\left[I_{em} + I_d\right]\left[N_D - N_A\left(1 + \frac{\epsilon_0\epsilon_r}{eN_A}\frac{\partial E_{SC}}{\partial x}\right)\right]}{\xi N_A\left(1 + \frac{\epsilon_0\epsilon_r}{eN_A}\frac{\partial E_{SC}}{\partial x}\right)} \qquad (1.25)$$

These, introduced in the expression for J_0, take to its final expression:

$$J_0 = -\beta_{ph}\left(N_D - N_A\right)I_\infty - e\mu\frac{s\left(I_\infty + I_d\right)\left(N_D - N_A\right)}{\xi N_A}E_0 \qquad (1.26)$$

This expression remains valid in the limit of a closed circuit configuration. As it does not depend anymore on the x direction, if $E_0 = 0$ then also J_0 vanishes. At this stage, the equation providing the time dependency for the space charge field, (1.22) can be solved, but only with numerical methods.

The obtained value for the local space charge field can be then used to study the propagation of a laser (in general non-uniform intensity profile beam) inside a photorefractive media.

Anyway, an analytical solution can be found with some other simplificative assumptions. If the charge density spatial modulation can be assumed weak and being acceptor density high, the term $\frac{\epsilon_0 \epsilon_r}{eN_A} \frac{\partial E_{SC}}{\partial x}$ in (1.24) can be neglected with respect to unity. As a consequence of this, n and the (1.22) can be re-written as:

$$n = \frac{s\,(I_d + I_{em})\,(N_D - N_A)}{\xi N_A} \tag{1.27}$$

$$T_d I_d \frac{\partial E_{SC}}{\partial t} + (I_d + I_{em})\,E_{SC} + \frac{K_B T}{e}\frac{\partial I_{em}}{\partial x} = E_{ph}\,(I_\infty - I_{em}) + (I_d + I_\infty)\,E_0 \tag{1.28}$$

Finally, under the hypothesis of a laser beam whose intensity profile does not change with time, it is possible to derive the analytical expression for the space charge field:

$$\begin{aligned} E_{SC}(x,t) = &\left[\frac{(E_{ph} + E_0)\,(I_{em} - I_\infty)}{I_{em} + I_d} - \frac{K_B T}{e}\frac{1}{I_{em} + I_d}\frac{\partial I_{em}}{\partial x}\right] \cdot \\ &\cdot \left[e^{-\frac{I_{em} + I_d}{T_d I_d} t} - 1\right] + E_0 \end{aligned} \tag{1.29}$$

From this expression it is possible to exploit the time dependency of space charge field building up on the dielectric relaxation time T_d. It is the time during which the light induced photorefractive pattern completely relax in absence of light. $T_d = \frac{\epsilon_0 \epsilon_r}{e\mu} \xi N_A / [\beta(N_D - N_A)]$, being β related to the dark intensity through the relation $I_d = \beta/s$. T_d represents one of the most appreciated properties of lithium niobate as it is quite long and permits the use of charge pattern for long time also under the exposition to light without the necessity of applying a thermal or electric treatment for fixing, not yet fully working for $LiNbO_3$. The photovoltaic field has expression: $E_{ph} = (\beta_{ph} \xi N_A) / (e\mu S)$.

In correspondence to the stationary regime, so for t $\rightarrow \infty$, the (1.29) can be written as:

$$E_{SC}(x, t \rightarrow \infty) = -E_{ph}\frac{I_{em} - I_{\infty}}{I_{em} + I_d} - \frac{K_B T}{e}\frac{1}{I_{em} + I_d}\frac{\partial I_{em}}{\partial x} + E_0\frac{I_d + I_{\infty}}{I_{em} + I_d} \tag{1.30}$$

Another approximation that is usually done to decrease calculation time consistes in neglecting the diffusion term in the equation (1.29), so to reduce (1.30) to:

$$E_{SC}(x, t \rightarrow \infty) = -E_{ph}\frac{I_{em} - I_{\infty}}{I_{em} + I_d} + E_0\frac{I_d + I_{\infty}}{I_e m + I_d} \tag{1.31}$$

The last assumption is justified by the fact that the electric field produced by the diffusion process is about two orders of magnitude less than the photovoltaic and the external fields which are as high as some kV/cm. At a glance, the last equation shows that the space charge field basic elements are the photovoltaic field and the bias, external, electric field and that they have concurrent effects. In a photorefractive, but not photovoltaic, material bright screening solitons can be obtained by adding an external field to produce an increasing of the refractive index in the illuminated region. If also the photovoltaic contribution is present, then its effect is to produce light defocusing proportionally to the injected light intensity. This implies that in the case of a screening photovoltaic medium, like lithium niobate, the bias electric field must be high enough to compensate the defocusing effect and so it is expected (and experimentally verified) that $\|\mathrm{E}_0\| > \|\mathrm{E}_{\mathrm{PV}}\|$.

This equation shows also the saturable nature of the photorefractive nonlinearity. Assuming $\mathrm{I}_{\infty} \simeq 0$, the two fractions can be written in function of the $\mathrm{I}_{\mathrm{em}}/\mathrm{I}_{\mathrm{d}}$ ratio. It has been demonstrated that this ratio is one of the main parameters for the minimization of the self-trapped beam dimension [67]. This ratio can be changed by increasing the I_{d} component via a high intensity background illumination on the sample. This operation in turn will reduce or eliminate the beam bending and in general stabilize the soliton formation dynamics.

In the next chapter, when erbium influence on the photovoltaic field will be exploited, it will be demonstrated that in correspondence to the condition of minimized photovoltaic field, self-trapping properties are maximized for each value of the applied bias electric field.

1.4.2 Approximated wave equation for beam propagation in a PR medium: solitonic solution

To study the propagation of a laser beam inside a photorefractive medium, it is necessary to specialize the Helmotz equation for this kind of material, so to keep into account the induced space charge field in the illuminated region. Helmotz equation has the expression:

$$\bigtriangledown^2 \vec{E} + k^2 \vec{E} = 0 \tag{1.32}$$

being $\tilde{\mathrm{E}}(\mathrm{x},\mathrm{z},\mathrm{t}) = \mathrm{A_z}(\mathrm{x},\mathrm{z})\mathrm{e}^{\mathrm{j(kz}-\omega\mathrm{t})}\hat{\mathrm{c}}$ the electric field associated to a wave propagating along the z direction and diffracting along the ĉ axis, this direction is referred as x for convenience. This wave is supposed to be independent from the other transverse coordinate y. The assumption that the propagation occurs inside a weakly perturbed medium is done, so the Slowly Varying Envelope Approximation (SVEA) approximation can be applied. Keeping in count the expression that the electric field vector (or equivalently the electric displacement vector) assume as a consequence of the electro-optic effect, section 1.2.1, the wave equation can be re-written in scalar approximation, as:

$$\left(\frac{\partial}{\partial z} - \frac{i}{2k}\frac{\partial^2}{\partial x^2}\right) A(x,z) = -i\frac{k}{n_0}\frac{1}{2} n_{eff}^3 r_{eff} E_{SC} A(x,z) \tag{1.33}$$

where $\mathrm{n_{eff}}$ and $\mathrm{r_{eff}}$ represent the refractive index $(\mathrm{n_e}, \mathrm{n_o})$ and the electro-optic coefficient $(\mathrm{r_{33}}, \mathrm{r_{13}})$ according to the injected light polarization, extraordinary or ordinary respectively. $\mathrm{E_{SC}}$ is the expression for the induced space charge field in its approximate form.

The expression for $\mathrm{A(x,z)}$ must satisfy the basic property for a propagating solitonic beam, so its transverse dimension must be independent from the x coordinate. Defining $\mathrm{r} = \mathrm{I_{em}}/\mathrm{I_d}$, u the soliton profile which depends only on the z transverse coordinate and Γ the soliton propagation constant, then:

$$A(x,z) = \sqrt{rI_d}\, u(x) e^{i\Gamma z} \tag{1.34}$$

In this expression, the $\mathrm{E_{SC}}$ formulation of (1.29) is substituted and the diffusion effect $(\propto \mathrm{K_B T})$ is neglected. Thus a dimensionless differen-

tial equation describing the spatial soliton formation in a photorefractive-photovoltaic medium can be written:

$$u''(X) = 2k\Gamma d^2 u(X) + \alpha u(X) + (1+\alpha)u(X) r \frac{u^2(X) - u_\infty^2}{1 + ru^2(x)} \left(e^{-\frac{1+ru^2(X)t}{T_d}} - 1 \right) \tag{1.35}$$

where $X = x/d$, $d = \sqrt{k^2 n_{eff}^2 r_{eff} E_{ph}}$ and $\alpha = E_0/E_{ph}$.

This equation can be used both for the dark and the bright soliton, according to the imposed boundary conditions. In the case of the dark soliton they are: $u''(\infty) = 0$ and $u(\infty) = 1$, while for the bright one they are $u(\infty) = 0$ and $u(0) = 1$ along with $u'(0) = 0$.

The final equation can be integrated and provide the wave equation for the soliton, dark or bright, in the PR-PV medium. This solution is affected by many and meaningful approximations.

In the next section a new approach will be discussed and demonstrated with experimental measurements that represent also the base for the production of more efficient and optimized waveguides in lithium niobate.

1.5 Guiding optimization and anisotropy effects on bright spatial soliton induced waveguides in lithium niobate

Via the electro-optic effect, the screening field can induce a positive refractive index variation in the illuminated region of a photorefractive sample. It remains stable for a long time also when both the laser beam and the bias electric field are switched off, so a waveguide remains written. This result is independent on the achievement of a steady-state or quasi-steady-state soliton solution. In fact, the formation process in lithium niobate is slow enough to stop the solitonic build up as soon as the maximum for self-confinement is achieved. No matter if it represents a temporary condition.

It is the long relaxation time of lithium niobate that makes soliton waveguides efficient also when used to propagate the light without any applied bias electric field. Stability/durability can be further increased by choosing a wavelength far from the material photorefractive absorption range.

As in $LiNbO_3$ photorefractive absorption increases moving towards the ultraviolet region, and is negligible in the infrared one, if the guide created

with visible light is probed by an infrared beam, it will not be deteriorated. The problem I have been studying since my master degree thesis, is the realization of such waveguides in conditions of low and very high light intensities and for different wavelengths so to exploit the different mechanisms involved in their formation and to prepare the conditions to make such a waveguide sustain a laser action inside it. A complete experimental characterization about these aspects is reported in [68]. While the last theme will be faced in the next chapter, here the problem of improving the guiding properties for light propagation inside such waveguides will be described both numerically and experimentally.

Lithium niobate exhibits an electro-optic coefficient relative to the extraordinary light polarization higher (about three times) [20, 69] than the ordinary polarization one, $r_{33} = 32\,\mathrm{pm/v}$ and $r_{13} = 9.4\,\mathrm{pm/V}$ respectively. Because of this, the realization of such waveguides using the r_{13} coefficient was never investigated before. In this framework, in collaboration with the University of Besançon, the effects of light polarization on the self-trapping process have been investigated in function of the intrinsic anisotropy of this material [70], both numerically and experimentally.

The idea is to propagate a laser beam at 532nm and at 632nm along the two direction perpendicular to the material optical axis and to verify the self-trapping process in function of the light polarization, so to exploit the anisotropy effects on it. A bias electric field is applied across the facets perpendicular to the $\hat{c}$ axis and is as high as $E_{bias} = 40\mathrm{kV/cm}$. Laser beams are focused on the input face of the sample, according to the light propagation direction, on a spot having size equal to 12 μm FWHM.

Before describing the performed measurements, it is worth introducing the numerical model developed by Fabrice Devaux and Mathieu Chauvet at the University of Besançon. Actually, their split step BPM approach demonstrated [71–73] to be able to explain in details experimental measurements in $LiNbO_3$. The model can strongly reduce the number of approximations typically introduced. It can also take into account the diffusion effect. The main advantage, calculation speed, is provided by the different approach used to determine the space charge field, it is no more based on the solution of the Poisson equation (1.17) which is the typical strategy.

As regards the photovoltaic effect, it is taken into account separating its components in function of the polarization, in other words it is no more supposed to be non-zero exclusively along the material optical axis, but contributions β_{13} and β_{33} are considered.

To make the anisotropy effects explicit, the more general form for the refractive index variation induced in the illuminated region via the electro-optic effect is written as:

$$\Delta n = -\frac{1}{2} n_{eff}^3 \tilde{r} \begin{bmatrix} E_X \\ E_Y \\ E_Z \end{bmatrix} \tag{1.36}$$

being n_{eff} the bulk refractive index corresponding to the injected polarization and $\tilde{r}$ the electro-optic tensor.

A laser beam is simulated to propagate along the 20mm long y axis. No matter if extraordinarily or ordinarily polarized, the refractive index variation depends exclusively on the electric field component directed along the z direction, eq.(1.37) and (1.38) other than the polarization related bulk refractive index and electro-optic coefficient. This is consequence of the electro-optic tensor expression and in this case the anisotropy does not play any role.

$$\Delta n_Z = -\frac{1}{2} n_e^3 r_{33} E_Z \tag{1.37}$$

$$\Delta n_X = -\frac{1}{2} n_o^3 r_{13} E_Z \tag{1.38}$$

As expected, the initially diffracted beam is found to self-trap. Its shape is not perfectly circular but slightly larger along the direction perpendicular to the ĉ axis, fig.1.2a(a) and fig.1.2b(a), respectively. This is coherent with the fact that the bias electric field acts along the z (parallel to the ĉ axis) direction and that the nonlinearity is stronger along it; consequently the induced refractive index change is more efficient, fig.1.2a(b) and fig.1.2b(b). Another information provided by these simulations is that the induced space charge fields profiles are not symmetric, in the sense that the component along the x direction, E_X, presents four lobes tilted of about 45° with respect to it, fig.1.2a(d) and fig.1.2b(d). In this case, it is the space charge field component E_Z to drive the process.

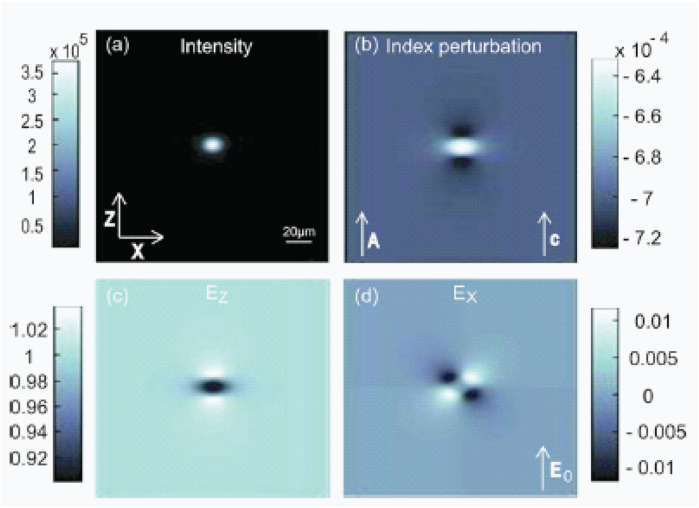

(a) Numerical simulation about the self trapping process for an extraordinary polarized beam propagating along the y direction.

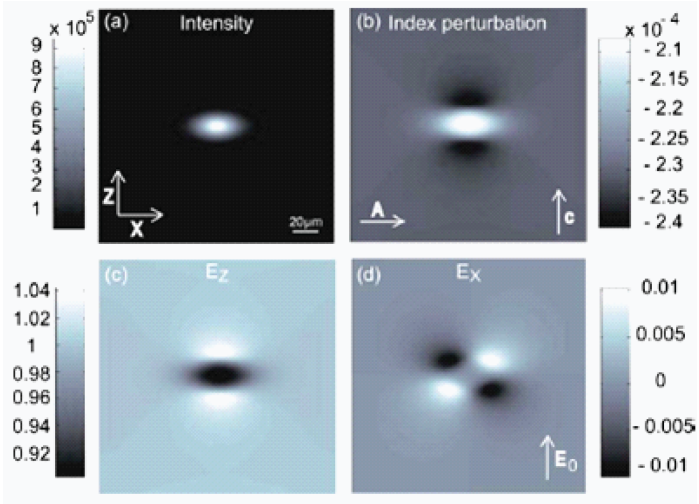

(b) Numerical simulation about the self trapping process for an ordinary polarized beam propagating along the y direction.

Figure 1.2: Numerical simulations about the propagation along the y direction of an extraordinary polarized beam in fig.1.2a and an ordinary one in fig.1.2b. The induced refractive index shape as well as the space charge fields don't differ, but the final spot dimension is much larger in the case of an ordinary polarization.

One important aspect to stress, is that while the qualitative behaviour for the self-trapping process related to an extraordinary or to an ordinary polarized laser beam is the same (while propagating along the y direction), some differences exist. The r_{13} coefficient is much smaller than the other, so usually self-trapping was expected not to occur or to be very disadvantaged. At a first glance from numerical results, such process can be resumed in two "drawbacks": larger dimensions for the final spot of an ordinary polarized beam and a much longer time required to achieve it.

Quantitatively, for an input beam having a waist FWHM $w_{in} = 12\mu$m and extraordinary polarization, the final dimensions are 10x14μm. For the ordinary case they increase up to 24x38μm.

Actually, the much more important point is related to the photovoltaic contribution, but for its explanation it is necessary to introduce the corresponding experimental test.

A laser beam with power of about 114μW is focused on the 12μm FWHM spot and let propagate along the y direction. A proper imaging system is then used to conjugate the output face of the sample on a ccd camera sensor, fig.1.3.

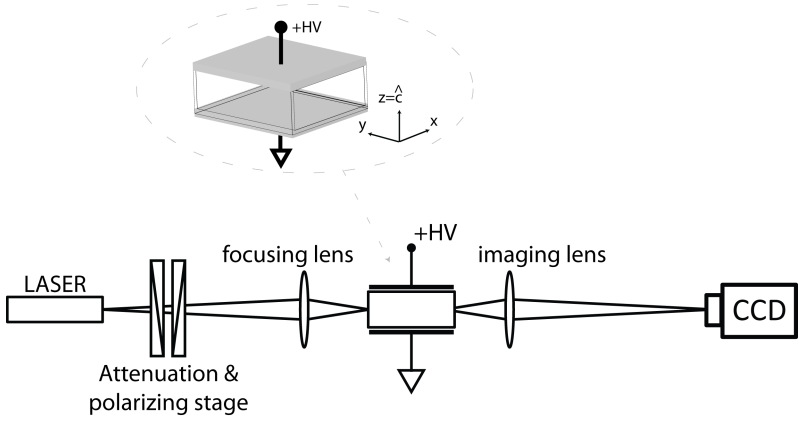

Figure 1.3: Sketch for the experimental setup employed to investigate the self-trapping process in lithium niobate along the two transverse propagation directions.

The evolution corresponding to the extraordinarily and ordinarily polarized beam are reported in fig.1.4a and fig.1.4b respectively.

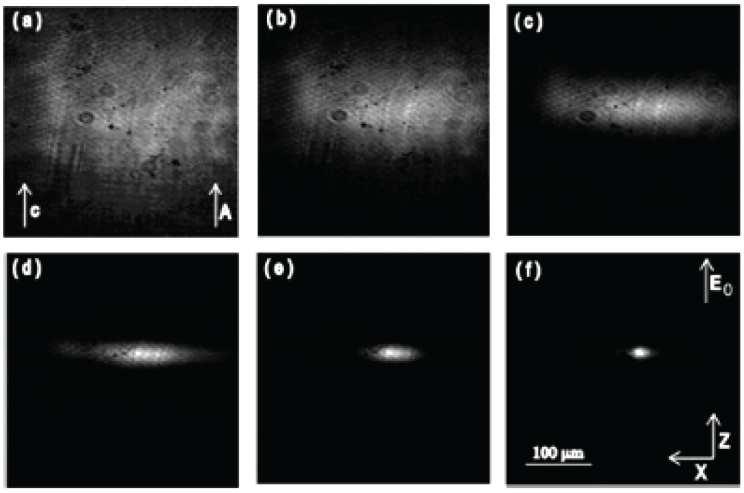

(a) Self trapping for an extraordinary beam. The final dimension is 12x14μm and is obtained in 405 sec.

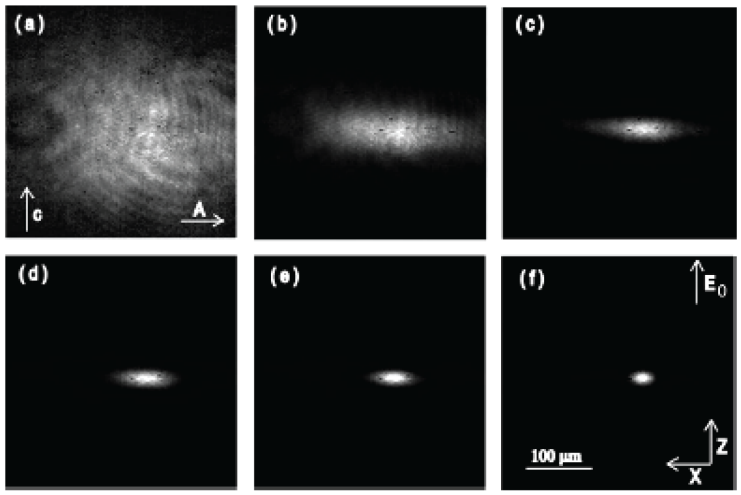

(b) Self trapping for an ordinary beam. The final dimension is 12x14μm and is obtained in 1020 sec.

Figure 1.4: Experimental measurements about self-trapping for a laser beam (532nm) propagating along the y direction. It is extraordinary polarized in 1.4a and ordinary polarized in 1.4b. The injected power is 114μW and is focused on the input face with a waist of $w_{in} = 12\mu$m FWHM. The final self-trapped spot is comparable in size but the confining time is very different.

A well formed self-trapped spot is achieved for both. The self-confined beams have comparable dimensions for both cases exhibiting a w_{out} = 12x14 μm FWHM, but their formation times are very different: t = 450 sec. for the first and t = 1020 sec. for the latter. Being all the experimental parameters the same, but the electro-optic coefficient, this result is not obvious and cannot be explained only by considering the longer evolution time.

Numerically, and by changing the value for the ordinary beam-related photovoltaic field, it has been found that the best fit for the experimental condition corresponds to $E_{ph} = 24$kV/cm, fig.1.5, instead of to the previously considered $E_{ph} = 35$kV/cm. This result allows to conclude that a stronger space charge field is formed with respect to an extraordinary polarized beam. This is coherent with the nature of the induced space charge field; it is provided by the concurrent effect of the bias electric field and the photovoltaic one, so if the second decreases, E_{SC} increases.

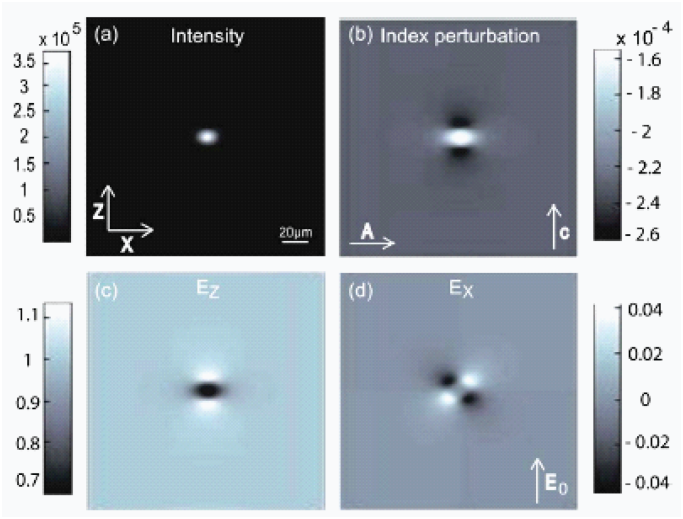

Figure 1.5: Numerical simulation about the self-trapping process for an ordinary polarized beam propagating along the y direction. The photovoltaic field value is decreased to fit the corresponding experimental measurement reported in fig.1.4b. This result is obtained with $E_{ph} = 24$kV/cm instead of $E_{ph} = 35$kV/cm.

This, in turn, is expected to provide a more efficient waveguiding structure, and will be demonstrated further on.

If the laser beam is let propagate along the (7mm long) x axis with extraordinary polarization, analogous results are achieved, but if the ordinary polarization is chosen, the anisotropy effect can be emphasized. In this case, the refractive index modification does not depend only on the E_Z space charge field component, but also on the E_Y one:

$$\Delta n_Y = -\frac{1}{2} n_o^3 \left(r_{22} E_Y + r_{13} E_Z \right) \tag{1.39}$$

In this condition, both numerically and experimentally, a tilt with respect to the optical axis is found for the self-trapped beam: fig.1.6a and fig.1.6b. The refractive index is given by the sum of two terms and the one along z is stronger. Consequently, this tilt can be observed only at the beginning of the self-trapping process and tends to vanish when E_Z starts becoming predominant. It completely disappears when self-confinement is complete. Actually, the anisotropy effect can be observed only when self-trapping starts to occur. Experimentally, to make this more evident, a He-Ne laser at 632.8nm is used. For this wavelength the photorefractive absorption is less strong than for the green; the general process becomes slower and can be stopped at any moment to freeze this configuration. It must be stressed here that this result can neither be seen in the quasi-steady-state nor in the steady-state regime.

The last question to answer is which configuration provides the more optimised structure: is it better to employ an extraordinary or ordinary polarized laser to write the guides? Once the guides are created, light (visible) and bias electric field are switched off. To test their propagation properties, infrared beams ($\lambda = 1064$nm and $\lambda = 1550$nm) are injected inside them with extraordinary polarization. Again, this wavelength is used to increase as much as possible guide lifetime. It is worth remembering that spatial soliton induced waveguides own the property of guiding a radiation having the same wavelength used to write it as well as all the longer ones, with the only limitation given by the material transparency range.

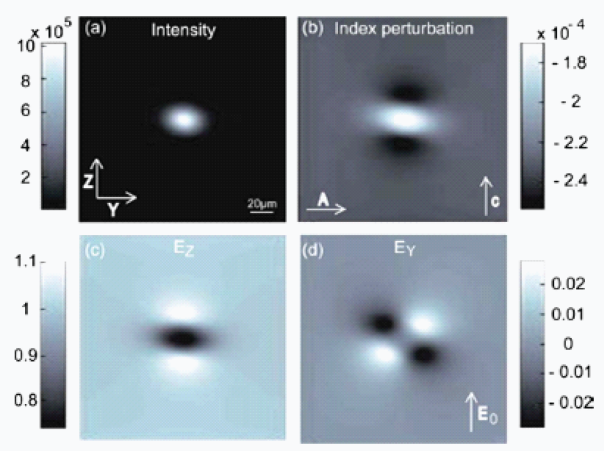

(a) Numerical simulation for the self trapping process relative to an intermediate transient condition. Both the induced refractive index and the transverse intensity profile show the presence of a beam tilting.

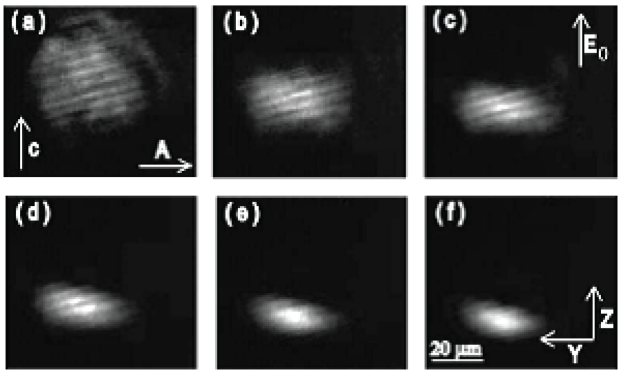

(b) Experimental evolution in the transient regime. The beam tilt is confirmed.

Figure 1.6: Numerical fig.1.6a and experimental fig.1.6b self-trapping process for an ordinary polarized beam propagating along the x direction. The anisotropy effect implies a tilting on the beam spot.

In fig.1.7(a)(b) is reported the output face of the sample for a propagation along the y axis. The light exiting from the waveguide written by an extraordinary visible beam experiences high losses for both the infrared

beams, so demonstrating that refractive index contrast is not high enough to guide them.

Same measurement but with a waveguide written by an ordinary polarized visible beam, fig.1.7(c)(d). In this case the confinement is much better. This demonstrates that, in spite of the longer time required for the space charge field to build up, the photovoltaic contribution decreasing allows a better confinement, consequence of the increased refractive index contrast.

As regards the photovoltaic field amplitudes used for numerical simulations, $E_{ph} = 35kV/cm$ and $E_{ph} = 24kV/cm$, they can be employed to derive the corresponding photovoltaic tensor constants. In fact, provided that the material is always the same, by substituting them in the proper expression for E_{ph}, derived in section 1.4.1 ($\beta_{ph}\xi N_A/(e\mu s)$), the ratio between β_{33} and β_{13} can be found. In the discussed case, $\beta_{33}/\beta_{13} = 1.46$ and it is in agreement with values found in literature [74]: $\beta_{33} = 4 \cdot 10^{-9}$cm/V and $\beta_{13} = 2 \cdot 10^{-9}$cm/V, so confirming the initial hypothesis validity.

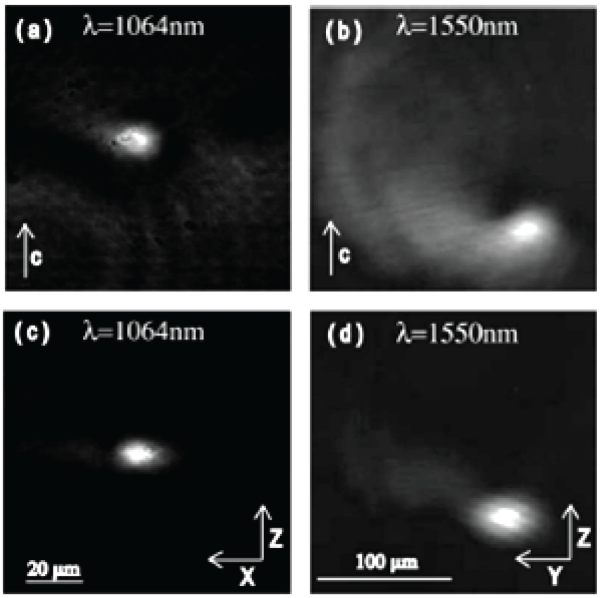

Figure 1.7: Guiding capability test using infrared probe beams at 1064 nm and 1550 nm. In (a) e (b) for a guide written with extraordinary polarization and in (c) and (d) with the ordinary one.

Chapter 2

Solitonic waveguide-based active devices in lithium niobate

In the previous chapter we have seen that spatial soliton waveguides are optimized for light propagation due to their self-written nature. More specifically, they show transverse monomodality for the writing wavelength with very low propagation losses. With reference to the lithium niobate specific case, they are indeed 3D structures resulting quasi-fixed thanks to the very long dielectric relaxation time of the material. Up today, even if in literature many devices have been proposed based on solitons, no real hardware have been realized.

In a very general configuration, every integrated photonic circuit would require an integrated light source. For such purpose, soliton waveguides are ideal candidate for the realization of active devices. In fact due to their ultra-low propagation losses, very efficient amplifiers and/or lasers can be built within them; moreover, thank to the 3D nature of the solitonic technology, even matrices of amplifiers and lasers could be realised as well, going towards intrinsically parallel photonic circuits. The realisation of active devices requires to make lithium niobate able to provide an optical gain, so a proper dopant must be added. The choice of this material depends on the emission band and working wavelength of the photonic circuits. We have to stress here one more time that lithium niobate will only be the host medium inside which all devices and circuits would be realized. Lithium niobate can supply the photorefractive nonlinearity as the tool to write circuits providing that the used light is absorbed by it. Thus, an ideal scheme of photonic

circuit would foresee a working wavelength which should not perturb the written circuit and that should be directly interfaced with other optic and photonic circuits, like for example optical fibres. Among all the possibilities, the ideal working regime would see the range around 1550 nm as the best wavelengths for a signal processing integrated circuit, being this wavelength in the third transparency window of silica and consequently of optical fibre networks. Clearly, a working problem becomes dominant here: how can we realize a self-written circuit if the host medium is not sensitive to the working wavelength. In fact, photorefractivity in lithium niobate is not efficient at infrared frequencies. The whole thesis will show bright technological solutions for such problem. We shall start with the easiest one, for which a first laser beam, absorbed by the host medium, is used to realize the soliton waveguide.

In order to realize integrated emitters or amplifiers within soliton waveguides, we have chosen to dope lithium niobate with erbium ions. Erbium offers many absorption and emission lines, but is one of the most efficient active medium with emission around 1530nm. For this reason it has been largely used for doping glasses [75, 76], fibres [77, 78] and consequently for realizing lasers and amplifiers within them. Femtosecond laser systems in optical fibres are now commercially available as well (see for example the Uranus series of Polaronyx Inc. (http://www.polaronyx.com/Uranus_introduction.htm). Laser sources in erbium-doped lithium niobate waveguides have already been realized using traditional technologies for waveguide realization, like ion indiffusion. The first integrated waveguide laser in lithium niobate is reported by Brinkmann, Sohler and Suche in 1991 [79, 80]. This device is realized by creating a Ti-indiffusion waveguide after having diffused erbium in a lithium niobate substrate. Different solutions for cavity mirrors have been tested but the more compact is done by coating high reflectivity mirrors, obtained with several TiO_2/SiO_2 layers, on the polished surfaces of the sample. Erbium is pumped with a wavelength, $\lambda = 1408$nm, which grants a good mode matching with the emitted one at $\lambda = 1532$nm, 1563 and 1576nm, according to the polarization of the light with respect to the optical axis of the substrate. Many upgrades have been reported during last years, and this basic device has been used to build more complex structures. For example, a modelocked $Er : Ti : LiNbO_3$ laser [81], in which the cavity is realized by Bragg reflectors created by dry-etching technique [82] or directly written in the volume thanks to photorefractive interference patterns [83]. Also wavelength tunability has been

demonstrated [84] by placing the titanium indiffused erbium doped waveguide between an acousto-optical filter and a frequency shift compensator, both integrated on the substrate.

A big improvement to the state-of-the-art is here proposed by using soliton waveguides. It will be possible to access the third dimension, for example to write several guides and thus lasers working in parallel. Again, a key role will be played by very low propagation losses. Clearly, when such technology is introduced, the first important question is: how the photorefractive nonlinearity works in presence of erbium doping. Will erbium incorporation modify the electro-optic properties of the doped material with respect to the undoped one? This is a fundamental point, which is even more stressed by the 3D geometry of solitons. In fact, erbium doping of the host material should cover the whole volume and not only a thin slab around the crystal surface. Thus, the manifold technologies are here connected: the volume doping of the material, its electro-optic characterization and the soliton-waveguide writing. All such steps will be followed in this chapter where initially, it will be investigated and demonstrated that erbium doping indeed influences all the photorefractive properties of the host lattice. I shall experimentally measure the electro-optic coefficient r_{33} as well as the photovoltaic field E_{PV}, performing a systematic characterization by varying the dopant concentration for a photorefractively absorbed wavelength. A microscopic model is also introduced for erbium incorporation so to describe the nature and quantity of defects that the erbium presence generates. Then light self-trapping in such doped material will be experimentally analysed as function of erbium concentration. Achieved results confirm the proposed model validity. Finally, taking advantage of a very special behaviour of erbium as emitter, we shall introduce a new family of spatial solitons induced by luminescence. In fact, to excite the material emission at 1530nm, it is necessary to pump it with a 980nm laser. Lithium niobate does not exhibits any photorefractive response to it (or at least it is extremely weak), thus this wavelength cannot be directly used to write a waveguide. When erbium is pumped by light at 980 nm, according to the pumping intensity only $^4I_{15/2} - {}^4I_{11/2}$ (single-step) or both $^4I_{15/2} - {}^4I_{11/2}$ and $^4I_{13/2} - {}^4F_{7/2}$ (two-steps) transitions may occur. In this last case a green luminescence is consequently induced and it might interact with the host lithium niobate writing a soliton channel. Such result, published in Applied Physics Letters [85], was never observed before and constitute an outstanding output of my PhD work. Such new technology can indeed be successfully used for

realising integrated amplifiers and laser sources in lithium niobate crystals doped in volume with erbium.

2.1 Material characterisation: Erbium volume doping via the Czochralski technique

The whole set of erbium doped samples that have been used for the presented measurements, have been provided by the group led by dr. Cinzia Sada (Physics Department of the Padova University) in the framework of the PRIN project *"Amplificatori e sorgenti laser integrati in guide solitoniche in* $Er:LiNbO_3$ *"*. Erbium bulk doped lithium niobate crystals were grown by the Czochralski technique [32, 33] along the Z-axis with a pulling rate $v_p = 3$ mm/h and with a rotation rate $\omega \simeq 30$ rpm. Erbium concentration in the starting melt composition was chosen to be in the range $0.0 - 0.7$mol.%. Boules were poled by applying a constant current density of about 3 mA/cm^2 while they were cooled from the paraelectric to the ferroelectric phase, in order to achieve a single domain state through all the sample volume. Samples were then oriented by exploiting the X-ray diffraction technique and cut in slices with the major surface perpendicular to the Z direction. Slices were annealed in air at 950°C for 6 h to remove eventual color centres and dislocations. Finally, they were optically polished using a Logitech PM5 lapping machine with standard techniques on the Z, X- and Y faces. The typical dimension of the final samples are about 8 mm along the Y propagation direction, 6 mm along the X one, and 1 mm along Z, the optical axis. For the following characterizations, a selection of five samples of nominal concentration $0, 0.1, 0.3, 0.5$ and 0.7mol.% were investigated to grant that they were ferroelecric monodomain, using the cross polarized microscopy, and that the residual number of dislocations was as low as what reported for undoped commercial samples from Crystal Technology ($\simeq 1.0 \cdot 10^5 \text{disl} \cdot \text{cm}^{-2}$).

2.2 Material characterisation: r_{33} coefficient measurement

Doping influence on lithium niobate photorefractive properties has been reported for many transition metals [29] introduced in the host lattice to

satisfy the necessity, arose during last years, both to increase and annihilate photorefractivity inside this material. Incorporation of Fe, Cu, Mn, Ni ions, for examples, produces an increasing of deep trap levels in the band-gap so to increase the photorefractive absorption in the visible range. On the contrary, Mg, Zn, In, Hf, Zr ions are able to reduce the number of intrinsic defects (antisite niobium Nb_{Li} or niobium occupying lithium positions) in the lattice so preventing the space charge field to come up. Often, and for low enough concentrations that is characteristic of the used dopant, these ions tend to enter the lattice occupying lithium positions. According to literature in fact, electro-optic coefficient, as the other photorefractive properties, is influenced by the presence of such ions and by the lithium quantity in the melt. Actually, in [86], an investigation about the change in value for both r_{13} and r_{33} for stoichiometric and congruent samples is reported. It is demonstrated that, in correspondence to a lithium concentration decreasing, the r_{33} decreases while the r_{13} remains almost unchanged. In addition, in [87–89], doping mechanism effects on photorefractivity are reported, and they are based on the substitution of dopants in lithium sites and in turn on the effects of Nb_{Li} concentration. More specifically, the electro-optic coefficient behaviour has been studied, to cite some examples, for Zinc [90], Chromium [91] and Iron [92], by varying the dopant concentration. For small dopant amount, a decreasing is found but, above a certain threshold value (material dependent), it can increase again, as for [90] in which this behaviour is more evident.

Unlikely to what reported for transition metals, very few is known about the influence of rare earth doping on photorefractivity as, because of its chemical nature, these ions are expected not to influence the electrical proprieties involved in these nonlinear processes. Many structural investigations have been performed to identify erbium occupancies in the lattice. As reported in [93–97], it has been found that these trivalent ions tend to occupy lithium positions with a small shift along the $\hat{c}$ axis of about 0.46Å. This hypothesis keeps for small dopant concentrations which is actually the case for all the further described measurements. This is usually justified as to be a consequence of their larger ionic radius and their stronger electronegativity. This substitutional incorporation, often found also for transition metals, could cause some influence on photorefractivity as well. Up today, in my knowledge, only one paper exists about the investigation of the electro-optic coefficient in erbium doped lithium niobate [98]. This study is related to a proton exchange waveguide, so only a superficial structure, which is reported

to suffer from being characterized by erbium clustering. This configuration could alter the measurement results both as a consequence of energetic interactions between these aggregated ions and because of anisotropic variations induced on the cell parameter.

In this section the analysis of the r_{33} coefficient (1.3), in uniformly grown erbium doped lithium niobate, is taken into account [99]. The reason for which only this coefficient has been considered is related to the fact that it is the strongest exhibited by lithium niobate and is usually considered as the most favourable for spatial soliton formation. To exploit the behaviour of the r_{33} electro-optic coefficient and in turn its dependency from the dopant concentration, a Mach-Zehnder-based interferometric scheme has been built, fig. 2.1. As source, a He-Ne laser has been used so to work in an absorption regime which is not resonant with erbium ions transitions. In other words to have results regarding only the host lattice response so to compare them directly with what is known about the pure, congruent, material. This source has been mode-cleaned with a spatial filter, collimated and enlarged with a telescope, extraordinarily polarized and divided in two arms. The generated two beams will acquire a relative phase shift provided by the propagation inside the $Er : LiNbO_3$ sample placed in one arm. The sample is hold between two metallic electrodes so to apply a bias voltage along the $\hat{c}$ axis direction. The two beam recombination is then analysed by imaging on the sensor of a CCD camera the consequent interference pattern that they form inside the BS2 beam splitter. The choice of this source is justified by its high degree of coherence (several centimetres) and its transverse monomodality (TEM_{00}) which grants good quality and high contrast interference fringes.

The bias voltage necessary to induce a variation of 2π on the generated pattern [100], allows to calculate the corresponding value for the electro-optic coefficient. Being the applied voltage constant, then this procedure permits to measure the DC r_{33} coefficient. For a sample having a length equal to L and a thickness h, the phase shift acquired by the beam propagating inside the medium, which exhibits a refractive index variation $\delta n = 1/2 r_{33} {n_e}^3 (V_{bias}/h)$, is $\Delta\phi = 2\pi\delta nL/\lambda$. So in correspondence to a 2π phase shift:

$$r_{33} = \frac{2h\lambda}{L{n_e}^3 V_{2\pi}} \tag{2.1}$$

Each calculated r_{33} value is the result of 20 averages performed in five different positions in the volume (and not only close to the surface) of each sample. This procedure grants measurement reproducibility and the demon-

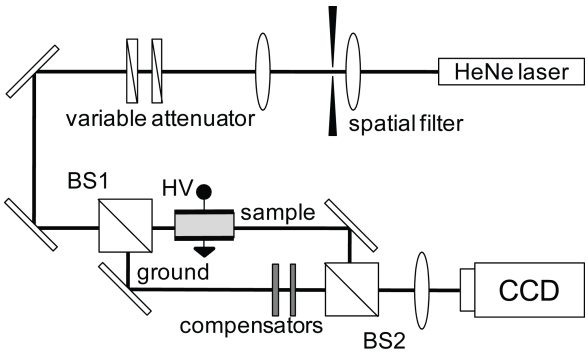

Figure 2.1: Setup employed to calculate the voltage $V_{2\pi}$ necessary to shift by 2π the interference fringes and thus to calculate the r_{33} coefficients in $Er : LiNbO_3$.

stration of sample uniformity, at least from the photorefractive point of view. To ensure a high enough accuracy for the calculated values of r_{33}, some experimental solutions have been taken into account. As the nonlinear phase shift is provided by a photorefractive material, light can generate a space charge field in the illuminated region where the photovoltaic effect can be excited and strongly alter results. To avoid such problems light intensity has been kept lower than 5 nW, as reported in [86]. Neutral filters are placed along the second, unaffected, beam to equilibrate light intensities and to obtain a fringe visibility up to 95%. If a residual photovoltaic field was still present and fringes were perpendicular to the $\hat{c}$ axis direction, an eventual fringe shape modification would have strongly influenced the measurements. So the beams have been aligned in order to make them appear parallel to the $\hat{c}$ axis and to have a separation of about 65 μm between them. The system resolution was high enough to: well discriminate fringe dimensions, thanks to the small pixel CCD sensor size ($4.65 \times 4.65 \mu m^2$), to verify fringe distribution uniformity and to determine $V_{2\pi}$ with a high enough accuracy.

A full characterization of all the available samples having concentrations ranging between 0.0 mol.% and 0.7 mol.% is reported in fig. 2.2. Points indicate the existence of a general monotonically decreasing trend, at least in the limit of the analysed concentrations.

It is worth noticing that in correspondence to a concentration $\rho_{Er} \simeq 0.2$ - 0.3 mol.%, a trend change appears. For these values also all the other

photorefractive measurements, that will be shown after, indicate a particular behaviour.

The used dashed line is not just a guide for the eyes, fig. 2.2. It is drawn according to the final considerations that will be presented in section 2.5 where the model describing a possible mechanism for erbium incorporation in the lattice will be presented.

The application of this technique to measure the r_{33} value for the undoped commercial congruent sample from Crystal Technology, allowed to find the value $r_{33} \simeq 29.6$ pm/V which is quite in agreement with the one ($r_{33} \simeq 30 - 33$ pm/V) reported in the datasheet [69] and in literature [20] in general, so demonstrating that these measurements are characterized by a very high precision and accuracy.

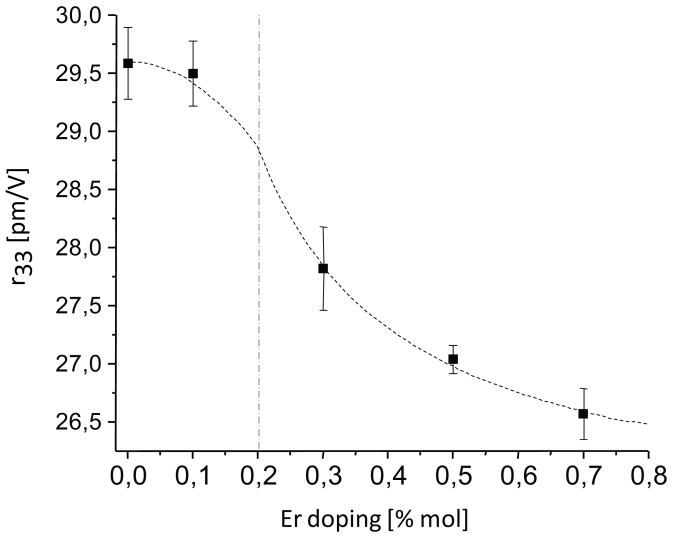

Figure 2.2: Values for the r_{33} coefficients for different values of erbium concentration. The trend, described by the guide for the eyes, is drawn according to the model for erbium incorporation that will be discussed in section 2.5.

2.3 Material characterisation: photovoltaic field ($\mathbf{E_{PV}}$) measurement

As already mentioned in the first chapter, where the main aspects regarding the photorefractive effect have been discussed, the photovoltaic effect is concurrent to the self-trapping process, so it represents a key parameter involved in the overall solitonic waveguide formation. As its physical origin is related to the alignment of the lithium and niobium atoms along the $\hat{c}$ axis, it is expected that the substitution of a lithium atom with an erbium one will produce some influence also on the photovoltaic field. Furthermore, being this changing in the atom distribution dependent on the dopant concentration, also the photovoltaic effect could be dependent on it, as verified for the r_{33} coefficient. Here the analysis of the E_{PV} dependency on erbium concentration is performed in terms of the photorefractive response of the doped material [101].

To investigate this dependency, a He-Ne laser was focused on the input face of the doped lithium niobate samples, with a waist $w_{in} = 20$ μm and a constant intensity $I_{em} = 0.96$ W/cm^2. Again, as done for the r_{33} measurement, a wavelength which was not directly absorbed by erbium ions has been used in order to take into account only the host lattice response in presence of doping. An extraordinary polarized (optical field oscillations along the $\hat{c}$ axis) beam was let propagate perpendicularly to the sample optical axis and an imaging optical system was used to conjugate the output face of the sample on the sensor of a computer controlled CCD camera. The free evolution of beam diffraction, without applying any bias electric field to the sample, was then studied at the output face.

Being the photorefractive nonlinearity concurrent effect (self-trapping) not excited, only the dynamics of the photovoltaic internal field is taken into consideration. Moreover, in this way its saturation value ($E_{PVt\to\infty}$) is exploited. The setup used for this analysis is reported in fig. 2.3.

As diffraction dynamics is driven by the photovoltaic effect, only the beam size along the $\hat{c}$ axis will change, because of the appearing of a charge current directed along it. The trend for the waist evolution along the optical axis direction can be found, as reported in fig. 2.4 for a doping level of 0.3 mol.%.

The analysis of this trend (quite general for all the investigated samples), shows that waist variation is very fast at the beginning of the measurement

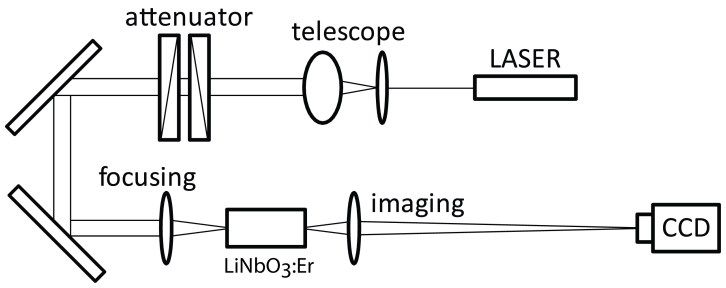

Figure 2.3: Sketch for the experimental setup employed to investigate the nonlinear free evolution of the beam when only the photovoltaic effect is taking place in the erbium doped lithium niobate sample.

when the photovoltaic field starts to build up, and then it reaches a slower regime corresponding to quasi-stationarity, for E_{PV} attaining a saturation value.

To determine the steady state value for the photovoltaic field starting from the waist evolution curve, the theory proposed by Nippus and Claus [102] is used. It deals with a geometrical approach that allows to fit the waist evolution curve simply knowing the initial waist value $w_0 = w(t)_{t=0}$ (relative to the linear diffraction in the material) and the saturation one $w_{max} = w(t)_{t\to\infty}$, according to the relation:

$$w(t) = w_{max} + (w_0 - w_{max})e^{-kt} \tag{2.2}$$

The fitting parameter k is related to erbium incorporation inside lithium niobate lattice by taking into account the dark and photovoltaic photoconductivities, σ_d and σ_{PV} respectively and the dielectric constant along the optical axis $\epsilon_0\epsilon_{33}$, according to the ratio [87]:

$$k = \frac{\sigma_d + \sigma_{PV}}{\epsilon_0\epsilon_{33}} \tag{2.3}$$

Nippus-Claus theory permits also to calculate the refractive index variation induced by the photovoltaic field inside the illuminated region of the photorefractive material. An estimation for the photovoltaic field (E_{PV}) for a propagation length L, can be derived according to the equality:

$$\Delta n_e = 4n_e \frac{\frac{w_{max}}{w_0} - 1}{\left(\frac{L}{w_0}\right)^2} = -\frac{1}{2} {n_e}^3 r_{33} E_{PV} \tag{2.4}$$

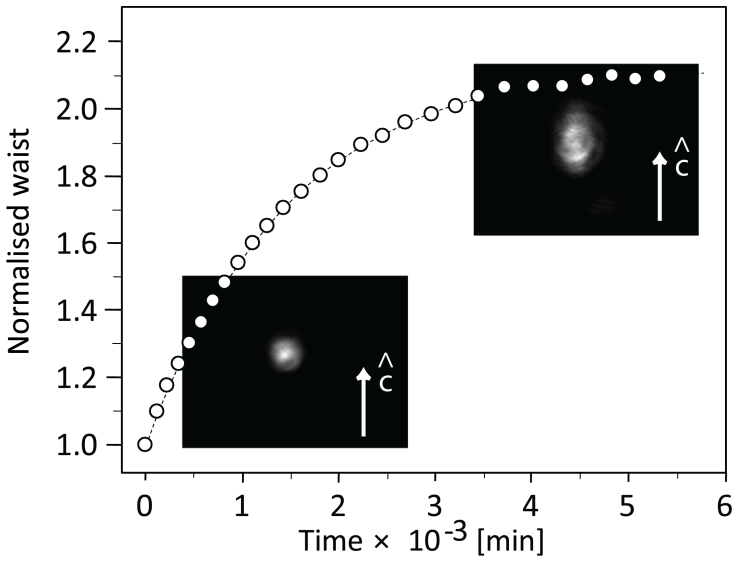

Figure 2.4: Waist evolution along the ĉ axis. Only the photovoltaic nonlinearity is acting on a sample with a doping level of 0.3 mol.% The initial linear diffraction (t=0) is elongated along the optical axis and a saturation value is reached.

Values for the photovoltaic field are calculated using the experimentally found coefficients r_{33}, reported in the previous section. Repeating the procedure for all the samples, a parabolic trend for E_{PV} versus the erbium concentration in the melt is found, as in fig. 2.5. This demonstrates again that erbium incorporation into the lattice modifies the general photorefractive behaviour of the material. The value for the undoped sample in fig. 2.5 is taken from literature [51,103] and fixed to 10^{+6} V/m. This trend shows an initial decreasing which attains its minimum value for an erbium concentration of about 0.3 mol.%. Then, the photovoltaic field starts increasing again so indicating that a different regime occurs with the increasing of the erbium concentration. This concentration value represents a critical point both for the r_{33} and E_{PV} measurements which are completely independent between them apart from having used the same set of samples. This point will be indept in the section 2.5, devoted to the explanation of erbium incorporation by the realization of a proper model. This value will be found again to have a particular meaning when the self-trapping process will be analysed.

In the next section, it will be demonstrated that diffraction compensation speed is maximized exactly in correspondence to this concentration.

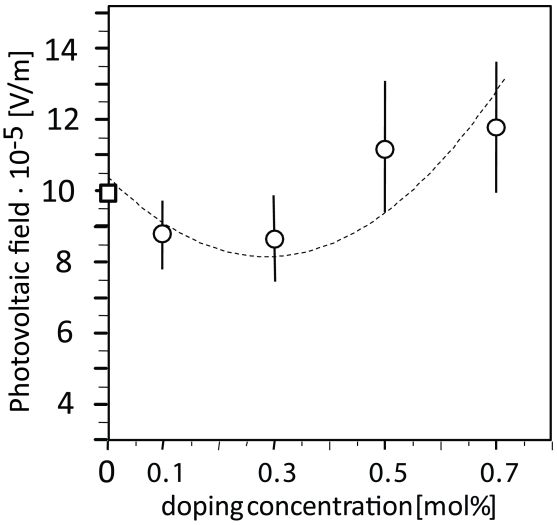

Figure 2.5: Trend for the photovoltaic field for different values of erbium concentration. The parabolic trend presents its minimum for $\rho_{\mathrm{Er}} = 0.3$ mol.%.

2.4 Self-trapped beams in $\mathbf{Er : LiNbO_3}$

It has been demonstrated that erbium ions influence the photorefractive process by modifying the electro-optic coefficient and the photovoltaic field in function of its concentration. It is now necessary to understand if a solitonic waveguide can be obtained in such a material [101], being a waveguide the basic element necessary for an integrated source realization.

Different aspects must be investigated; it is not *a priori* guaranteed that erbium doping permits to self-trapping to be achieved, or at least the formation dynamics could be different from what reported for the undoped case [9]. In fact, being a rare earth element, it should not affect the electric properties (free charge generation rates, diffusion, drift and recombination processes) and thus photorefractivity, but previous results indicate that erbium plays an active role.

To perform these measurements the experimental setup depicted in fig. 2.6 is used. In this case a bias voltage is applied. A duplicated Nd:YAG

laser, 532 nm, is collimated and the extraordinary polarization is selected. Also in this case, the analysis is performed by injecting in the sample a radiation having wavelength not resonant with erbium transitions to exploit lattice response to the dopant introduction. In section 2.7 a new family of solitons will be presented and, for its realisation, erbium transitions will be used. Neutral density filters are necessary to reduce the injected power so to keep light intensity constant and as high as 14.7 W/cm^2 ($\pm$3%) for the beam focused on the input face of the sample with a waist of $\simeq 8$ μm. The beam propagates along the $\hat{b}$ direction, fig. 2.6, and a bias electric field can be applied along the optical axis. Formation dynamics are again studied using a camera and an imaging optical system granting also a magnification of 22 times of the output face of the sample on the sensor.

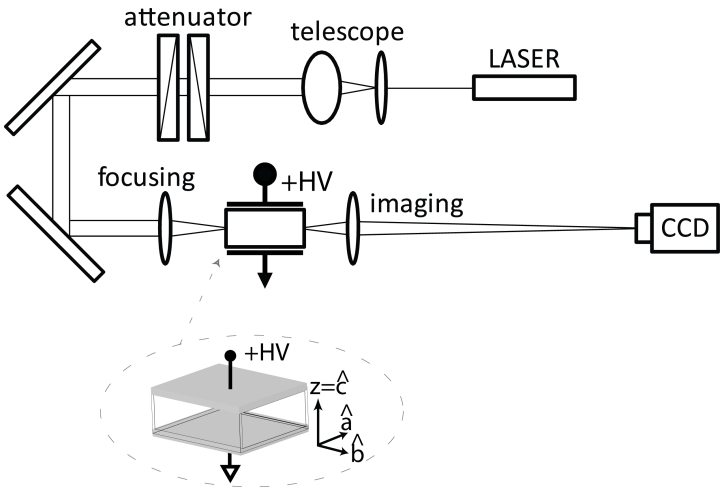

Figure 2.6: Sketch for the experimental setup employed to investigate the self-trapping process in the whole set of the erbium doped lithium niobate samples.

The first performed measurements, to be considered as reference, are intended to investigate self-trapping in undoped samples, both commercial and growth in the University of Padova.

Then, self-trapping has been characterized both in terms of erbium concentration, with the same sample set used for previous measurements, and by changing the bias electric field E_{bias} =15, 20, 30, 40 kV/cm. In fig. 2.8,

beam waist evolution at the output face of the sample is depicted for a bias electric field of 30 kV/cm. This value for the bias field is the one that allowed to get the best self-trapping for all the samples. It is with reference to this value that all the self-confinement measurements will be reported.

By observing waist evolution at the output face of the sample, fig. 2.7, the typical behaviour described in [9] can be recognized. The circular diffracted beam become elliptical along the fast, $\hat{c}$ axis, direction after the application of the bias electric field, and then self-traps, reaching a circular shape. The final dimension becomes comparable to the one at the input face after about 90 min − 100 min.

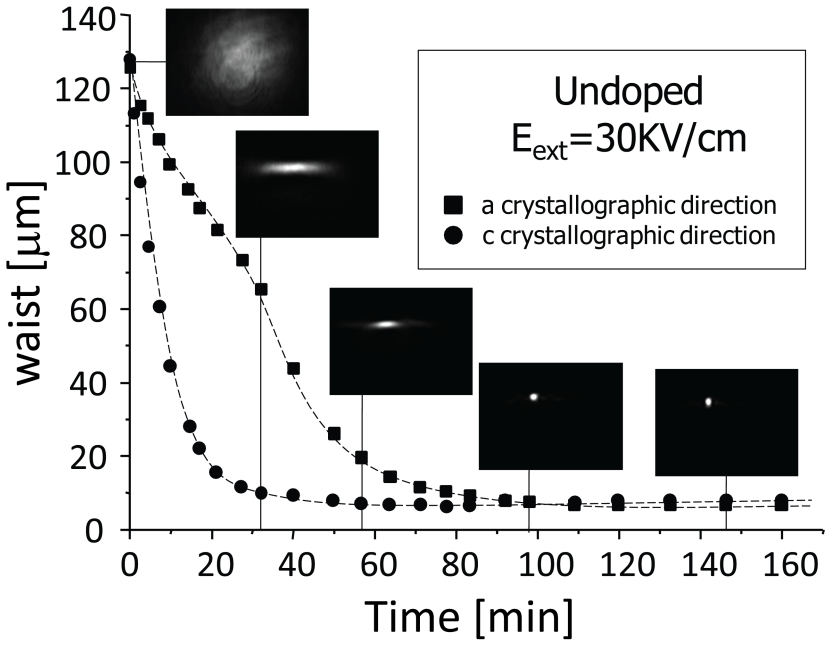

Figure 2.7: Self-trapping waist evolution for the undoped sample for a bias electric field of 30 kV/cm.

The same procedure is repeated for all the doped samples. In fig. 2.8 are depicted the waist evolutions for the four concentrations: $\rho_{\mathrm{Er}} = 0.1, 0.3, 0.5, 0.7$ mol.% in correspondence to the same bias field as for the undoped case: 30kV/cm. From these measurements it is clear that self-trapping can always be achieved whatever the employed concentration. As for the undoped case,

two different self-trapping speeds can be distinguished: a fast one, along the ĉ axis and a slower one, along the â direction. Ellipticity looks to be reduced in comparison with the undoped case. So the main objective has been demontrated: self-trapping in erbium doped lithium niobate is still possible and in turn a waveguide having a solitonic profile can be written in the material. From this point of view, erbium does not look to change the whole photorefractive process dynamics, but further informations can be deduced from these measurements. Actually a first point is related to the time necessary to obtain the complete beam self-focusing (quasi stationary regime) as it results to be concentration dependent.

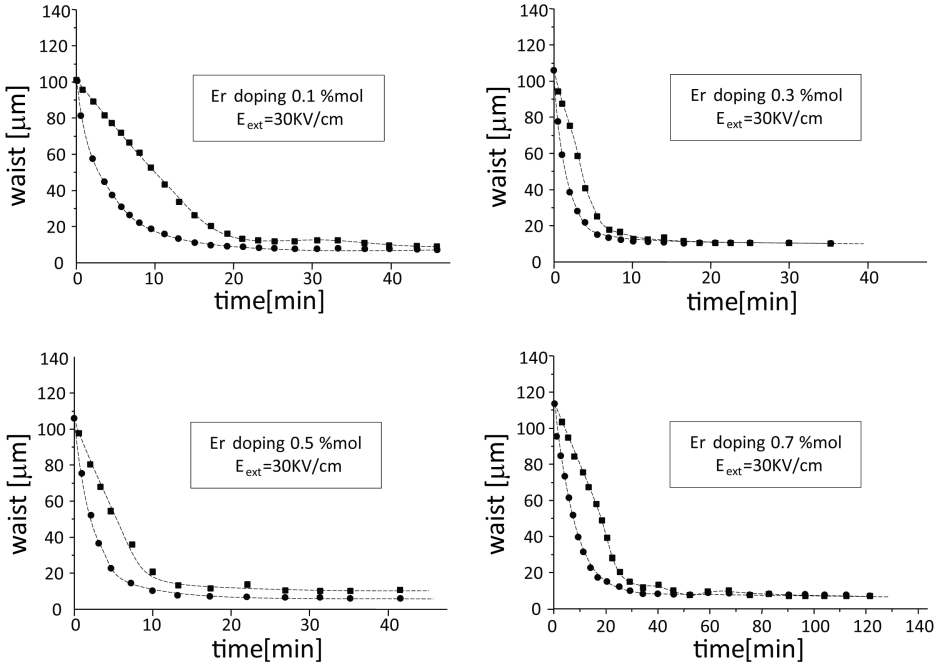

Figure 2.8: Self-trapping waist evolution for erbium doped samples having concentrations 0.1, 0.3, 0.5, 0.7mol.% and for a bias electric field of 30 kV/cm.

Fitting the transverse experimental beam shape at the output face of the sample with a dedicated 2D fitting code, all the time constants τ characterizing the self-confinement process along the fast (optical axis) direction

have been measured. By plotting them versus the applied bias electric field values, a monotonic decreasing trend can be found, fig. 2.9. It obeys to the law:

$$\tau(E_{bias}) = \tau_L \frac{a + {E_{bias}}^2}{b + {E_{bias}}^2} \tag{2.5}$$

where τ_{L} represents the limit time to which all the measurements tend at the increasing of the bias electric field. The best fit is obtained for $\tau_{\mathrm{L}} = 1.3$min.

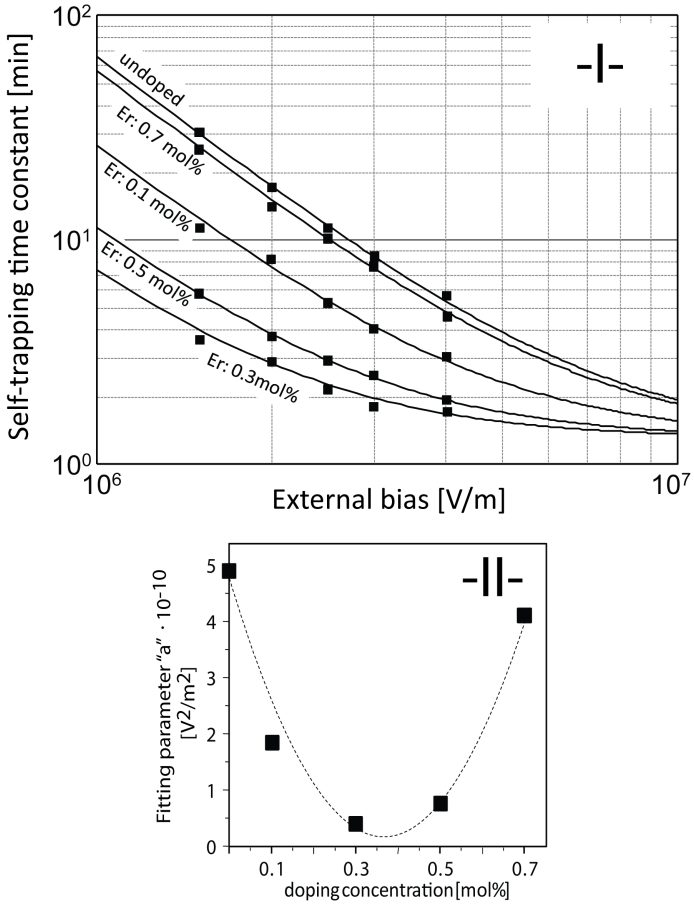

Figure 2.9: -I- Self-trapping time constants τ along the fast ĉ axis in function of the bias electric field. -II- Parabolic trend for the "a" fitting parameter showing a minimum for $\rho_{\mathrm{Er}} = 0.3$ mol.%

The parameter "b" does not affect the fit function, while the "a" one has a parabolic trend, fig. 2.9 -II-. The fastest self-trapping process is provided by the sample having a concentration $\rho_{Er} = 0.3$ mol.%. This is not surprising as the measured photovoltaic field results to be minimized exactly for this concentration. Thus, for a fixed value of the bias electric field, the screening one results to be more efficient than in all the other cases. It is worth noticing that this measurement is completely independent from those performed to calculate the E_{PV}, so this result represents another verification of measurement quality.

Another parameter to be analysed, and that will be proved to be the key brick to verify all the performed measurement at the same time, is the the final waist size in condition of maximized self-confinement, along the fast direction.

At a first glance, the curve trend corresponding to each bias electric field plotted in function of the erbium concentration, fig. 2.10 -I-, shows only small oscillations around the average value. Two informations can be deduced. Actually by increasing the bias electric field, the final size reduces more and more accordingly and, in addition, for each electric field value, in correspondence to the 0.3mol.% concentration this dimension is always the smaller. This might be a consequence of the minimum value for the photovoltaic field. So it might be inferred that oscillations around the average value could be not a measurement error, but a consequence of the E_{PV} oscillatory behaviour influence weighted by the corresponding value of the r_{33} parameter.

If the same waist values (considering all the examined erbium concentrations and for all the applied bias fields) are plotted versus the proper refractive index value, we find that all of them follow the same trend, fig. 2.10 -II-, with very small deviations. This is a clear indication of how good are all the performed measurements, in fact refractive index variation is not theoretical but is calculated considering the experimentally found values for E_{PV} and r_{33} which carry with them all their measurement errors. For negative values of δn, the photovoltaic field is predominant and according to the measured parameters, the induced refractive index variation can arrive up to $5 \cdot 10^{-4}$.

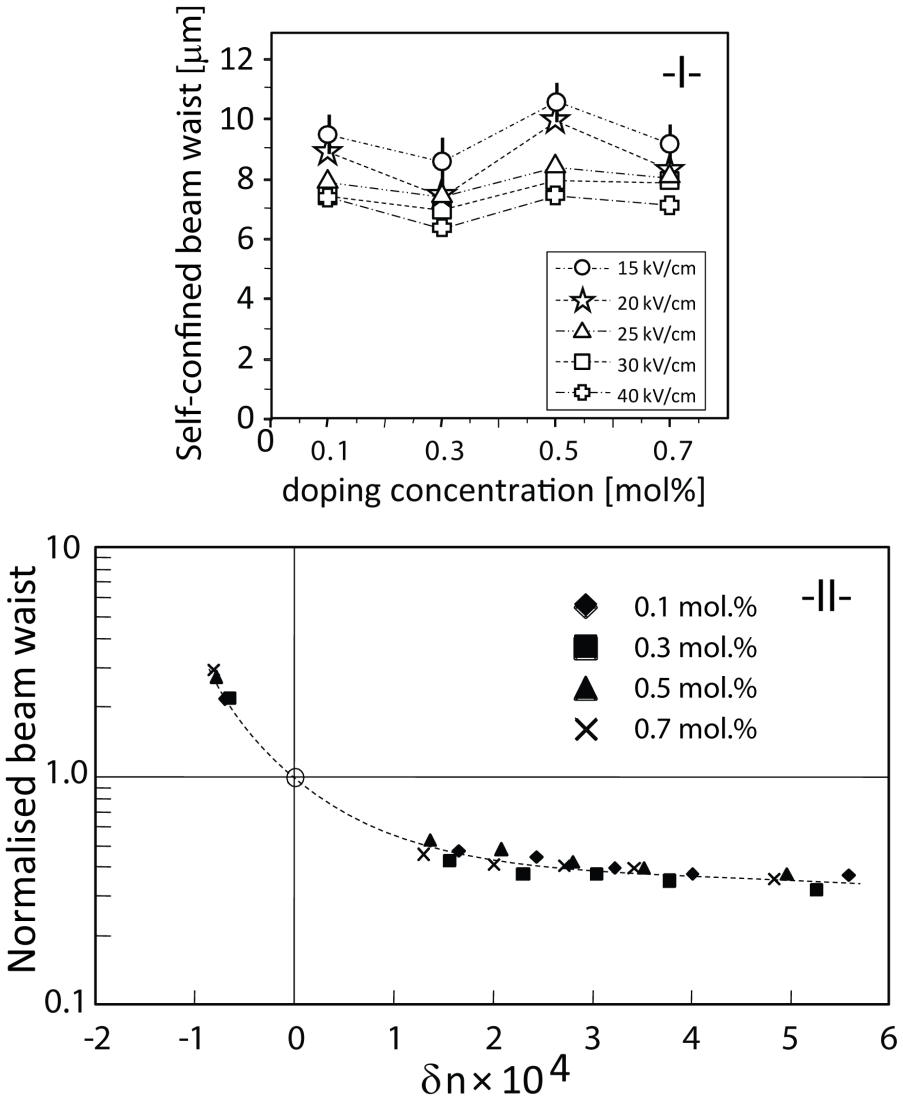

Figure 2.10: Final waist size along the fast ĉ direction. In -I- with respect to the doping concentration. In -II- with respect to the induced refractive index variation which is calculated using the experimentally found parameters. In both cases, all the concentrations and bias electric fields have been considered.

2.5 Microscopic structure and defects-based erbium incorporation model

Previously discussed experimental measurements demonstrate that erbium ions change the photorefractive radiation-matter interaction even if these trivalent ions should not influence the electrical (charge based) processes occurring when the material is shined by a laser beam. Actually, the microscopic interaction has not yet been taken into account, so what is measured is only the macroscopic effect associated to the charge build-up in time. Moreover, erbium ions are forced not to interact, from a spectroscopic point of view, having chosen wavelengths not absorbed by them but only by the host lattice.

These results can be resumed remarking the main parameters. As regards the electro-optic coefficient r_{33}, a variation of about 10% has been found between the value for a congruent commercial sample and the doped samples growth by the group of the University of Padova and a trend inversion appears in correspondence to the $\rho_{\mathrm{Er}} = 0.2 - 0.3$ mol.%, fig. 2.2. The photovoltaic field is characterized by a parabolic trend for which the maximum variation is in the order of 35% with a trend minimum at 0.3 mol.%. Also self-trapping (photorefractive versus the concurrent photovoltaic effect) results indicate a maximized speed in waveguide formation and a minimum waist size for the same concentration value. So this looks not to be only a coincidence.

A further useful analysis has been done by the group of Padova and it deals with the measurement of the elementary cell parameter for both the undoped and doped samples. This experimental investigation, conducted by means of the (0 0 12) X-ray diffraction technique, shows that the cell parameter along the $\hat{c}$ axis, decreases monotonically and linearly with the increasing of erbium concentration, fig. 2.11. The trend is in agreement with the Vegard's law [104] that is to say the linear relationship between the dopant concentration and the lattice constant parameter. Furthermore, samples resulted to be uniform in the whole volume, so the presence of erbium clusters can be excluded (at least within the limits of this kind of analysis).

A commercial Cristal Technology sample has been employed as reference. For it, the cell parameter resulted to be $C_{\mathrm{pure}} = (13.86655 \pm 0.00014)$ Å. The linear fit of the experimental points gives (13.86621 ± 0.00008) Å for the

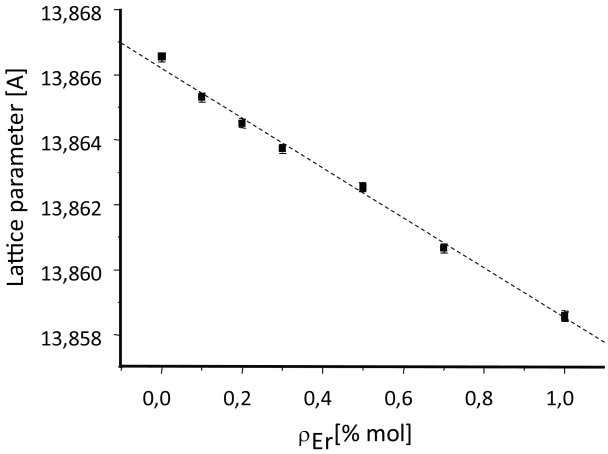

Figure 2.11: Cell parameter measured along the ĉ crystallographic direction as a function of the erbium concentration.

undoped and a slope of (-0.0077 ± 0.0001) [Å/mol%] to take into account the doped ones.

The linear decreasing of the cell parameter along the optical axis could be interpreted as an erbium incorporation occurring always in the same site type, at least up to 1 mol.%. Actually, this hypotesis is in agreement with literature as it is reported by many authors [93–97] that the rare earth element erbium, as many metals, tends to occupy lithium sites. Erbium shifts along the optical axis ($-\hat{c}$ direction) of about 0.46 Å. This shifting could be consequence of the erbium ionic radius which is larger than the lithium one (176 pm versus 152 pm). Also the electronegativity difference could explain the reduced size of the cell parameter, as with the incorporation of erbium, it increases from 0.98 Pauling to 1.24 Pauling. Starting from this considerations, a model describing the defect structure for erbium doped lithium niobate has been developed [99] for concentrations ranging between 0.0 mol.% and $0.7 - 1$ mol.%.

Many authors reported the intrinsic defects as responsible for the changes in lithium niobate photorefractivity properties and many models have been proposed [105–111]. The ratio between lithium and niobium concentrations, eq. 2.6, in congruent samples, ranges from 48.5 mol.% and 50 mol.%, the

stoichiometric condition.

$$X = \frac{[Li]}{[Li] + [Nb]} \tag{2.6}$$

Many lithium sites are empty, about 6% for X = 48.6%, and because of the close ionic radius value of niobium, it tends to displace into a lithium position, so forming an anti-site niobium intrinsic defect (Nb_{Li} or Nb^*). As the charge neutrality must always be kept, three options to compensate for these defects are possible: oxygen vacancies, lithium vacancies in lithium sites or niobium vacancies in niobium positions. From density measurements the hypothesis of the oxygen vacancies must be discarded as with the decreasing of lithium concentration, the density increases and this is not compatible with the presence of oxygen vacancies [106,112,113] as proposed by [114]. On the contrary this supports the hypothesis of Nb^* formation.

Maintaining the same formalism as in [105,109,111], when passing from a stoichiometric to a congruent concentration, a set of intrinsic defects are created. To grant the electric neutrality, the material needs five cells instead of one, according to the chemical expression 2.7. It resumes what extensively reported in the table 2.1 which show the intrinsic defect structure in comparison with the stoichiometric one.

$$[Li_{1-5d}\ Nb_{5d}{}^*]\,[Nb_{1-4d}\ VNb_{4d}]\,O_3 \tag{2.7}$$

Electric charge	0		+4	-1
	Li		Nb^*	Nb^*
	Nb		Nb	0
	O_3		O_3	O_3
n° of cells	1		1	4

Table 2.1: Intrinsic defects (anti-site niobium) distribution in a congruent sample composition compared to the stoichiometric one. The number of cells, 5, necessary to grant charge neutrality along with the single cell electric charge are indicated.

According to what said before about the cell parameter, erbium incorporation looks not to change the lattice disorder with the increasing of its concentration, as the cell parameter decreases linearly. To introduce erbium

effect in the model, the hypothesis of new defects generation with an ordered lattice is done. In other words the same intrinsic defect configuration, as for the congruent case, is assumed to appear in presence of erbium doping for the concentration range under investigation $\rho_{\mathrm{Er}} \in [0.0, 1]$ mol.%.

For an erbium concentration $\rho_{\mathrm{Er}} < 0.2$ mol.%, new niobium anti-site intrinsic defects are created; lattice is reorganized, and erbium enters it for substitution into lithium sites as many of them are empty and so available. This is summarized by the expression 2.8. To compensate electrically for the erbium introduction, three cells are necessary. In table 2.2, the comparison with the stoichiometric and the congruent cases is reported. The defect number estimation, again according to the formalism in [105,109,111], shows a linear decreasing with the erbium concentration increasing. The cell parameter has also a linearly decreasing trend, so a quadratic change for the electro-optic coefficient can be inferred. Actually this result is in agreement with the first part, 0.0 mol.% $< \rho_{\mathrm{Er}} <$ 0.2 mol.%, of the experimental points reported in figure 2.2.

$$[Li_{1-5d-3x}\ Nb_{5d+2x}{}^{*}\ Er_x]\,[Nb_{1-4d-2x}\ VNb_{4d+2x}]\,O_3 \tag{2.8}$$

Electric charge	0		+4	-1		+4	-1	-3
	Li		Nb*	Nb*		Nb*	Nb*	Er
	Nb		Nb	0		Nb	0	0
	O_3		O_3	O_3		O_3	O_3	O_3
n° of cells	1		1	4		1	1	1

Table 2.2: Intrinsic defects and erbium distribution when a low dopant concentration ($\rho_{\mathrm{Er}} < 0.2$ mol.%) is added to the melt. The new cell configuration is compared to the stoichiometric/congruent one and the number of cells, 3, necessary to grant the charge neutrality along with the single cell electric charge are indicated as well.

Increasing erbium concentration, up to the limit $\rho_{\mathrm{Er}} < 0.8$ mol.%, it is supposed not to create new defects but to "use" the already present ones. This implies that the overall number of defects decreases with erbium concentration increasing, so a saturating trend is expected. In addition, as a consequence of the cell parameter linear decreasing, an overall saturating decreasing trend for the r_{33} is reasonable. For intermediate concentrations this behavior is described by the expression 2.9, being x + y the new erbium

concentration. For $0.4\,\text{mol.\%} < \rho_{\text{Er}} < 0.8 - 1\,\text{mol.\%}$, a much more stable configuration is achieved and can be described by the cell configuration in table 2.3 and consequentely by the equation 2.10.

$$[Li_{1-5d-3x-3y}\ Nb_{5d+2x}{}^{*}\ Er_{x+y}\ VLi_{2y}]\,[Nb_{1-4d-2x+3y}\ VNb_{4d+2x}]\,O_3 \quad (2.9)$$

$$[Li_{1-4z}\ Nb_z{}^{*}Er_{3z}]\,[Nb_{1-2z}\ VNb_{2z}]\,O_3 \quad (2.10)$$

Electric charge	+4	+2	-3
	Nb^{*}	Er	Er
	Nb	Nb	0
	O_3	O_3	O_3
n° of cells	1	1	2

Table 2.3: Intrinsic defects and erbium distribution when a high enough dopant concentration ($0.4\text{mol. \%} < \rho_{\text{Er}} < 0.8 - 1$ mol.%) is added to the melt. The number of cells, 4, necessary to grant the charge neutrality along with the single cell electric charge are indicated as well.

2.6 Erbium spectroscopic properties

From a spectroscopic point of view, erbium doped lithium niobate presents absorption and emission lines which are not present in the undoped material. In particular, in fig. 2.12, the absorbance (OD) spectrum for an erbium doped sample is reported highlighting the corresponding name for transition levels. In fig. 2.13, the complete set of levels and possible transitions (absorption, radiative and nonradiative emissions) are emphasized, [115, 116]. When pumped at 980 nm, erbium gives the opportunity of having radiative emission and optical gain in the infrared band at 1530 nm through the transition $^4\text{I}_{13/2} \rightarrow {}^4\text{I}_{15/2}$, so at telecom wavelengths. Because of this feature, this dopant is very promising for the realisation of integrated active waveguide-based sources. As anticipated, integrated lasers have already been realized by using a pumping scheme at 1480 nm in waveguides obtained via Ti indiffusion, so just superficial guiding structures. What will be proposed in the following is the big evolution that a volumetric, light self-written, waveguide

can offer. In this way, multiple and working in parallel monomodal emitting devices can be written in the bulk. Apart from the 3D technological realization, solitonic waveguides are characterized by propagation losses which are extremely low, about one order of magnitude less than what offered by the other technologies, so population inversion should be more efficient.

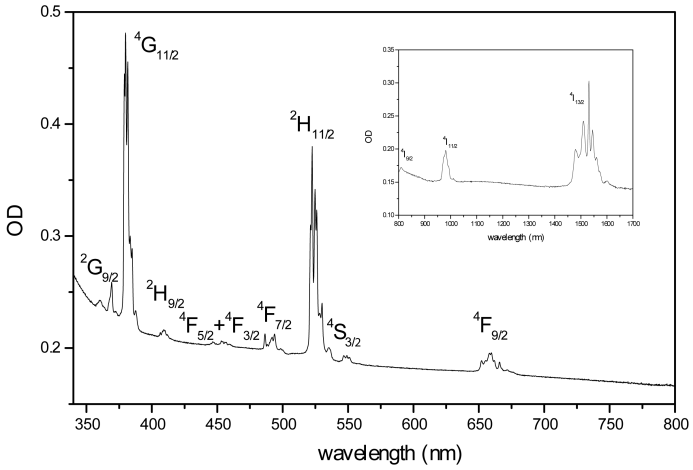

Figure 2.12: Optical Density measured for an erbium doped lithium niobate sample produced by the group of Padova. To each absorption peak the relative transition name is assigned. OD is the absorbance of the material so is defined as $OD = -\log(I_{out}/I_{in})$ where I_{in} and I_{out} are the light intensities measured at the input and the output of the sample.

This particular pumping frequency, 980 nm, is not absorbed by $LiNbO_3$ lattice, which, in general, does not present any absorption at infrared wavelengths, so photorefractivity cannot be excited. As the pump level $^4I_{11/2}$ has a very long lifetime, a saturation for the 1530 nm emission is reached [115, 116]. While this is a drawback for lasing performances, it results to be highly favourable for solitonic waveguide formation. Actually, $Er : LiNbO_3$ presents another level, $^4F_{7/2}$, which is resonant with the pumping transition, so the saturation at $^4I_{11/2}$ strongly increases the probability of having a two step absorption (ESA, Enhanced State Absorption). It provides a fluorescence in the green 550 nm via a radiative spontaneous emission between the levels $^4S_{3/2} \rightarrow {}^4I_{15/2}$.

This emitted fluorescence is absorbed by lithium niobate lattice and

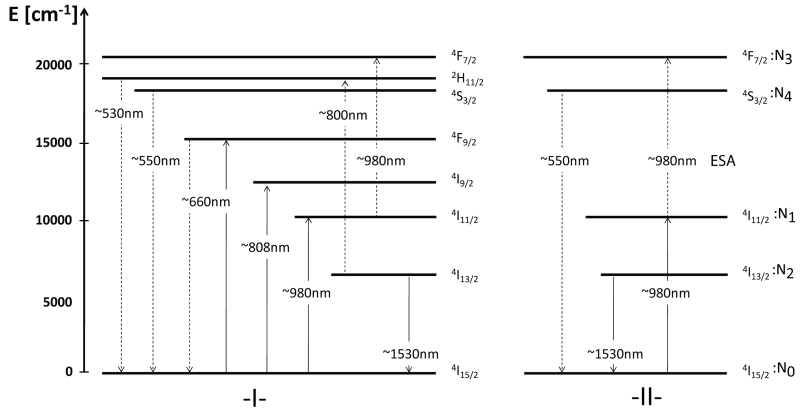

Figure 2.13: -I- Allowed transitions in $Er : LiNbO_3$ and -II- simplified scheme to emphasize the two step absorption at 980 nm producing a fluorescence at 550 nm. N_i represents the population for the i^{th} energetic level.

so photorefractivity can be excited. Consequently, photorefractive self-confinement would be driven by a radiation which is, by definition, incoherent and isotropic. This has been demonstrated here for the very first time and will be discussed in the next section.

2.7 LISS: Luminescence Induced Spatial Soliton

In the past [117,118] incoherent solitons were demonstrated both employing a laser source made partially incoherent by using a light diffusion system, and then directly using a spatially and temporally incoherent white light ($380 - 720$ nm) in an SBN (Strontium Barium Niobate) sample.

As a novelty element, in this section, self-trapping for a coherent infrared beam in lithium niobate will be demonstrated to be possible thanks to a totally self-generated incoherent and isotropic beam [85]. Taking advantage of the enhanced state absorption (ESA) process, allowed by erbium ions energy transitions, a fluorescence at 550 nm can be induced by pumping the material with a 980nm coherent radiation. Lithium niobate is not sensitive to the latter, but the erbium generated fluorescence is directly absorbed by lithium niobate lattice. This gives rise to a photorefractive process,

which would not be possible with an infrared pumping scheme for which this material is transparent.

When the 980 nm beam is focused on the input face of the sample, a luminescence seed is self-generated collinearly to the fundamental beam. Along the propagation path, the fundamental beam continuously excite this fluorescence which is able to promote, photorefractively, charges and thus to induce a space charge field. By applying a bias electric field, the 550 nm self-traps. This result is not at all obvious as the fluorescence propagates isotropically, this means that it radiates with a cylindrical symmetry with reference to the fundamental beam propagation direction. The point is that in spite of this symmetry, its intensity profile is always non-uniform and results well overlapped to the fundamental beam intensity, so it can excite the photorefractive process.

In order to optimize it, propagation inside a waveguide is required. In fact, as it is the luminescence beam to induce the positive refractive index modification, so to guide the light both at 550 nm and also at 980 nm, the higher is the trapping efficiency for the fundamental beam, the higher is the generated luminescence. This in turn maximizes the overall trapping efficiency and stabilization. Furthermore, having the guide a constant section, luminescence efficiency remains constant all along the beam path.

With reference to the experimental setup of fig. 2.6, a second CCD camera is added to image the beam profile along the direction parallel to the beam propagation one. A 980 nm depolarized beam is focused on the input face of the sample. When a bias electric field is applied, in this case $E_{bias} = 40$ kV/cm, the photovoltaic field induced by the green fluorescence is compensated and self-trapping can be achieved. The choice for an erbium concentration value is related only to the necessity of having a high enough luminescence emission. Here measurements for $\rho_{Er} = 0.7$ mol.% ($\simeq 1.32 \cdot 10^{20} \text{atoms} \cdot \text{cm}^{-3}$) are reported, but this does not prevent from having self-trapping for smaller concentrations.

The 980 nm is focused on a waist dimension of (9 ± 0.5 μm) with a power of $P_{980} \simeq 80$ mW and luminescence can be estimated to be in the order of hundreds of μW. This strong luminescence allows to image the transverse trace of 550 nm. In fig. 2.14 is reported the experimental transverse configuration for self-trapping both for the pump (980 nm) beam and the luminescence one (550 nm) considering the initial condition (linear diffraction) and the self-trapped solution. Linear diffraction for the green radiation is evident only for a short propagation length because of its low intensity and

absorption by the lattice.

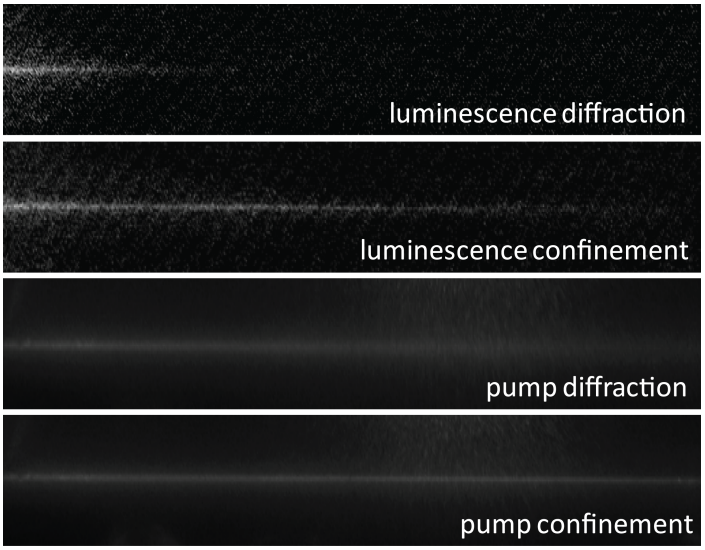

Figure 2.14: Experimental demonstration of self-trapping both for the luminescence and the fundamental beam along the propagation direction. Linear diffraction and self-trapping are depicted for both the wavelengths.

The same self-focusing process as in fig. 2.14, but observed at the output face of the sample and only for the 980 nm is reported in fig. 2.15 -I-. After the application of the bias electric field, the 980 nm starts to self-trap reaching the final dimensions after about 3 hours. As in the usual self-trapping dynamics, also in this case a faster direction (along the $\hat{c}$ axis) exists, fig. 2.15 -II-. Finally, in fig. 2.15 -III-, the beam centre position is analysed with reference to time. This measurement is interesting as it demonstrates that bending influence on the self-trapped beam is extremely reduced and can be quantified as $1 - 2$ μm per hour. This result is again a novelty element in self-trapping process as, usually, self-focusing in lithium niobate is always accompanied by such effect [59].

This improvement can be addressed to the isotropic nature of luminescence. It is known that self-trapping in lithium niobate suffers from bending which has been proved [59] to depend on the too low acceptors concentration. This can be avoided by adding a uniform background illumination to the sample, so to increase the dark conductivity and in turn to avoid

saturation in the illuminated region.

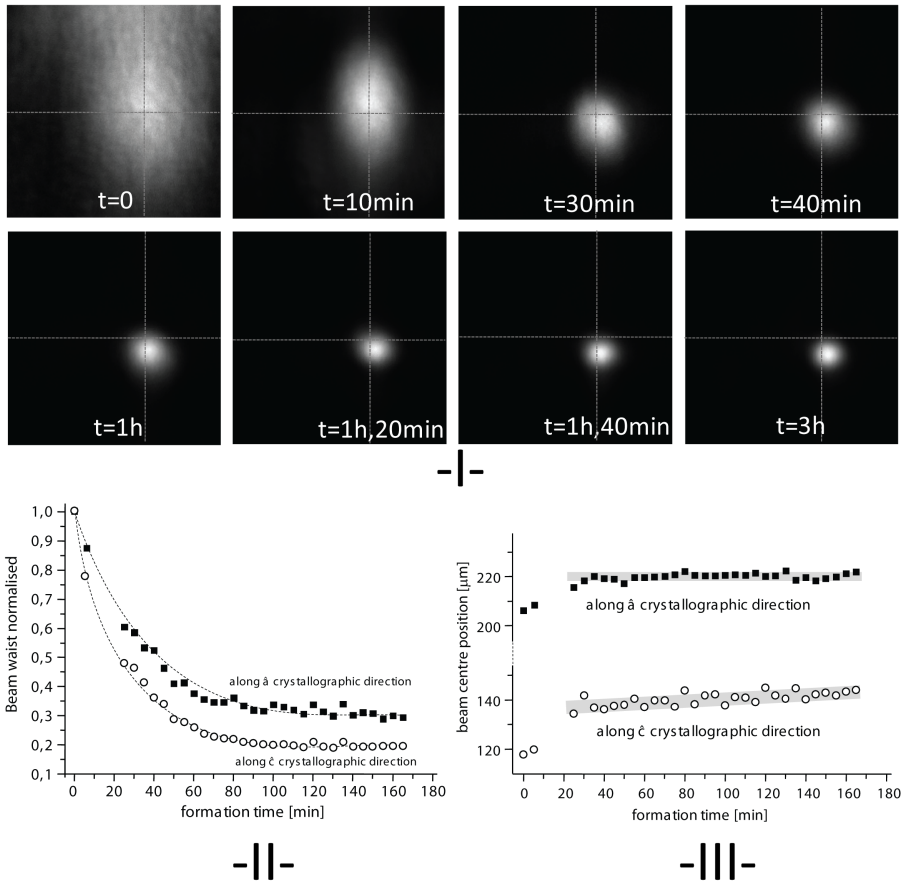

Figure 2.15: -I- Pump beam evolution at the output face of the sample when the bias electric field is applied. -II- beam waist size evolution with time and -III- beam centre position evolution with time.

The induced luminescence, as a consequence of its isotropic propagation, not only induces the photorefractive nonlinearity but realizes also a very efficient self-generated background illumination. In fact, because of its cylindrical symmetry, it is maximized exactly in correspondence to the self-confined beam centre. Its tails are wider than the pump beam ones, so free electrons are always available to avoid photorefractivity saturation

with two main favourable results. Refractive index variation is prevented from distorting into a squared profile that would imply a multimode propagation and bending is expected not to occur. This is exactly what has been experimentally demonstrated.

Uniform sample shining with the application on an other high intensity laser is then no more necessary.

This behaviour has been investigated also numerically and results are in good agreement. In fact, an estimation of the fluorescence interaction with the material, taking into account also the photorefractive charge exchange with the lattice, can be obtained. This will be done by considering both the rate equations for erbium ion transitions, with reference to the simplified scheme of fig. 2.13 -II-, and the Kukhtarev's ones (section 1.3.1) describing the space charge field formation.

Defining F_{980} the photon flux at 980 nm, σ_{ij} the cross sections between levels i and j, τ_i the i^{th} level lifetime and being N_i the population density for the i^{th} energetic level, according to the convention reported in fig. 2.13-II-, rate equations be can written as:

$$\begin{cases} \frac{dN_1}{dt} = F_{980}\left[\sigma_{01}(N_0 - N_1) - \sigma_{13}N_1\right] - \frac{N_1}{\tau_1} \\ \frac{dN_2}{dt} = \frac{N_1}{\tau_1} - \frac{N_2}{\tau_2} \\ \frac{dN_3}{dt} = F_{980}\sigma_{13}N_1 - \frac{N_3}{\tau_3} \\ \frac{dN4}{dt} = \frac{N_3}{\tau_3} - \frac{N_4}{\tau_4} \end{cases} \tag{2.11}$$

Luminescence, produced by the radiative decay from the $^4S_{3/2}$, is absorbed along the propagation distance by the lithium niobate lattice. Photons at 550 nm are absorbed by donors in the lattice (N_D) and electrons are promoted in the conduction band leaving non-compensated N_D^+, according to the equation:

$$\frac{dF_{550}}{dz} = \frac{N_4}{\tau_4} - \sigma^{LN}F_{550}\left(N_D - N_D^+\right)_{LN} \tag{2.12}$$

On the contrary, the photon flux at 980 nm does not interact directly with lithium niobate lattice and its variation along the propagation distance is governed by the relation:

$$\frac{dF_{980}}{dz} = F_{980}\left[\sigma_{01}(N_1 - N_0) + \sigma_{13}N_1\right] \tag{2.13}$$

As already mentioned, it is the isotropically generated green to induce the refractive index variation that also the fundamental beam will use to propagate undiffracted. The refractive index contrast, and so the induced space charge field, can be obtained from the Kukhtarev's equations (keeping the same meaning for the involved parameters as in section 1.3.1) according to:

$$\begin{cases} \frac{\partial N_D^+}{\partial t} = (\beta + \sigma^{LN} F_{550})(N_D - N_D^+) - \xi n_e N_D^+ \\ \rho = e(N_D^+ - N_A - n_e) \\ \vec{\nabla} \cdot \vec{D} = \rho \\ \frac{\partial \rho}{\partial t} + \vec{\nabla} \cdot \vec{J} = 0 \\ \vec{J} = e\mu n_e \vec{E} + \mu K_B T \vec{\nabla} n_e + \beta_{PV}(N_D - N_D^+) F_{550} \hat{c} \end{cases} \tag{2.14}$$

All these equations, together with the wave equations for the two wavelengths, eq. 2.15, can be solved numerically obtaining the propagation behaviour for both the beams, as in fig. 2.16. Numerical values for transitions in erbium doped lithium niobate are taken from [119]

$$\frac{\partial A_{980/550}(x,z)}{\partial z} = i \left[\frac{1}{2k} \frac{\partial^2}{\partial x^2} + \frac{2\pi}{\lambda \Delta n} \right] A_{980/550}(x,z) \tag{2.15}$$

Figure 2.16: Numerical simulation: self-trapping induced by the luminescence beam at 550 nm on the fundamental one at 980 nm.

2.8 Towards laser devices in solitonic waveguides

Self-trapping at 980 nm via the fluorescence emitted at 550 nm (LISS) opens the way to realize a lasing device in the third window for telecommunications ($\simeq$ 1530 nm). In this case, the fundamental beam allows to obtain, at the same time, both the solitonic waveguide and the optical pumping for erbium ions to provide an optical gain for the emitted 1530 nm radiation, thanks to the radiative transition $^4I_{13/2} \rightarrow {}^4I_{15/2}$.

In this section only the very basic technological problems related to the lasing process inside a solitonic waveguide will be discussed. Up to now, in fact, lasing threshold was not overpassed because of the not-enough optical 980nm pumping power. This problem is consequence of the very narrow absorption line of erbium ions in comparison to the much wider pumping source emitted line. So, only a fraction of the injected power at 980nm can actually be absorbed by the active ions.

With respect to the state of the art for laser emission from an integrated waveguide [79–84], the work performed during this thesis presents at least two major improvements: integrated waveguides written in the bulk (LISS), and not only close to the surface, and an overall improvement of all the lasing related figures of merit by pumping the material at 980 nm instead of 1480 nm. For the latter in fact, emission and absorption cross section spectra are almost completely overlapped so limiting the overall net optical gain that can be achieved. Although this strong limitation, this pumping scheme offers the advantage of granting a very good mode matching.

Luminescence in green allows to make the beam self-trap, but it provides also a very high stabilization during the formation process. As demonstrated in the previous section, luminescence not only writes the waveguide for the pumping radiation (980nm), but acts also as a local and in turn extremely effective background radiation that prevents bending to occur. If the active waveguide is placed into a cavity and if a bending was present, then the light re-injected into the material by the coupling mirror would of course present spatial k-vectors very different from those matching the waveguide acceptance angle. Actually, because of the low refractive index contrast that spatial solitons can induce ($\delta n \simeq 10^{-4}$), the more divergent k-vectors cannot be coupled. Consequently, in a bending-free configuration, the extremely low propagation losses, characteristic of a solitonic waveguide, are thus accompanied by low coupling losses at the sample interfaces as well. This is a key parameter to make such a guiding structure lase.

The achievement of a lasing action requires an amplification of such 1530 nm luminescence via the realization of a resonating cavity in which the active waveguide must be inserted. At the moment two cavity configurations have been considered: Fabry-Perot and hemispherical, fig. 2.17. The first one did not give any useful result because of the impossibility of getting samples with plane parallel faces, consequently the hemispherical one has been realized.

The Fabry-Perot geometry, fig. 2.17a, is quite simple as it was composed by two plane mirrors directly placed on the sample. Mirrors were chosen to provide very high reflectivity (ideally 100% and 98%) for the 1530 nm and very high transmission for all the other employed wavelengths. In this way, luminescence at 1530nm can be amplified up to the lasing threshold exceeding. Practically this configuration is not usable as, for definition, it works in the the stability region boundaries. In fact, considering the notation based on the g parameters, being $g = 1 - L/R$, L the cavity length and R the mirror curvature radius, for a Fabry-Perot configuration $g_{1,2} = 1$. This implies that the overall performances of this structure are sensitive to every kind of external or internal influence that can make it stop working. Not parallel faces take the working point completely out of the stability region.

On the contrary, the hemispherical configuration, fig.2.17b, results to be much more stable as the g parameters can be tuned in order to make it work inside the stability region $g_1 = 1$ and $0 < g_2 \leq 1$ for a cavity length (L) shorter than, or equal to, the curved mirror radius (R). This geometry is the one employed to investigate lasing from the solitonic waveguide.

As anticipated, the main issue for obtaining lasing action is given by the actual pump power that can excite erbium response. To exceed or at least to minimize this limitation, the waveguide transverse dimension assumes a critical importance as by reducing it, photon flux can be increased. Up today, efficient self-confinement has been demonstrated in lithium niobate for beam waists in the order of $7 - 8$ μm at the sample input face [9, 101]. Consequently, the maximum allowed photon flux value cannot be radically changed. By using the equation set described in the previous section, eq. 2.11, a qualitative behaviour for the population inversion between levels $^4I_{13/2}$ and $^4I_{15/2}$ in the steady state regime has been investigated in function of the input beam waist and the input pump power at 980 nm. They are depicted in fig. 2.18b. From this analysis, it can be deduced that moving from an input waist of 5 μm to a 10 μm one, the necessary input power must be increased from $\simeq 11$ mW to $\simeq 45$ mW. This is the actual power

that erbium ions must absorb to produce population inversion.

The two cavities have been tested by injecting into the samples a 80 mW unpolarized 980 nm laser. Also for this power value and for an input waist of 8 μm, population inversion and in general all the involved energetic level population evolutions, fig. 2.13 -II-, have been simulated in the transient regime, fig. 2.18a. Population inversion between $^4I_{13/2}$ and $^4I_{15/2}$ can be reached, but an other important aspect must be discussed. Luminescence in green is originated by the saturation (long lifetime) of the $4I_{11/2}$ level, so actually the gain at 1530 nm is limited by this bottleneck [116]. Observing the behaviour of its population evolution, it appears that as soon as population inversion is reached, the fluorescence amount should decrease and in turn increase the emission for lasing action. This reduction (and not annihilation) is another favourable aspect as this residual luminescence can continue stabilizing the process by opposing to all those factor, like temperature, which could break the solitonic waveguide and so prevent laser action occurring.

Until now, doping concentration has not yet been discussed because in absence of experimental evidence it is not possible to estimate the actual performances. It is expected that the higher is erbium doping in the melt, the higher should be the emitted fluorescence and so the optical gain. This is a critical aspect as by increasing its concentration also the probability of having erbium cluster formation increases. In this case erbium ions would start exchanging energy between them so reducing the overall performances, in other words losses would be increased. So clearly, the proper concentration value is the one that realize the best compromise gain - losses.

Another critical point consequence of the introduction of very high dopant quantities is related to the crystal growth. The presence of scattering centres (non-uniform samples) would again increase losses and prevent the device from lasing.

These measurements will be started again as soon as the new pumping high power laser will be available.

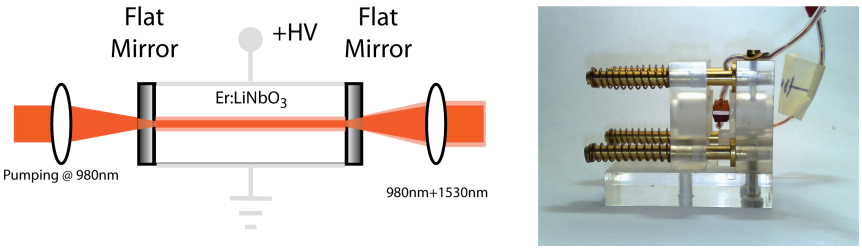

(a) Fabry-Perot resonator designed for 1530 nm with parallel flat external mirrors put in contact with sample surfaces. The principle working scheme and the experimental realization are reported on the left and on the right respectively.

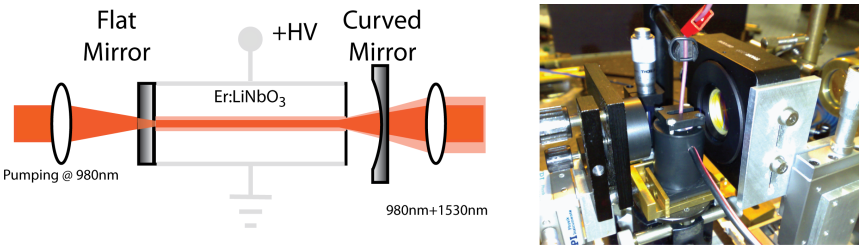

(b) Hemispherical resonator designed for 1530 nm with a parallel mirror put in contact with the input sample surface for the pumping radiation and an external curved mirror placed at a distance L less than its curvature radius (R). The principle working scheme and the experimental realization are reported on the left and on the right respectively.

Figure 2.17: Resonator experimental configurations having $Er : LiNbO_3$ as active medium. Waveguide realization is based on the LISS physical principle.

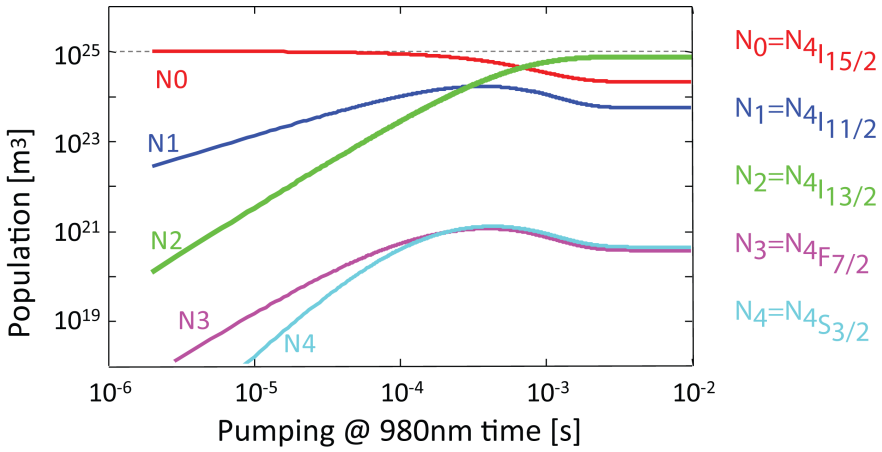

(a) Population evolutions in the transient regime for a pumping power of 80 mW at 980 nm. Population inversion between levels $^4I_{13/2}$ and $^4I_{15/2}$ can be reached and in correspondence a luminescence emission decreasing appears.

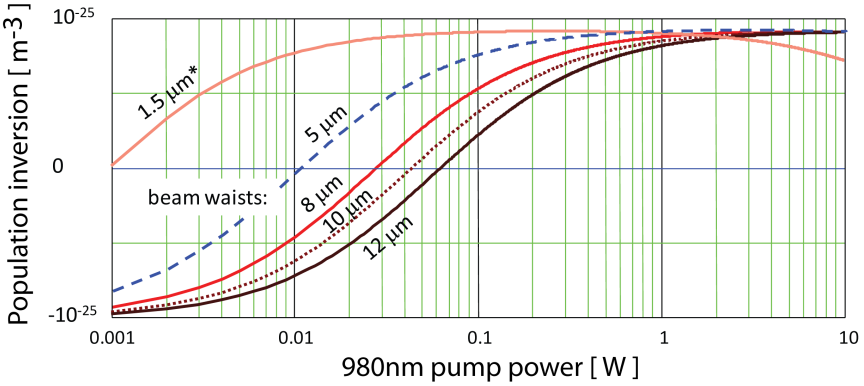

(b) Population inversion at steady state between levels $^4I_{13/2}$ and $^4I_{15/2}$. It is parametrized to the beam waist dimension and to the pump power at 980 nm.

Figure 2.18: Numerical simulations about population evolutions in the transient regime for all the involved energetic levels, fig. 2.18a and population inversion for lasing at 1530 nm in the steady state, fig. 2.18b.

Chapter 3

Second Harmonic Generation and solitonic waveguides

3.1 Introduction

During the last years, integrated source technology required research activity to move towards the realization of devices working in the blue region and in general to short wavelengths so, for example, to accomplish the necessity of storing the always increasing amount of data in smaller optical media. Different approaches were proposed in the past, for example sources based on GaAs or GaN [120–122] compounds. These materials suffer from the necessity of being grown on a substrate in order to provide a surface second harmonic generation, so also their realization is expensive and technologically complex.

A valid alternative which is taking place in the market (see for example Crystal Technology [123]) is provided by periodically poled structures in lithium niobate substrates (PPLN) [124–126]. Materials with a high phase mismatch (lithium niobate) generate the second harmonic signal with a periodical trend (the period is called coherence length and typically is in the order of microns), but the maximum conversion efficiency is low. The periodical ferroelectric inversion (with period equal to a coherence length) allows to increase the efficiency as an always increasing trend for the generated signal can be achieved. In this way, the low conversion efficiency can be strongly enhanced. This technique is known as Quasi Phase Matching (QPM) [127]. The price to pay to achieve such conversion increasing is the necessity of re-

alizing an accurate domain inversion. This can be done only applying high values for the electrical field so to overpass the coercitive one, characteristic of the material. This field decreases with the increasing of lithium concentration in the melt [38, 128]. Furthermore, as the inversion must take place every few microns (according to the wavelength to be duplicated), then also in this case the process results to be expensive and critical. Another drawback of this solution is consequence of the photorefractive nature of lithium niobate. Actually, performances are strongly affected by the space charge field induced by the light itself as photorefractive efficiency results maximized quite for green and blue conversion in this material. To avoid this kind of problems, the lattice must be doped with transition metals which prevent space charge field from building up, typical employed materials are Zinc and Magnesium [123, 129].

As novelty element, here is proposed second harmonic generation inside waveguides written in the bulk of an undoped, congruent, ferroelectric monodomain, lithium niobate via the photorefractive effect. This approach goes in the opposite direction of what proposed with PPLN where photorefractivity is an effect that must be eliminated.

Lithium niobate does not support second harmonic generation from 800 nm to 400 nm as a consequence of the very high phase mismatch, so conversion efficiency is typically very low. Taking advantage of the propagation inside a waveguide, it would be possible to increase it [130, 131].

A waveguide actually preserves the transverse dimension of the propagated mode. So, being conversion efficiency proportional to the inverse of this transverse dimension, efficiency can be kept constant. Furthermore, the smaller is the waveguide transverse section, the higher is the fundamental beam intensity and consequently also conversion efficiency can be improved. Also the phase matching condition remains unchanged all along the propagation distance, so again conversion efficiency can be maintained constant.

Actually, the idea of realizing a parametric conversion inside a waveguide is not new, as already demonstrated to be effective inside PPLN. In [132] a Zn-diffused waveguide is used to produce an optimized second harmonic signal at 397.8nm.

In this work, I introduce the second harmonic generation inside a solitonic waveguide written in the volume of lithium niobate. It will be shown that second harmonic generation (based on the birefringence of the material) can be achieved taking advantage of the higher nonlinear coefficient for lithium niobate: d_{33}. Such a result can be obtained with an $ee - e$ interac-

tion (fundamental and second harmonic beams are extraordinary polarized) and that a strong signal is obtained in spite of the very high phase mismatch. It will be demonstrated also that it is the upconverted frequency to write the solitonic waveguide inside which it will propagate together with the fundamental one. This result is consequence of an interplay between the quadratic and photorefractive effects.

The physical relations between the fundamental and the generated second harmonic beam will be analysed demonstrating that the second harmonic seed is actually composed by two contributions with peculiar properties in terms of phase and group velocities with respect to the fundamental one.

3.2 Second harmonic generation: An introduction

Second harmonic generation [133–135] is a second order nonlinear optical effect, as pointed out in equation 1.1, and it consists in the conversion of two photons (o- or e- polarized) at the fundamental frequency ω into one single photon (o- or e- polarized) at 2ω via an intermediate virtual energetic level. So an ee-e interaction means that two e-polarized photons at ω generate one photon again e-polarized at 2ω.

Considering two plane waves which propagate along the z axis and oscillate at frequencies ω and 2ω respectively, if their associated electric fields are written as:

$$\begin{cases} E_i^{(\omega)}(z) = 1/2\left[E_i^{(\omega)} e^{i(\omega t - k^{(\omega)} z)} + cc\right] \\ E_j^{(2\omega)}(z) = 1/2\left[E_j^{(2\omega)} e^{i((2\omega) t - k^{(2\omega)} z)} + cc\right] \end{cases} \tag{3.1}$$

then their interaction can be described by the coupled equations:

$$\begin{cases} \frac{dE_i^{(\omega)}(z)}{dz} = -i\omega\sqrt{\frac{\mu_0}{\epsilon^{(\omega)}}} d_{eff} E_j^{2\omega} E_k^{\omega *} e^{-i\Delta k z} \\ \frac{dE_j^{(2\omega)}(z)}{dz} = -i2\omega\sqrt{\frac{\mu_0}{\epsilon^{(2\omega)}}} d_{eff} E_i^{\omega} E_k^{\omega} e^{i\Delta k z} \end{cases} \tag{3.2}$$

where d_{eff} is the nonlinear coefficient, and it is related to the crystallographic structure of the sample and i,j,k represent the beam polarization directions which can be both extraordinary or ordinary. These two equations keep into account also the case of fundamental beam depletion along with propagation. Actually, in the measurements that will be further on described, depletion

will be considered negligible because of the low conversion efficiency. In this case $dE_i^{(\omega)}/dz = 0$ and in turn the SHG process can be described only by the second equation in 3.2.

$\Delta k = 2k_1 - k_2$ represents the phase mismatch for the two frequencies propagating inside the anisotropic material and its value influences conversion efficiency, defined as the ratio $\frac{P^{(2\omega)}}{P^{(\omega)}} \propto L^2 \frac{sin(0.5\Delta kL)^2}{(0.5\Delta kL)^2}$ for a sample length of L. It is worth remembering that conversion efficiency also directly depends on the injected fundamental beam light intensity. Only for a $\Delta k = 0$ that is to say $2k^{\omega} = k^{2\omega}$ or $n^{2\omega} = n^{\omega}$, conversion is maximized. This condition can be fulfilled by considering different polarisations for the fundamental and second harmonic beams. For values of $\Delta k \neq 0$, the conversion efficiency has an oscillatory behaviour and the distance between two adjacent peaks is called coherence length (l_c), and is related to Δk as:

$$l_c = \frac{2\pi}{\Delta k} = \frac{\lambda}{2(n^{2\omega} - n^{\omega})} \tag{3.3}$$

This is actually the situation of lithium niobate. As the aim of this research activity is to realize an integrated source emitting in the blue spectral region, a 800 nm - 400 nm conversion is required. Lithium niobate does not support it and phase mismatch is quantified to be in the order of $10^{+4} cm^{-1}$, independently from the interaction type. Conversion efficiency is very low and also coherence length results to be much shorter than the pulse spatial length. As a consequence, the second harmonic contribution is expected to be characterized by a sequence of oscillations.

The nonlinear polarization at 2ω is related to the electric field associated to each interacting photon, so at ω, by the expression:

$$P_{NL_i}(2\omega; \omega, \omega) = 2\epsilon_0 d_{ijk} E_j(\omega) E_k(\omega) \tag{3.4}$$

According to the contracted notation and with the choice $1 \rightarrow x$ $2 \rightarrow y$ $3 \rightarrow z$, the expression for the nonlinear polarisation eq. 3.5, specialized for the case of lithium niobate (3m group), is:

$$\begin{bmatrix} jk: & 11 & 22 & 33 & 23,32 & 31,13 & 12,21 \\ l: & 1 & 2 & 3 & 4 & 5 & 6 \end{bmatrix}$$

$$\begin{bmatrix} P_x(2\omega) \\ P_y(2\omega) \\ P_z(2\omega) \end{bmatrix} = \begin{bmatrix} 0 & 0 & 0 & 0 & d_{31} & -d_{22} \\ -d_{22} & d_{22} & 0 & -d_{31} & 0 & 0 \\ d_{31} & d_{31} & d_{33} & 0 & 0 & 0 \end{bmatrix} \begin{bmatrix} E_x(\omega)^2 \\ E_y(\omega)^2 \\ E_z(\omega)^2 \\ 2E_y(\omega)E_z(\omega)^2 \\ 2E_x(\omega)E_z(\omega)^2 \\ 2E_x(\omega)E_y(\omega)^2 \end{bmatrix} \quad (3.5)$$

The values reported in literature for the coefficients (@1.064μm [69]) are $d_{31} = -5$pm/V, $d_{22} = 3$pm/V and $d_{33} = 33$pm/V and they can change in function of the material stoichiometry.

To maximize conversion efficiency, a type 0 ($ee - e$) interaction will be demonstrated to occur.

In the next sections phenomena related to a type-0 polarization mixing, ($ee - e$), for a laser beam propagating perpendicularly to the optical, $\hat{c}$, axis of the material, are reported. With this configuration, non-critical interactions are performed and spatial walk-off is prevented from occurring. The specialized expression for the nonlinear polarization and for this interaction type, is reported in eq. 3.6. It is the same for a beam propagating along the x or y axis:

$$P_{NL_z}(2\omega) = 2\epsilon_0 d_{33} E_z(\omega)^2 \quad (3.6)$$

Being the conversion efficiency for the second harmonic signal at 400 nm very low, a very high intensity for the fundamental beam is required. To accomplish this, femtosecond pulses are focused onto the input face of an undoped lithium niobate sample.

3.3 Second harmonic beam properties in photorefractive congruent lithium niobate

Before analysing the effects of the second harmonic generated contribution to the self-trapping process and in turn for the solitonic waveguide formation, the physical properties existing between this second harmonic pulse (SH) and the fundamental one (FF) will be discussed.

As anticipated, because of the high phase mismatch, the coherence length of the second harmonic generated pulses is expected to be shorter than

the spatial extension of the fundamental pulse. With reference to a type-0 (ee − e) interaction, when pulses at 800 nm are injected into the sample with a time duration of 65 fs, so with a spatial extension of about 9 μm, then a second harmonic pulse at 400 nm is generated with a coherence length of about 2.5 μm. As the two wavelengths feel different refractive indices, SH and FF propagate with different velocities and finally separate. Calculating the non stationary length value: $L_{nst} = \tau/(\mathrm{u}_{\mathrm{SH}}^{-1} - \mathrm{u}_{\mathrm{FH}}^{-1})$, being τ the pulse duration and u the speed of pulses [136, 137], the two pulses should be completely separated after about $125\mu m$; this value is obtained for the case of transform limited pulses. This condition is verified for the employed laser with reference to a hyperbolic secant beam profile that is provided by a Kerr lens modelocking realized inside the main oscillator. As a consequence of the very high phase mismatch and the extremely low fundamental pulse duration, the separation of these two pulses is indeed observable.

It will be shown that the FF and the SH pulses do not simply propagate with a speed forced by the dispersion law in lithium niobate and moreover that not only one SH pulse is generated but two. Actually, when one fundamental beam pulse enters the bulk, it generates two second harmonic pulses. One of them results locked with the fundamental, both in phase and group velocity. They propagate according to the refractive index experienced by the fundamental beam. The second one instead, propagates according to its own dispersion law and independently from the locked two. This aspect had been theoretically predicted by Bloembergen [138] who demonstrated that in presence of a nonlinear interface a laser pulse gives rise to harmonics. In details, by introducing the nonlinear properties of the medium into the Maxwell's equations, in terms of the susceptibility tensor, they could identify a solution for the homogeneous and the inhomogeneous equations. The inhomogeneous solution showed that along with the transmitted fundamental beam, a second harmonic component propagates and that it is characterized by a $\vec{k}$ vector identical to the one of the fundamental: $\vec{k}^{(\omega)}$. On the contrary, the pulse related to the homogeneous solution, is characterized by a different direction $\vec{k}^{(2\omega)}$. These two pulses result to be parallel only in the limit of perfectly phase-matched configuration or in correspondence to a perpendicular incident plane. In addition to the transmitted beams, an interface reflected SH beam is created. Further theoretical and numerical investigations in the femtosecond regime and in the hypothesis of phase mismatched conditions [139], demonstrated that the fundamental and the second harmonic pulse propagating with the same spatial $\vec{k}^{(\omega)}$ are

locked together. Both propagate experiencing the dispersion properties of the pump beam and the same group velocity. Numerical analysis about the propagation of the two transmitted second harmonic pulses in a dispersive medium characterized by high phase velocity mismatch (so group velocity mismatch) have been performed by authors. They showed that during the propagation, and as long as they are superimposed, they interfere giving rise to Maker-Terhune fringes [140, 141]. These fringes present again the oscillatory behaviour that was initially explained in terms of short coherence length.

Some other authors [142,143] derive the same pulse split structures without considering the presence of a nonlinear interface. They suggest that for very short pulse durations, like in the femtosecond case, and in case of propagation inside a medium characterized by a high group velocity mismatch (GVM), a group velocity dispersion (GVD) can be induced and that is not negligible. Its effect consists in broadening both the fundamental and the second harmonic pulses. The shape of the pulse changes and the converted energy will decrease more and more influencing the conversion efficiency. Taking into account the contemporary action of the nonlinearity and the dispersion law of the material acting on the oscillating second harmonic pulse, splitting of the second harmonic pulses can be explained.

Type-0 parametric interaction in $LiNbO_3$ is characterized by a phase and group velocity mismatch, and for a conversion 800nm to 400nm the phase mismatch is very high, of the order of $\Delta k \simeq 2.4 \cdot 10^4 cm^{-1}$. In the framework of a collaboration between the Department of Energetics and the Redstone Arsenal (Alabama), starting from a numerical model initially developed for short pulse propagation inside negative index materials [144], numerical investigations about the propagation of femtosecond pulses inside $LiNbO_3$ were performed. These simulations take into account the parameters provided by the sample supplier and extraordinarily polarized pulses having duration of $\tau_p = 100fs$ and peak intensity of $I_{peak} = 1GW/cm^2$. A $200\mu m$ propagation distance before the nonlinear interface is considered and, after it, they propagate for $300\mu m$, which is long enough to observe pulse separation, thanks to the high group velocity mismatch.

As reported in fig. 3.1, when a femtosecond pulse is launched through the nonlinear interface, part of it is back reflected, interfering with itself. The rest is transmitted creating a second harmonic contribution fig. 3.1(a). The two contributions are represented with different scales as a consequence of the low conversion efficiency. As the propagation distance increases, the sec-

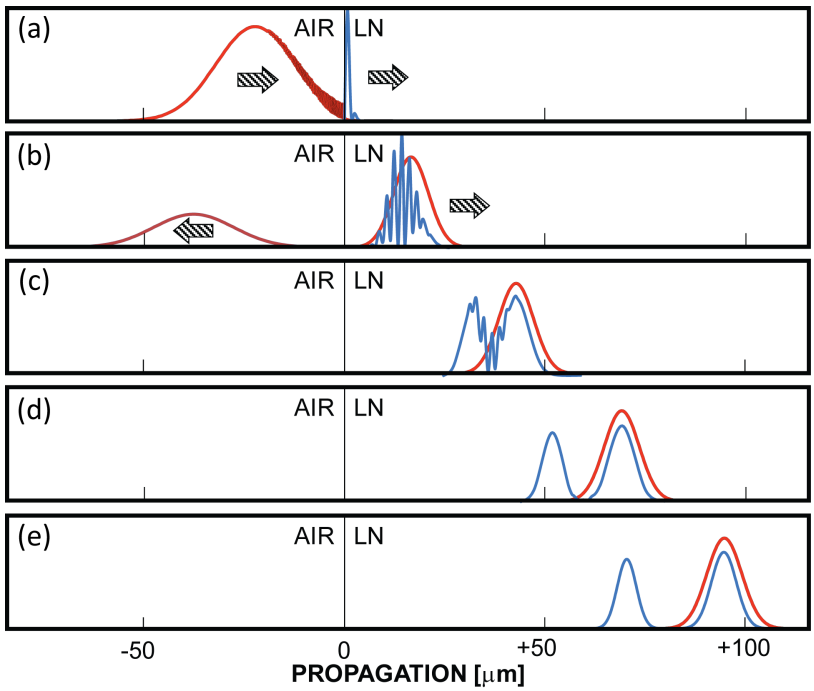

Figure 3.1: (a) The fundamental beam (red) is launched against a nonlinear interface and a second harmonic contribution (blue) is generated. A part is transmitted and a part is back reflected (b). The transmitted component is composed by two contributions: one locked with the foundamental, same $\tilde{k}^{(\omega)}$ and the other completely non related to it, with its own $\tilde{k}^{(2\omega)}$. Initially they interfere (b) and after a long enough propagation distance, they completely separate thanks to their very high GVM (c)-(e).

ond harmonic signal looks to have a behaviour typical of phase mismatched configuration: a very short coherence length is present giving rise to fast oscillations inside the propagating pulse, fig. 3.1(b). Such oscillations are the beating of two pulses. In fact, for long enough propagation distances, such second harmonic splits, one remaining locked under the fundamental pulse, and one keeping its nature of usual second harmonic fig. 3.1 (c)-(e). The locked one will thus propagate with the same speed of the fundamental pulse while the other will behave according to the material dispersion.

3.4 Experimental demonstration of pulse locking: phase and group velocities

Under the hypothesis of type-0 (ee − e) interaction, it will be experimentally demonstrated that two SH pulses are generated. In agreement with the theoretical predictions, one of them, what is reported to be the solution of the inhomogeneous equation, results to be locked to the transmitted fundamental one both in terms of phase and group velocity [145]. If a SH pulse is phase locked with the fundamental one, then it will experience exactly its refractive index in the medium: n_e(800nm). In turn, they will propagate with the same speed, while the other should propagate experiencing the refractive index n_e(400nm) and slower than the others. To succeed in distinguishing the directions for all the involved wavelengths, one side of the sample has been cut with an angle of 20° with respect to the normal incidence of the fundamental beam. So it behaves like a prism and, in correspondence to its output face, where the prism is realised, the directions for the beams will be different according to the felt refractive index, in agreement with the Snell-Cartesio law. In fig. 3.2a the employed setup is reported. The fundamental beam is focused in correspondence to the input face of the sample, is orthogonally injected, and a CCD camera is used to distinguish the positions for the three wavelengths: ω, locked 2ω and free 2ω.

Using this geometrical configuration and changing the injected light polarization, pulse splitting has been verified for the various allowed interactions types by imaging the sample cut face on the CCD sensor. The different light component positions can be distinguished by using a proper filtering system to cut one of the two colours.

When an extraordinary polarized beam at the 800nm is injected into the sample, two 400nm pulses can be distinguished: one which is superimposed to the fundamental beam, and another which occupies a different position with respect to the Snell-Cartesio law, fig. 3.2b -I-. By the application of a polarizer, both the pulses result to be extraordinarily polarized, so a type-0 ee − e interaction is realised for a calculated phase mismatch of $\Delta k \simeq 2.4 \cdot 10^4 cm^{-1}$.

From this observation, both the hypothesis have been demonstrated: two second harmonic pulses are generated and one of the two is phase-locked with the fundamental one.

If an ordinarily polarized fundamental beam is now injected fig. 3.2b -II-,

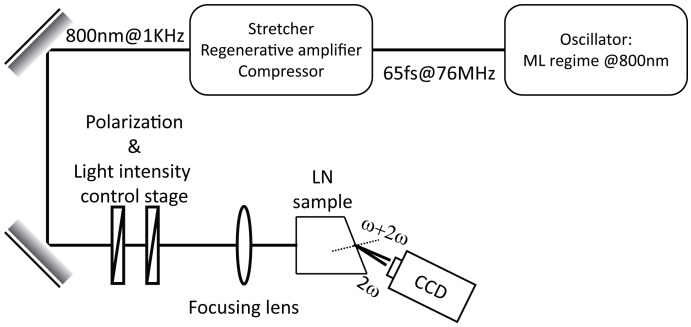

(a) Experimental setup used to identify all the allowed conversion types and phase velocity locking for the locked pulses in $LiNbO_3$.

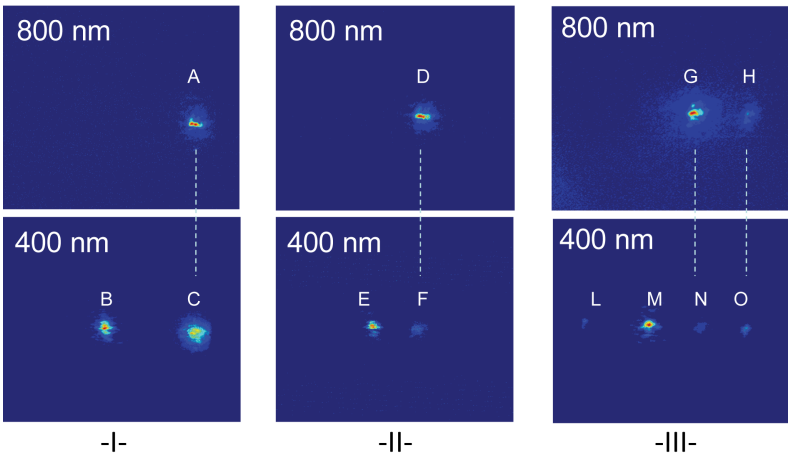

(b) Possible second harmonic conversion types in $LiNbO_3$ exploited thanks to the prismatic sample configuration. (-I-) type 0 $(ee-e)$, (-II-) type-I $(oo-e)$ and (-III-) type 0, type-I and type-II $(oe-o)$ and $(oe-e)$ couplings.

Figure 3.2: Second harmonic interaction types in $LiNbO_3$: (a) Experimental setup and (b) generated contributions recorded at the output face of the sample in function of the injected polarization.

on the camera a phase locked extraordinarily polarized 400nm results superimposed to the ordinarily polarized 800nm . The non-locked 400nm pulse results to be extraordinarily polarized as well. So a type-I $(oo-e)$ interaction is achieved and the corresponding phase mismatch is calculated to be

about $\Delta k \simeq 1.2 \cdot 10^4 cm^{-1}$.

Finally, injecting both the polarizations, fig. 3.2b -III-, extraordinary (G) and ordinary (H), then type 0, type-I and type-II generations can be simultaneously obtained. As previously discussed, an extraordinarily polarized fundamental beam will create two extraordinarily polarised second harmonic pulses (M, O)according to a type 0 coupling process. An o-polarized input fundamental beam will produce two e-polarized SH pulses in positions M and N, according to the type-I interaction. The contribution in L is the result of a type-II coupling process and is o-polarised. The phase mismatch in this case is calculated to be $\Delta k \simeq 1.8 \cdot 10^4 cm^{-1}$ for an oe-o interaction and $\Delta k \simeq 3.5 \cdot 10^4 cm^{-1}$ for an oe-e process. In this case, generation efficiency for the contribution in L is very low. In fact, as a consequence of the very high group velocity mismatch which force the cross-polarized pump pulses to quickly separate, the second harmonic pulse cannot lock with the fundamental one. The spot in L represents the solution for the homogeneous equation.

To demonstrate that also group velocities for the two locked pulses are the same, setup has been modified as in fig. 3.3a. Being the type-0 interaction the most efficient, pulse group velocity locking has been investigated in this configuration.

The two superimposed phase-locked pulses, 800nm and 400nm , coming out the tilted face of the sample, are focused by a curved mirror on the input face of a BBO crystal. This sample is cut in order to grant the $\omega + 2\omega = 3\omega$ interaction and so to have all the three frequencies at its output face. The 3ω can be obtained only if the ω and 2ω pulses arrive exactly at the same time on the sample. If the photodiode can reveal a 3ω signal then also the group velocity locking is demonstrated.

Injected pulses have been measured to have a duration in the order of 110fs and an energy of few tens of micro-joule. Beam waist at the input of lithium niobate sample is about 600μm and intensity in the order of the GW/cm^2. In the setup, several optical stops have been added in order to cut, as much as possible, all the scattering and contributions from the involved wavelengths but the ultraviolet one. In front of the photodiode are put interferential filters that only allow the transmission of the 3ω component.

In fig. 3.3b -I- is reported the pulse train at 3ω after having injected the fundamental beam onto the input face of lithium niobate. The problem associated to this kind of measurement is that also lithium niobate could produce a third harmonic contribution if a high enough light intensity was

injected in the sample.

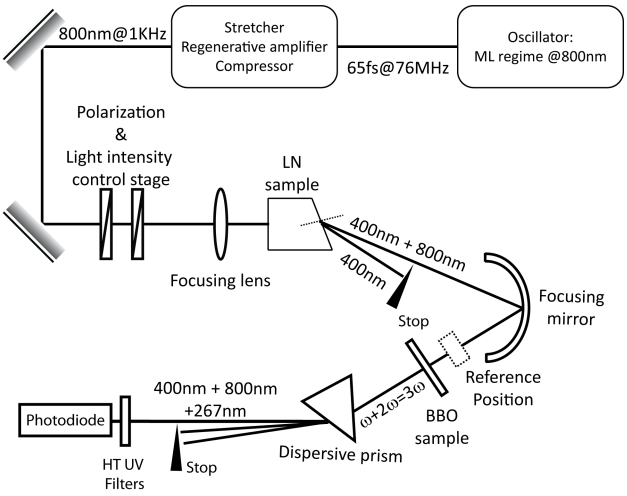

(a) Experimental setup built to investigate the group velocity locking. The tilted output face of the sample, working as a prism, allows to focus only the two locked pulses on a BBO sample. This, in turn, will produce a 3ω only if the two components at ω and 2ω arrive at the same time on it.

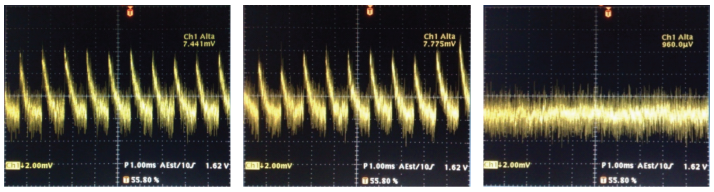

-I- -II- -III-

(b) Group velocity locking verification. -I- Pulse train at 3ω obtained by focusing the locked ω and 2ω on the BBO sample. -II- Same configuration but cutting every eventual 3ω contribution from $LiNbO_3$ by placing a thin glass plate in the reference position, fig. 3.3a. -III- Signal obtained when ω and 2ω are separated in time by using a thick glass plate in the reference position so preventing BBO from producing any 3ω.

Figure 3.3: (a) Experimental setup to exploit the group velocity locking for the ω and 2ω pulses and (b) group velocity locking evidence signal from the photodiode.

To be sure that the contribution shown by the photodiode is consequence of a generation inside the BBO sample, a 100μm thin glass, is put in between the $LiNbO_3$ and BBO, in the reference position reported in the setup sketch. If it was lithium niobate to produce the ultraviolet contribution, the glass would completely absorb it and no pulse train at 3ω should be visible. This is not the case, fig. 3.3b -II-, as the pulse train is still present. Finally, the temporal superposition of the fundamental and second harmonic pulses arriving on the BBO sample has been tested. By putting a thick glass plate at the place of the thin one, thanks to the dispersive properties of the material, we separate in time the FF and SH pulses and this implies that they cannot arrive at the same instant on the BBO sample. In this case, it is expected not to have the third harmonic generation from BBO. Actually, as in fig. 3.3b -III-, no pulses train can be revealed.

In conclusion it is possible to assess that even in condition of very large phase mismatch, the second harmonic pulse, the one foreseen by Bloembergen as solution of the inhomogeneous equation, is phase-locked and has the same group velocity of the fundamental beam.

3.5 Experimental self-trapped (solitonic) waveguide at 800nm in congruent lithium niobate

Having demonstrated that second harmonic generation at 400nm can be obtained with a type-0 ($ee - e$) interaction type, and taking advantage of the highest nonlinear coefficient d_{33}, it will now be demonstrated that self-trapping can be obtained and that the upconverted light is responsible for self-trapping.

As photorefractive self-trapping realize a waveguide [9] inside the material, it can be used to make second-harmonic and fundamental beam propagate inside it in diffractionless conditions. In this way, the blue radiation generates the guide which freezes its k-vector configuration all along the propagation distance. This, in turn, increases the conversion efficiency by fixing the phase-matching configuration. Because of this, it is expected that this feedback can realize a self-written and self-optimized blue light radiation coherent source.

To verify such behaviour [146], the setup in fig.3.4 has been employed. In details, the 800nm beam, linearly polarized along the $\hat{c}$ axis of an undoped congruent $LiNbO_3$ sample, is focused on its input face. This wavelength

is provided by a Ti : Sapphire oscillator which can work both in continuous wave (CW) or modelocked (ML) regime. By applying an external static electric field (E_{bias}) along the $\hat{c}$ axis direction, the evolution of self-trapping is monitored by imaging the output face of the sample on a CCD camera. A sample background uniform illumination has been added in order to stabilize the self-trapping process and in turn reduce the bending of the written waveguide. The sample, commercial from Crystal Technology, has a lithium concentration $c_{Li} = 48.38\%$ and an optical absorption $\alpha(@1064nm) < 1.5 \cdot 10^{-3} cm^{-1}$, according to the provided datasheet [69].

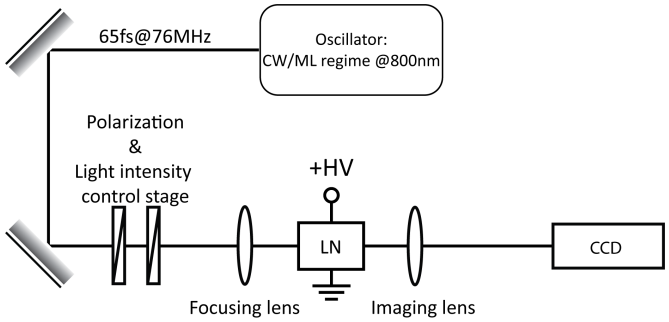

Figure 3.4: Typical setup employed to write solitonic waveguides in the volume of lithium niobate.

To emphasize the photorefractive nature of the self-induced waveguide, two kind of measurements have been performed. The average light power @800nm and the external electric field are kept constant. By injecting the laser beam working in CW regime before and in ML one after, it will be demonstrated that self-trapping can be achieved only if a second harmonic seed is present. Considerations about other possible nonlinear effects which could arise during the process induced by the femtosecond pulses will be discussed.

The 800nm beam is focused on the input face of the sample with a waist of 12μm and an average power of 16mW, fig. 3.5a -I-. After a propagation of 6mm it diffracts reaching the final waist of 96μm. A uniform background illumination, having an intensity of 70mW/cm^2, is provided by a CW laser, $\lambda = 532$nm, and it is injected from one side to shine the whole sample and so to stabilize the self-trapping process by preventing the charge saturation in the illuminated region.

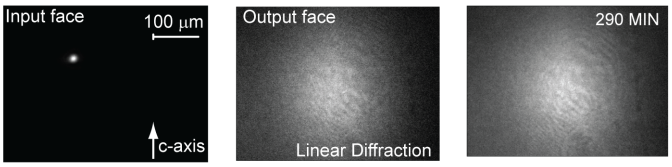

(a) No photorefractive response of $LiNbO_3$ when the 800nm beam in CW is focused on the input face of the sample (-I-). Linear diffraction (-II-) doesn't react to the externally applied electric field and after 290min the shape is not changed (-III-).

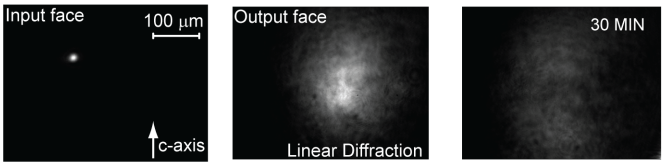

(b) Self-defocusing case. When the 800nm is focused on the input face of the sample in ML regime (-I-) and no external electric field is applied, the linear diffraction (-II-) increases along the ĉaxis as consequence of the photovoltaic effect (-III-).

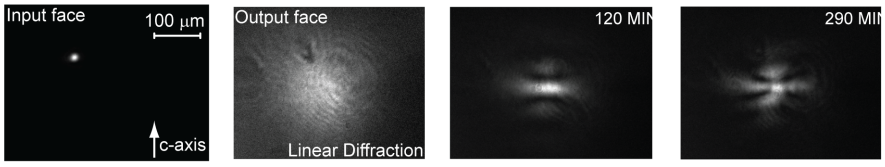

(c) Solitonic waveguide formation when the fundamental beam, 800nm in ML regime, is focused (-I-) on the input face of the sample and a type0 ($ee - e$) second harmonic beam is generated inside the sample. Under the application of an external static electric field, linear diffraction (-II-) starts to be compensated (-III-) and after 290min self-trapping results to be completely achieved (-IV-). A multihump structure appears when self-confinement is complete.

Figure 3.5: Photorefractive response of $LiNbO_3$ to 800nm in different experimental conditions: fig. 3.5a in CW regime; fig. 3.5b in ML regime but without having applied the external E_{bias} and fig. 3.5c ML regime with $E_{bias} = 35KV/cm$.

When the fundamental beam is working in CW regime and an external static electric field is applied to induce a positive refractive index variation, the diffracted beam does not change at all in shape during an observation time of about three hours. Neither self-trapping nor self-defocusing could be observed, fig. 3.5a -II- and -III-.

On the contrary, if the 800nm beam is injected in ML regime, with a pulse duration of 65fs and a repetition rate of 76MHz, both self-trapping and self-defocusing can be achieved. In details, with this configuration, and without applying the static electric field, the beam defocuses along the direction of the $\hat{c}$ axis as expected in presence of the photovoltaic effect and after 30min linear diffraction, fig. 3.5b -II-, results strongly elongated along it, fig. 3.5b -III-.

If the external electric field ($E_{bias} = 35KV/cm$) is applied, a complete self-trapping is obtained after about 290min, fig. 3.5c. In this regime, conversely to what happens in CW measurements in visible (reported in the first chapter), the final self-trapped structure is characterized by the presence of four bright lobes along the $\hat{c}$ axis and its perpendicular around the main guiding structure, fig. 3.5c -IV-. This result might be explained by a not perfect mode matching inside the written waveguide. As regards the trend for the self-trapping process evolution, in fig. 3.6a is reported the waist size modification trend, along the $\hat{c}$ axis. This result is typical of a photorefractive behaviour [9], in fact from CW measurement it had been demonstrated that along this direction waist size versus time can be fit by a single exponential curve. In this case the novelty is represented by the presence of an additional multihump structure, inset in fig.3.6a.

These results in CW regime are compatible with expectations. It is known that photorefractive response in undoped $LiNbO_3$ is very low at 800nm as, at this wavelength, energy is not enough to promote electrons to the conduction band from the trap states into the band gap. The presence of the background illumination could help the process by supporting a two step excitation as reported for holograms writing in the infrared regime. Low energy photons cannot modify the refractive index but, if a more energetic radiation is present (green for example), they can be excited to trap states closer to the conduction band and from there they can be directly promoted by the IR radiation in the conduction band, [46, 147, 148]. Performed measurements show that photorefractivity in lithium niobate cannot be excited by a 800nm beam in CW regime and that the uniform green background illumination is not high enough to induce a GRIIRA (GReen Induced Infrared

Absorption) process, fig. 3.5a.

Conversely, the behaviour in the ML regime can be affected by many nonlinear processes. In the last case, even if the average power injected is the same, the peak intensity is much higher than the one for the CW: $0.7GW/cm^2$ versus $2.6kW/cm^2$, so Kerr effect, self-phase modulation, second harmonic generation, multi photons absorption or cascading effect could be present.

Observing the light exiting from the sample, the presence of a blue component was quite evident, so the spectral composition of the emitted radiation has been investigated. This measurement demonstrated, as expected, that a second harmonic generation inside the sample had been achieved and the polarization of the generated blue light, 400nm , has been verified to be extraordinary, as for the injected fundamental beam. In fig. 3.6b, the comparison between the spectrum of the fundamental, at the output of the sample, and second harmonic generated beam is reported, for a fundamental beam average power of 20mW. The second harmonic emitted power has been measured to be in the order of 60nW. This value is still affected by a residual fundamental beam which could not be completely removed, so SH generation efficiency results to be in the order of 10^{-6}. These measurements show that the SH seed is responsible for the self-trapping process as at 400nm the photorefractive sensitivity is quite strong in $LiNbO_3$. As soon as the SH component starts to induce self-trapping, also the FH feels the refractive index variation and in turn is trapped inside it. At the end of the process, both the beams will be spatially self-trapped into a waveguide optimized for both.

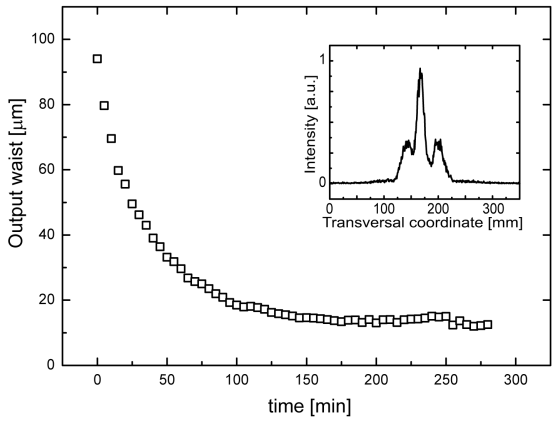

(a) Beam waist evolution for the 800nm beam along the "fast" direction (ĉ axis) at the output face of the sample. In the inset the multihump structure along this direction is reported. By fitting the central lobe, a single exponential trend can be derived.

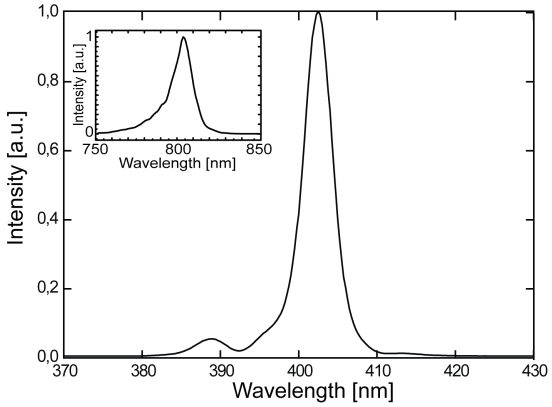

(b) Second harmonic spectrum measured at the output of the sample (in the inset is reported the spectrum of the fundamental beam). No distortion is present in the fundamental frequency spectrum as a consequence of the cascading nonlinearity absence, while the second harmonic component shows an evident frequency modulation which is responsible for pulse breaking. As a consequence of such phase modulation phase- and group-velocity locking were originated.

Figure 3.6: Second harmonic evidences in photorefractive self-trapping process at the output of the $LiNbO_3$ sample: (a) waist trend for the fundamental beam during the self-confinement process along the fast axis (ĉ axis) and (b) spectrum of the second harmonic signal.

To give a further demonstration about the fact that it is the blue seed to cause self-trapping, a BBO sample has been used to generate a SH component for the 800nm beam. This component, of about 700nW, was focused on the input face of the $LiNbO_3$ sample, fig. 3.7 -I-. By the simultaneous use of a prism and interferential filters, the fundamental component is removed. Keeping constant all the experimental parameters as in the previous measurements, the 400nm beam has been focused on a waist of 9μm at the input face. After about 12 min., self-confinement has been completely achieved with a final waist of 8μm at the output face, fig. 3.7-III-.

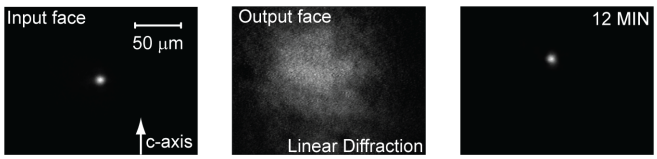

Figure 3.7: Verification for the necessity of a SHG seed to obtain self-trapping. A 400nm component with waist of 9μm and power of about 700nW is obtained from a BBO sample and is focused on the input face of $LiNbO_3$. Linear diffraction is compensated and self-trapping is achieved after 12min.

By comparing the FH spectrum, acquired at the output of the sample, with the SH one, spectrum broadening does not appear, giving an indication [149, 150] of the fact that cascading and self phase-modulation processes don't take place. Actually this result is intensity dependent but with the employed experimental conditions their contribution are expected to be negligible. In fact, being the generation efficiency so low, 10^{-6}, the superimposition of the component at ω resulting from a complete cascading process [151, 152], with the same component injected in the sample, results to be negligible.

Furthermore also Kerr effect, $\chi^{(3)}$, is expected to be negligible as the measured coefficient [153] for a sample bought from the same customer is reported to be $1 \cdot 10^{-19}\mathrm{m}^2/\mathrm{W}$ in the near infrared.

In terms of multiphoton absorption, being demonstrated the presence of a second harmonic seed, it looks that the favourite process is the linear photorefractive absorption of a photon at 2ω more than a nonlinear absorption

of two or even more photons at the fundamental wavelength.

3.6 Simulton

The geometrical configuration used to perform a second harmonic seed induced photorefractive soliton (section 3.5) is characterized by the propagation of the two locked (FF and SH) and the free (SH) pulses along the same direction because of the orthogonal fundamental beam incidence on the sample. In this case it is not possible to distinguish the contributions offered by the two second harmonic pulses and their behaviour in presence of the photorefractive nonlinearity.

Here the self-trapping process related to the locked pulses will be investigated with some more details [154]. Phase and group velocity locking implies that if self-trapping can be achieved, then the final structure is spatially confined, but they also propagate locked in time thus realizing a "simulton". It does not deal with two pulses for which also temporal dispersion can be achieved, so the final result is not a spatial-temporal soliton (a light bullet).

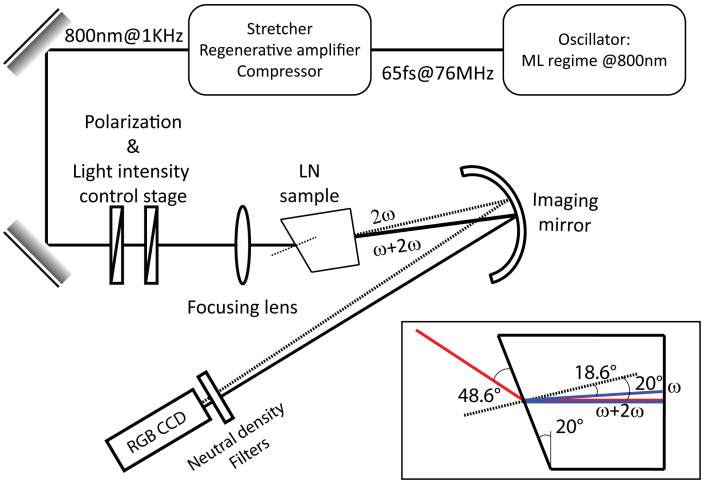

Figure 3.8: Experimental setup to investigate the simulton formation in lithium niobate with a type-0 (ee − e) coupling. In the inset, pulse direction angles with respect to the normal incidence on the input face are depicted.

As the two SH pulse generation is operated by the material itself, using

the terminology introduced by Bloembergen, by the interface air-nonlinear material, the necessity of separating the two pulses at the very beginning of their propagation path inside the bulk arises. The easiest way to do this is to focus the fundamental beam on the sample 20° cut face. The prism will separate colours according to the Snell-Cartesio law and they will propagate gaining an high enough separation at the output face of the sample.

Experimentally, the input beam at 800nm is focused on the input face of the sample, the cut one. A curved mirror is used to imagine the output face of the sample on a CCD camera sensor so avoiding the chromatic aberration given by the wavelength differences and providing at the same time a known magnification, as reported in the schematic setup of fig. 3.8. Again, to maximize the overall generation performances, we take advantage of an $ee - e$ (type-0) interaction by selecting the extraordinary polarization for the 800nm beam. The use of this experimental configuration has the advantage of imaging at the same time both the fundamental and second harmonic beams on the same sensor and in turn it allows the direct comparison between them. In the inset of fig. 3.8, the calculated values of the three pulse propagation trajectories with respect to the normal incidence are emphasized. To distinguish the pulse wavelength with reference to their position, a RGB camera is used. This allows to separate the three colour planes and so to investigate each pulse behaviour.

With respect to the self-trapping experiment reported in the previous section, in this case another element of novelty is introduced. The application of the external bias field is realized by heating the sample with a Peltier cell. In this way the pyroelectric effect [28] is excited as it can induce an electric field, in the order of tens of kV/cm, high enough to compensate the photovoltaic field and induce the self-trapping [39].

The self-trapping process is expected to be dependent on the fundamental beam intensity, and over a threshold, other nonlinear process in addition to the photorefractive one, could appear. In the following, measurements by varying the injected light intensity will be presented. In details, it will be shown that three different behaviours can be distinguished.

When a power of about 120μW or less, is injected into the sample, the generated second harmonic is not high enough to induce self-trapping, at least during the observation time. The 800nm shape does not change in an appreciable way at the output face of the sample, fig. 3.9a.

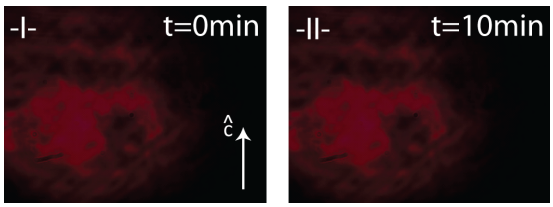

(a) Diffraction of the fundamental beam (800nm) at the output face of the sample for a power of 120μW. -I- At $t = 0$ when no heating is applied and -II- after $t = 10$min in presence of the induced electric field. Neither second harmonic nor fundamental beam self-focusing is achieved.

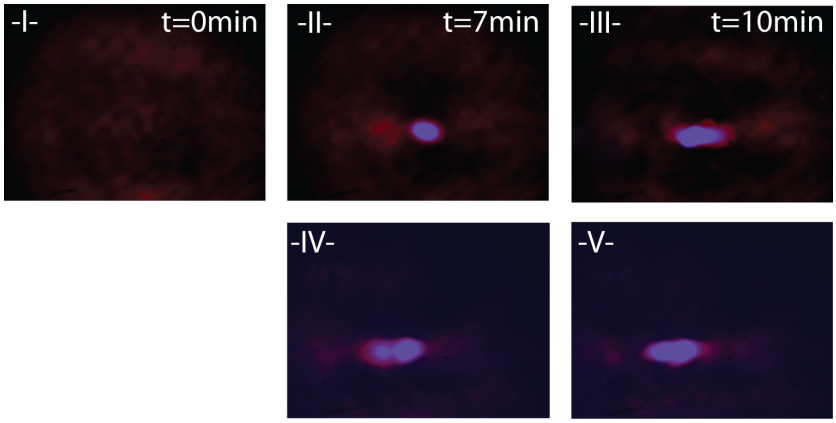

(b) Diffraction of the fundamental beam (800nm) at the output face of the sample for a power of $160\mu\text{W} - 180\mu$W. -I- At $t = 0$ when no heating is applied. -II- and -IV- after $t \simeq 7$min in presence of the induced electric field without and with a blu uniform background illumination. -III- and -V- after $t \simeq 10$min in presence of heating and without and with background illumination, respectively.

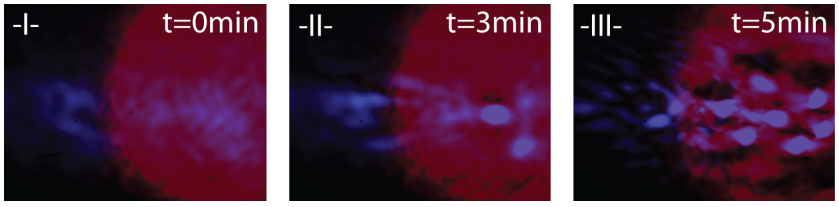

(c) Diffraction of the fundamental beam (800nm) at the output face of the sample for a power of $\simeq$ 1mW. No background illumination is applied. -I- At $t = 0$ when no heating is applied. -II- and -III- after $t \simeq 3$min and $t \simeq 5$min respectively in presence of the induced electric field. A filamentation behaviour is obtained.

Figure 3.9: Locked FH and SH and unlocked SH pulses self-trapping in function of the injected light intensities.

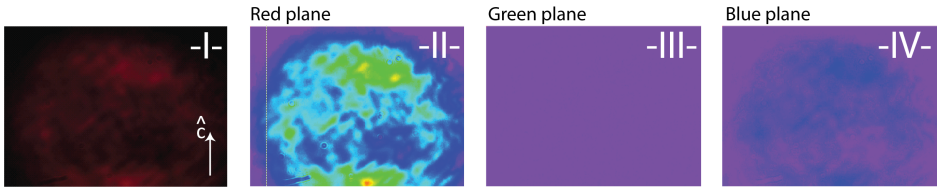

(a) Self-trapping process at t=0 (fig. 3.9b -I-). The pyroelectric-induced space charge field is not strong enough to screen the photovoltaic contribution induced by the weak blue component. Beams at 800nm (in -II-) and at 400nm (in -IV-) elongate along the optical axis direction.

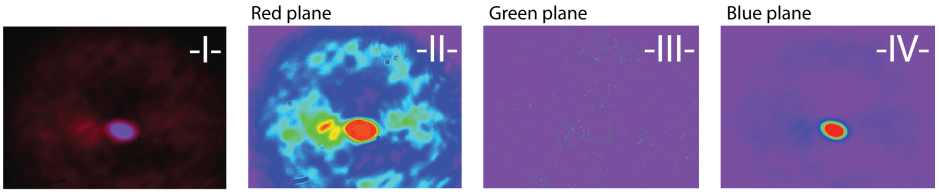

(b) Self-trapping condition for the two locked pulses and for the unlocked one at its very early stage (fig. 3.9b -II-). Each of the two blue pulses generates a waveguide in which also the infrared is driven. The 800nm beam propagates inside the blue locked pulse-induced collinear waveguide. The free blue pulse guides only a residual scattered fundamental beam, also in function of the 800nm beam k-vector dispersion.

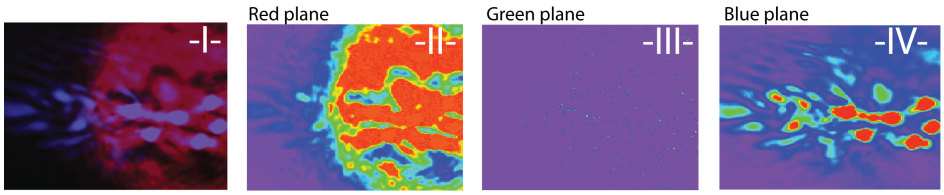

(c) Filamentation condition. Each filament realizes a waveguide for the fundamental beam. The quantity of transported 800nm light depends on the k-vector dispersion of the fundamental beam with respect to each guide propagation direction. The information about the nature of the two blue original pulses is lost.

Figure 3.10: Details about self-trapping and filamentation processes, reported in fig. 3.9, analyzed by separating the three RGB coulour planes.

On the contrary, when the power is increased to $160\mu\text{W} - 180\mu\text{W}$, at the very beginning of the process the photovoltaic contribution driven by the blue light is predominant and an elongation along the $\hat{c}$ axis is induced. This effect is consequence of a heating which is not strong enough to produce a bias electric field able to screen the photovoltaic contribution, fig. 3.9b -

I-. By separating the three colour planes, the light displacement towards the illuminated region borders along the optical axis, is still more evident, fig. 3.10a. As soon as the space charge field becomes more effective, the second harmonic (the locked pulse) self-traps and forces the fundamental beam to be guided as well. This behaviour is justified by the charge depletion occurring for the infrared beam around the blue induced waveguide, fig. 3.9b. As regards the free pulse, it starts self-trapping only after that the locked one completes its self-confining process. This is somehow expected as the unlocked pulse, once generated, propagates along its own direction according the absorption rules for 400nm wavelength without possibility of being enhanced due to the lack of 800nm along that direction. Its intensity decreases and a longer time is required in order to make it self-trap. The locked 400nm pulse, on the contrary, starts writing the guide inside which the fundamental beam is captured and thus its second harmonic generation rate can be increased, so compensating for its absorption by the lattice. This behaviour is resumed in pictures fig. 3.9b -II- and in fig. 3.10b, where the three planes are separated. The blue plane indicates that in correspondence to a complete self-trapping for the locked blue pulse and a partial confinement for the free one, fig. 3.10b -IV-, infrared is guided through the induced waveguides fig. 3.10b -II- and the typical photorefractive space charge field depletion along the $\hat{c}$ axis appears. Once self-trapping is accomplished for both the structures, the second pulse, the free one, feels the refractive index variation induced by the locked structure and is attracted towards it without never collapsing, giving rise to a "twin-state" propagation, fig. 3.9b -III-.

The non collapsing can be explained if the conservation of the original $\vec{k}^{(2\omega)}$-vector for the second pulse is taken into consideration. This behaviour becomes more evident if a background illumination is applied to the sample 3.9b -IV- and -V-. A high power blue light emitting diode (LED) is applied directly over the surface of the sample to shine it completely, so preventing saturation inside the guiding structure and in turn to continuously excite the free charges via the photorefractive effects to make the process more stable.

By increasing the optical power, a filamentation-type behaviour is obtained, fig. 3.9c. The application of the bias electric field makes the locked blue pulse self-trap, fig. 3.9c -II-, but as the process evolves it starts splitting in multiple filaments. Also the free second harmonic pulse, again slower than the locked one in self-trapping, produces its own filaments. As a consequence, after some times it is no more possible to distinguish the contribution

of the two second harmonic pulses, fig. 3.9c -III-. Once formed, each of these filaments starts guiding the infrared fundamental radiation and in turn increasing the depleting region around each of them. The effective guiding properties of the induced waveguides can be exploited by comparing the red (800nm) plane and the blue one in fig. 3.10c -II- and -IV-, respectively. In fact, on the left side of the infrared beam, fig. 3.10c -II-, some spots appear, but as this plane is reserved to the red component, they should not be there. This is consequence of the corresponding blue filaments, fig. 3.10c -IV-, that propagate also the diffracted, residual, fundamental beam. It is worth noticing that the quantity of guided light inside them decreases with the distance from the 800nm beam. This is consequence of the increasing difference between the k-vectors associated to the fundamental beam and the direction of the blue-induced guides. These are characterized by a refractive index contrast as high as 10^{-4} and so they are not strong enough to capture these highly tilted k-vectors.

In comparison with the self-trapping process reported in fig. 3.5, the pulse peak intensity at 800nm increases from 1.6 GW/cm^2 (and thus an energy of about 0.2 nJ), to intensity values ranging between 0.7 TW/cm^2 and 1.2 TW/cm^2, corresponding respectively to energy levels of 0.1 μJ and 0.3 μJ. As conversion efficiency inside the waveguide is supposed to increase, cascading effects or nonlinear multiphoton absorption could be most likely present. At the moment further measurements are being performed to investigate with more details whether cascading is affecting measurements.

Chapter 4

Photorefractive interactions in InP:Fe for all-optical telecommunication devices

In the previous chapters, the advantages that photorefractive solitons offer have been demonstrated. The diffraction compensation provided by the photorefractive nonlinearity, along with the refractive index variation given by the Pockels effect, allows to realize both integrated optical sources and interconnections necessary to propagate the emitted radiation. They are volumetric and for the first time a real 3D circuitry can be realized with a very high degree of optimization. What is still missed, to obtain a working electro-optic, or better all-optical circuitry, is a final, volume-integrated, device able to elaborate optical signals. While in the past optical computing attracted much attention [155–159], today also information and communication technology play a critical role. Their state of the art presents again structures which can be only superficial, like switches and Mach-Zehnder interferometers or modulators.

Switches represent one of the most investigated devices in the framework of transparent optical networks [160, 161]

As regards modulators and Mach-Zehnder interferometers, two interesting examples projected towards a multi-purpose integrated device are reported by Söchtig [162] and Mašanović [163]. Both the papers present different devices that can successfully lay on the same substrate; the former, an integrated laser device followed by a Mach-Zehnder modulator/interferometer

and the latter reports also about a wavelength converter obtained with the same structure.

Signal elaboration, to be competitive with electronic devices, requires to be fast and to be fully fit to the actual telecommunication technology, so it must operate in the infrared region, better in the third window. What is proposed in this chapter is the demonstration of a working principle to achieve an electro-optical fast signal switching that can be used as a router device. This will be done by making two self-trapped beams interact in a photorefractive medium so to make them fuse or separate according to their relative properties. Here coherent interactions will be investigated, so the key parameter will be their relative phase.

As a router device needs to address signals over as many input and output ports as possible, a photorefractive medium is a very interesting candidate for such a device. This feature can be easily achieved because of the volumetric nature of spatial solitons, port (waveguide) number can be dynamically scaled according to the necessities and they can work in parallel.

On the contrary of what has been shown previously, in this case neither lithium niobate, nor other photorefractive insulators can be used. In fact, waveguide realization is not at all fast enough, as in the more optimistic case their formation time is in the order of seconds, in SBN for example, and minutes or even hours in lithium niobate. Furthermore their photorefractive responsivity is strong in the visible region, but negligible in the infrared one. To overpass these limitations, the semiconductor indium phosphide doped with iron ions (InP : Fe) is used. It provides both the features: speed (estimated in between the μs and ms) and photorefractive sensitivity in the infrared region.

InP:Fe is a relatively new material in the photorefractive family and its properties are not yet completely known, so before entering in the interaction process details, an introductory explanations about the main physical mechanisms involved will be done. The inadequacy of the one carrier-one band model used and discussed for lithium niobate will be emphasized introducing the necessity of a two carriers-two bands one. The photorefractive self-trapping will be discussed along with the interaction between two coherent beams which propagate parallel inside such medium, demonstrating the possibility of driving the fusion or the repulsion between them by simply changing their relative phase.

4.1 InP:Fe structural and optical properties

Indium phosphide has been used for many years both as substrate because of its very high resistivity and as semiconductor belonging to the $III-V$ group. It belongs to the "zincblende" family and exhibits a direct bang-gap of about 1.35eV. It is so characterized by a face centred cubic structure where atoms of indium (In) and phosphure (P) are alternatively disposed in correspondence to the lattice positions. InP is a non-centrosymmetric material belonging to the $\bar{4}$3m punctual group.

InP does not exist in nature but can be artificially grown using the Czochralsky technique [32, 164, 165]. Many different approaches have been proposed to increase the final crystal quality. It is firstly necessary to synthesize the polycrystalline InP compound. This is obtained in vacuum and at very precise and controlled environmental conditions, like fixed temperature (1062°C) and pressure (10^5Pa). Then the doping element (iron) is introduced in the melt and finally single crystalline boules can be grown. Also in this case temperature and pressure are fixed and an encapsulant liquid is used to cover the polycristalline InP. Pressure must be high enough to prevent InP from decomposing, so it must be in the order of 10^5Pa. Recently, a method to synthesize directly InP has been developed [166] and consists in using the phosphorus (P) element in the liquid phase both as encapsulant for the Czochralsky growth and as source element for the compound. In this way it is no more necessary to synthesize the polycrystalline compound and to add the boric oxide (B_2O_3) as encapsulant. In the market it is possible to find single crystal wafers grown according to the crystallographic directions: $< 001 >$ and $< 111 >$.

In the following of this chapter, all the measurements are referred to a sample having a doping level as high as 10^{17}cm^{-3}. It has been measured via the Secondary Ion Mass Spectrometer (SIMS) technique. It is cut along the crystallographic directions: $< \bar{1}10 >$, $< 001 >$ and $< 111 >$.

The necessity for doping the bulk with iron is justified by the fact that only in this way it is possible to make this material photorefractive and sensitive in the third window infrared wavelengths, at the same time. Iron adds energetic levels in the band-gap so, in spite of the fact that its energy corresponds to photons at $\lambda \simeq 919$nm, photo-excitation can be obtained also by injecting less energetic photons. These aspects will be demonstrated in the following with more details.

Iron addition influences also the material carriers mobility. As it will

be deepened further on, photorefractive behaviour in iron doped indium phosphide is characterized by free electrons and free holes. With respect to the pure material, a mobility decreasing with doping increasing is expected [167] as well as a dependency on the working temperature. According to the rule for mobility in semiconductors, their effect can be distinguished in two terms in the general expression for mobility μ. In fact, doping will increase the impurity density and temperature will influence the phononic behaviour of the lattice. So mobility can be expressed as $1/\mu = 1/\mu_{\mathrm{I}} + 1/\mu_{\mathrm{L}}$, being μ_{I} and μ_{L} related to the impurities and to the lattice, respectively. In literature their specific values are found to be very different. With reference to [168–170], for electrons it can assume values ranging between 1470 cm^2/Vs and 5000 cm^2/Vs, while for holes it can vary between 120 cm^2/Vs and 150 cm^2/Vs, so at least one order of magnitude less. It is worth noting that in semiconductors, a change in temperature implies a modification in the band-gap. In the measurements further presented, this effect is considered negligible. In fact, sample temperature will range between 15°C and 25°C and according to [171] it corresponds to a net gap variation of about 3meV.

Optically, InP : Fe provides a bulk refractive index n_0 =3.29 @1064nm and n_0=3.17 @1550nm. Thanks to its crystallographic property of presenting a non-centrosymmetric structure, it exhibits also a linear electro-optic behaviour which grants the possibility of locally modifying the bulk refractive index via the typical photorefractive process.

In analogy to the basic principles about the photorefractive effect described for lithium niobate, also in this case it is necessary to apply a bias electric field to induce a positive refractive index variation able to make light self-trap. The electro-optic tensor to be considered depends on the direction along which this field is applied. Because of the geometry of the sample that will be used, the condition of E_{bias} directed along the $< 001 >$ direction is considered, so the refractive index variation is described by eq.(4.2). In the frame, eq. (4.1), are reported respectively: the general expression for the indium phosphide electro-optic tensor and the impermeability tensor corresponding to the considered direction for the applied electric field. The value for the only non-zero coefficient is $r_{41} \simeq 1.34\mathrm{pm\,V^{-1}}$. It is worth noting that this value is extremely low if compared to the more common insulators ones ($30\mathrm{pm\,V^{-1}}$ for $LiNbO_3$ and $1340\mathrm{pm\,V^{-1}}$ for SBN:75). As it will be demonstrated in the next sections, self-trapping can be achieved only because of a resonance effect that the involved (photorefractively excited) charges create

for the space charge field.

$$\begin{bmatrix} r_{11} & r_{12} & r_{13} \\ r_{21} & r_{22} & r_{23} \\ r_{31} & r_{32} & r_{33} \\ r_{41} & r_{42} & r_{43} \\ r_{51} & r_{52} & r_{53} \\ r_{61} & r_{62} & r_{63} \end{bmatrix} = \begin{bmatrix} 0 & 0 & 0 \\ 0 & 0 & 0 \\ 0 & 0 & 0 \\ r_{41} & 0 & 0 \\ 0 & r_{41} & 0 \\ 0 & 0 & r_{41} \end{bmatrix} \Longrightarrow \Delta\eta = \begin{bmatrix} 0 & 1 & 0 \\ 1 & 0 & 0 \\ 0 & 0 & 0 \end{bmatrix} \tag{4.1}$$

$$< 001 > \qquad n = n_0 \tag{4.2a}$$

$$< 110 > \qquad n = n_0 - \frac{1}{2} n_0^3 r_{41} E \tag{4.2b}$$

$$< \bar{1}10 > \qquad n = n_0 + \frac{1}{2} n_0^3 r_{41} E \tag{4.2c}$$

4.2 Temperature and illumination role on InP:Fe photorefractivity: electron-hole competition effect

Indium phosphide has been really overworked to realize devices based on its elevated resistivity as substrate or to produce laser devices as well as photon counting sensors, but it is relatively new in the framework of photorefractive materials.

This feature is obtained by adding iron ions in the melt, so to add trap states into the band-gap. These levels, providing additional donors and acceptors (Fe^{2+}, Fe^{3+} respectively) are located approximately in the centre of the band-gap [172]. They are thought to be the main responsible for free charge generation and recombination, upon illumination, inside it.

The photorefractive mechanisms discussed for lithium niobate, photoexcitation - diffusion/drift - recombination, remain unchanged (with the exception of the photovoltaic field). On the contrary, the one free carrier (electrons) assumption does not find any kind of agreement with the experimental results.

All the informations known about InP have been obtained via two wave mixing (TWM) measurements. It consists in making two beams (pump and

signal) interfere in order to induce fringes and, via the Pockels effect, photorefractive index variations. These scatter the light from one beam (pump) to another (signal) and provide a photorefractive gain Γ for the latter. It is this gain to provide the inconsistency with the basic model (considering only free electrons). In fact, gain is proved to depend on the induced grating period (so on light) and the temperature. By varying these parameters, a change in the Γ sign appears. This evidence led to the conclusion that carriers having opposite sign had to play a role in this process and that the predominant one decide the Γ sign according to the experimental conditions.

Many models based on TWM schemes have been developed, but a real working one does not exist yet to describe photorefractive measurements. To introduce to this problematic and to give a better insight for the interaction measurements, a brief overview about model evolution and their key points will be provided.

Since the beginning, it appeared clear that the experimental results could not be explained taking into account just one carrier type: electrons. Because of this, also holes had to be considered. One of the first attempt to measure carriers photoionization and recombination cross sections must be addressed to Valley [173] at $\lambda = 1064$nm. Initially, just one impurity centre in the band-gap was hypothesized, so it acted both as electron and hole generation centre, according to its ionic state [174] towards conduction or valence bands respectively. This model gave a much better fit for experimental measurements but still needed to be revised [168]. Again both electrons and holes are considered, but they are supposed distributed over two sets of defects: one for which the dominating carriers are electrons and an other one characterized by holes. A comparative analysis of results, obtained under the assumption of carriers provided by only one set or two sets of defects, has been carried out by Bashaw [175].

These models, although introducing holes as active centres, did not take into account the temperature effect, which strongly influences the material response, as it will be shown both for the single beam self-trapping and the two beam interaction. Picoli et al. [169, 176] introduced it in their model. Numerical results are quite in agreement with the experimental measurements but emphasized some aspects which are still under investigation for beam self-trapping processes. They suggest that a deep level (iron for indium phosphide) in the band-gap can interact both with the conduction and the valence band and that these interactions can be both optical and thermal. Furthermore, they take into considerations other levels, very close

to the two bands. These are supposed to be introduced in the growth phase and to play a role only in terms of "residual" conductivity and not of photorefractivity. What is important in the model is the combined action of temperature with injected light; it can induce a resonance-like behaviour that can strongly increase the photorefractive gain Γ. This peak is characteristic for each couple light intensity-temperature. Thermal and optical generations are then weighted according to a comparison between the corresponding cross-sections (estimated as not completely known), arriving to the conclusion that electrons and holes are respectively thermally and optically generated. This statement is justified by experimental evidences. Hole photo-ionization cross-section is larger than the one for electrons $\sigma_{\mathrm{h}}^{\mathrm{ph}} > \sigma_{\mathrm{e}}^{\mathrm{ph}}$ and the thermal emission rate for holes is much less than the one for electrons $\mathrm{e}_{\mathrm{h}}^{\mathrm{th}} << \mathrm{e}_{\mathrm{e}}^{\mathrm{th}}$. With reference to [169, 177], the photo-ionizations at $\lambda = 1.064\mu$m assume values: $\sigma_{\mathrm{h}}^{\mathrm{ph}}$=$5 \cdot 10^{-17}\mathrm{cm}^2$ and $\sigma_{\mathrm{e}}^{\mathrm{ph}}$=$4 \cdot 10^{-18}\mathrm{cm}^2$. As regards electron thermal generation rate, for the same wavelengths, it can be calculated as a function of the working temperature from the expression [169,178]: $\mathrm{e}_{\mathrm{e}}^{\mathrm{th}} = 3.25\mathrm{T}^2 \cdot 10^{25}(\mathrm{m}_{\mathrm{e}}^*/\mathrm{m})\sigma_{\mathrm{n}}^{\infty}\exp(-\epsilon_{\mathrm{na}}/\mathrm{K_B T})$. T is the temperature in Kelvin, $\mathrm{m}_{\mathrm{e}}^*/\mathrm{m} = 0.078$ the ratio between the electron effective mass and the free electron one, $\sigma_{\mathrm{n}}^{\infty} = 3.5 \cdot 10^{-14}\mathrm{cm}^2$ the capture cross section for infinite temperature and $\mathrm{K_B}$ the Boltzmann constant. ϵ_{na} represents an activation energy for the single electron trapping by an iron acceptor. The value for holes is not known but is assumed to be much smaller (and typically considered zero) as the deep level from which they originate is much closer to the conduction band. Resonance occurs when the thermal generation rate for electrons is equal to the optical one for holes. Özkul and Picoli demonstrated also [179] that the addition of a bias electric field could increase the photorefractive gain, and could derive an approximated analytical expression for the space charge field.

Other improvements have been reported by Rana [180], who took care about some low temperature inconsistencies solved introducing a generation/recombination centre in addition to the iron one in the band-gap, and by Özkul [170, 177] who confirmed these results and placed this additional level close to the valence band.

The problem is no more completely solved, and at the moment the state of the art consider an energetic level scheme based on the one proposed by Look [172] which is reported in fig.4.1. In this scheme also levels proposed by Rana and Özkul have been added. In the band-gap an energetic level

indicated with Fe^{2+*} is also reported and it has been demonstrated to be responsible for an indirect hole-electron competition [181]. Anyway, it has been proved not to give any photorefractive contribution in the range of temperature further on used, so it is considered negligible. For sake of completeness anyway, it allows direct photoexcitation of electrons from the valence band and a thermal one to the conduction band along with hole recombination as well.

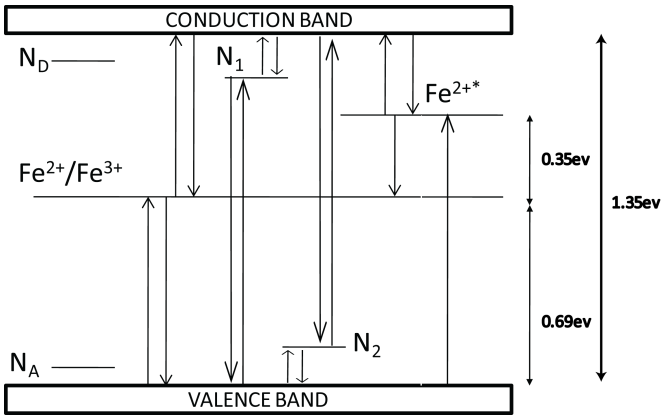

Figure 4.1: Energetic levels for InP:Fe.

A modified Kukhtarev model is used to describe charge movements in terms of two carriers (electrons and holes) in a two bands scheme. The equation system is:

$$\vec{\nabla} \cdot \left(\tilde{\epsilon}\vec{E}_{SC}\right) = \rho \tag{4.3a}$$

$$\rho = e(N_D - N_A + p - n - n_T) \tag{4.3b}$$

$$\vec{J_n} = e\mu_n n\vec{E}_{SC} + \mu_n K_B T\vec{\nabla}n \tag{4.3c}$$

$$\vec{J_p} = e\mu_p p\vec{E}_{SC} - \mu_p K_B T\vec{\nabla}p \tag{4.3d}$$

$$\frac{\partial n}{\partial t} = e_n n_T - c_n n p_T + \frac{1}{e}\vec{\nabla} \cdot \vec{J_n} \tag{4.3e}$$

$$\frac{\partial p}{\partial t} = e_p p_T - c_p p n_T - \frac{1}{e}\vec{\nabla}\cdot\vec{J_p} \tag{4.3f}$$

$$\frac{\partial n_T}{\partial t} = e_p p_T - e_n n T - c_p p n_T + c_n n p_T \tag{4.3g}$$

$$N_T = n_T + p_T \tag{4.3h}$$

$\tilde{\mathrm{E}}_{\mathrm{SC}}$ represents the space charge field, $\tilde{\epsilon}$ the dielectric tensor, ρ the volumetric density charge and $\tilde{\mathrm{J}}_{\mathrm{n,p}}$ the current densities for electrons and holes respectively. n and p are the electron and hole densities, while $\mathrm{n_T}$ and $\mathrm{p_T}$ indicate the ionized and neutral deep level iron traps ($\mathrm{Fe}^{2+}, \mathrm{Fe}^{3+}$). $\mathrm{N_D}, \mathrm{N_A}$ are the donor and acceptor densities and are constant. Electrons and holes mobilities are indicated with μ_{n} and μ_{p}, the corresponding recombination rates are $\mathrm{c_n}$ and $\mathrm{c_p}$ and their emission ones are $\mathrm{e_n}$ and $\mathrm{e_p}$. Emission rates take into account both the thermal (th superscript) and optical (defined via a photoionization cross section σ) according to: $\mathrm{e_n} = \mathrm{e_n^{th}} + \sigma_{\mathrm{n}}(\mathrm{I} + \mathrm{I_d})$ and $\mathrm{e_p} = \mathrm{e_p^{th}} + \sigma_{\mathrm{p}}(\mathrm{I} + \mathrm{I_d})$. I and $\mathrm{I_d}$ represent light and dark intensity respectively. Finally, with T and $\mathrm{K_B}$ have been indicated the absolute temperature and the Boltzmann constant. This model has been recently used [182, 183] to get self-trapping process description inside InP : Fe, with results close to the experimental evidences.

4.3 From two wave mixing to one beam self-trapping process in InP:Fe

Self-trapping process for an infrared beam in iron doped indium phosphide is very disadvantaged by its low electro-optic coefficient ($\mathrm{r_{41}} = 1.34\mathrm{pm/V}$) but in spite of this fact, optical self-trapping has been experimentally observed.

The first evidence must be addressed to Chauvet at al. [13,184] who succeeded in making infrared beams self-trap, in a planar structure before and along both the transverse dimensions after, at telecom wavelength (1.04μm, 1.3μm). They address self-trapping to the resonant behaviour (explained with more details in section 4.6) for the space charge field that reaches values much higher than the applied bias electric field, so compensating for the low $\mathrm{r_{41}}$ coefficient. Using an interferometric technique they also measure an induced refractive index variation as high as $\delta\mathrm{n} = 10^{-4}$.

This material is very attractive in the framework of beam-self trapping as a consequence of its semiconductor nature. In spite of iron doping that reduces its response time, the steady state regime can be attained in a time (over-)estimated that is in the order of ms. For the transient regime this time is supposed to decrease by a factor of 10^3. This has been reported by Wolfersberger et al. [14] for the wavelengths 1.064μm and 1.55μm.

Recently a (2+1)D numerical model has been published [182]. It takes into account the Kukhtarev's equation system re-written for the case of two free charges and a single deep model, providing results which are in agreement with the previous experimental works.

4.4 Self-trapped beams and coherent interactions

The realization of an all-optical switching or coupling device requires to access the possibility of driving the behaviour of two or more photorefractive solitons just taking advance of light properties. Performances that such a system must provide are the possibility of fusing into a unique guiding structure or to increase their initial separation.

To achieve this result, the coherent interaction process between self-trapped beams will be experimentally investigated. Up today, photorefractive collisions have been experimentally realized in the insulator SBN at frequencies in the visible region [185–189]. In the proposed analysis, the InP:Fe semiconductor, working at infrared (telecom) wavelengths, is used so to obtain the further advantage of increasing the whole process response time by orders of magnitude. Coherent interactions, on the contrary of what allowed by the incoherent ones can make possible both fusion and repulsion according to the relative phase existing between the two beams. In the incoherent case [190–192], in fact, only fusion can be induced as a consequence of the increased total intensity in between the two beams. Photorefractive coherent interactions can take to an efficient fusion between the two beams other than their repulsion. This is consequence of the partially inelastic nature of collisions, thus soliton annihilation or new solitons birth can be achieved as well [186, 187]. This is a novelty element with respect to the Kerr type [193] for which collisions are rigorously elastic and consequently soliton speed, energy and number of solitons are always kept. In turn, this implies that one-dimensional Kerr collisions can only take to a temporary fusion of the two beams which separate afterwards.

Photorefractive collision process is local, in the sense that is based on the superposition degree between each beam induced refractive index variation region. Effects are expected to be maximized for an almost complete overlapping and negligible for far enough beams. On the contrary, nonlocal media allow beam interactions for much higher beams separations [194]. In this case, another kind on nonlinearity is required, for example the one provided by the optical thermal nonlinearity (heating transfer between the beams). The physical process driving fusion or repulsion in a photorefractive medium is based on the interference pattern that the two beams create, and it is in this framework that their relative phase plays a role. If the two beams are in-phase ($\Delta\phi = 0$) then the constructive interference between them will increase the light intensity pattern and if out of phase ($\Delta\phi = \pi$) a minimum for it should appear in between them (ideally the fringe space modulation should reach its maximum value m=1). The photorefractive nature of $InP : Fe$ reacts to this modifications inducing a refractive index change which is function of the space charge field created by the increasing of the local illumination or its decreasing. In the first case, the two beams will be attracted towards the centre, so fusing, while in the other they will increase their separation.

This aspect is often described in terms of attractive or repulsive forces that each soliton exertes on the other one being it considered as a "particle-like" entity. Some models trying to quantify these forces have been developed so far [195, 196].

To maximize these forces is indeed necessary to increase as much as possible the induced refractive index variation. This condition is locally realized in correspondence to the formation of a spatial soliton.

Other parameters must be briefly introduced, as to investigate the very basic properties of an interaction process inside this material, secondary effects like two wave mixing gain must be eliminated. They would play a role if an high enough number of fringes appeared in between the two co-propagating beams. In this case, the scattering would not be negligible and a photorefractive gain could appear. The induced grating path can be calculated with the usual expression for photorefractive gratings: $\Lambda = \lambda_0/(2\mathrm{nsin}(\theta))$. n is the average refractive index, 2θ the whole angle between the crossing beams and $\lambda = 1.064\mu$m. It can be found, fig.4.2, that starting from a relative inclination of 0.4 degrees, full angle, fringes can reach a size comparable to each beam transverse dimension. To avoid this, the two beams are injected and let propagate along parallel directions inside

the sample. Furthermore, this configuration allows to reduce as much as possible eventually present angular momenta. For the in-phase condition, they could induce a spiralling behaviour [197] between the two "particles". This is consequence of the perfect balancing between each soliton centrifugal force and the relative attraction force, with the consequence that they would propagate without fusing.

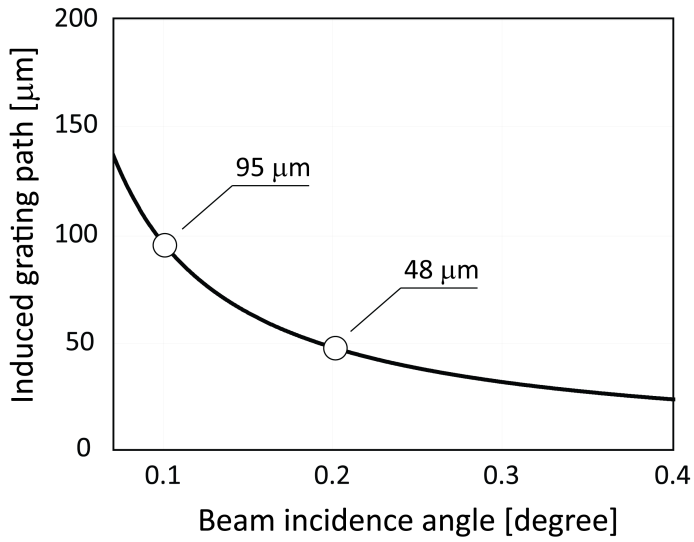

Figure 4.2: Photorefractive induced grating period for two crossing beams. The graph is plot versus half of the whole angle and for a $\lambda = 1.064\mu$m.

4.5 Coherent interactions: experimental setup

Experimentally, interaction measurements have been performed by injecting, inside the sample, two focused identical beams, extraordinarily polarized and in continuous wave regime, fig.4.3. A laser with wavelength $\lambda = 1.064\mu$m is firstly mode-cleaned via a monomodal optical fibre, collimated and then divided in two arms by a Mach-Zehnder interferometric scheme.

These two beams are then focused on the input face of the sample to make them co-propagate along parallel directions. Being the beams collimated and focused using two identical lenses, the transverse dimensions in the focus and the linear diffraction properties, should remain the same for

both the beams. Along one of the two arms is placed a piezo-electric mirror that allows to change the relative phase with a resolution much higher than the employed wavelength, so to grant high accuracy in the relative phase regulation. Optical filters are also added to keep the two beam light intensities equal.

With reference to the crystallographic directions, light is made propagate along the 11mm long $< \bar{1}10 >$ direction and its polarization oscillate along the 5mm long $< 110 >$ one. Furthermore, parallel beam optical axis lie on the same plane along which the electric field acts, as in the inset of fig.4.3.

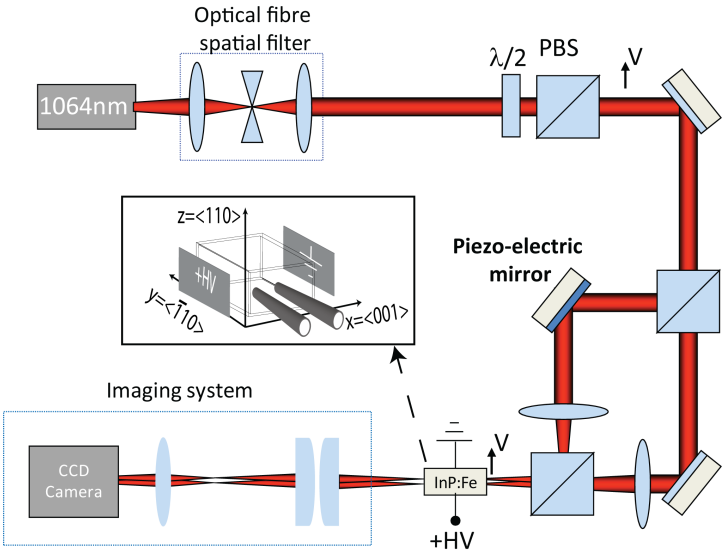

Figure 4.3: Experimental setup employed to study coherent interactions between two co-propagating parallel beams. In the inset, the crystallographic directions are emphasized according to the bias field application one and beam relative positions.

An optical system is then used to conjugate the output face of the sample on the sensor of an infrared camera, providing at the same time an optical magnification of about ten times. This optical device is composed by a couple of plano-convex lenses disposed to reduce aberrations and in a 2f-2f configuration. A microscope objective (10X) is then placed to conjugate the resulting image on the camera sensor with the ten time magnification. This optical system allows to measure the input beam waist size, to investigate

the formation dynamics at the output face and moreover to establish the initial beams relative phase. In fact, only one large fringe will appear between them on the input face so, by direct visual inspection, it is possible to distinguish its intensity level and thus to maximize or minimize it. Furthermore, magnification allows to reduce an eventual angle existing between the beams along the propagation direction because of the high enough CCD sensor resolution (squared pixel having side of 6.45 μm). The used camera has a response time which is longer than the transient evolution for the self-trapping process, so all the results that will be presented are relative to the steady-state condition.

Metallic electrodes are applied on the sample opposite facets along the 5mm long $< 001 >$ direction. A high voltage generator is used to realize the required bias electric field between them. To thermalize the sample to a constant temperature, a Peltier cell is placed along the same facets. Nevertheless a temperature gradient is anyway expected to exist between the Peltier application facets. As it will be further on demonstrated, the two beams stop interacting starting from distances between their centres in the order of three times their waist, so for a distance of $125 \div 130\mu$m along the $< 001 >$ direction. This permits to assume that in the small volume occupied by the two beams the imposed temperature remains constant.

4.6 One beam self-trapping: dependency on light intensity, temperature and input waist

As anticipated, the main issue that must be investigated is the identification of the best self-trapping conditions in order to locally increase as much as possible the refractive index variation and so to maximize the mutual forces between the two solitons. Involved parameters are: light intensity (I), temperature (T), bias electric field E_{bias} and input waist (w_{in}).

As first approach, sample temperature is stabilized at 20° C and light intensity for the single beam is varied checking the degree of self-confinement. For these measurements a waist $w_{in} = 25\mu$m is chosen and a bias electric field of 10kV/cm is applied; these values have been experimentally found and are in agreement with [14]. In fig.4.4, I have reported the ratio between the beam waist in nonlinear regime (so when the bias field is applied) and in linear diffraction, at the output face, as function of input intensity. This is an experimental curve that I calculated to determine exactly the self-focusing

properties of the sample under investigation according to its doping level. When the ratio is equal to one, the beam is in linear diffraction condition.

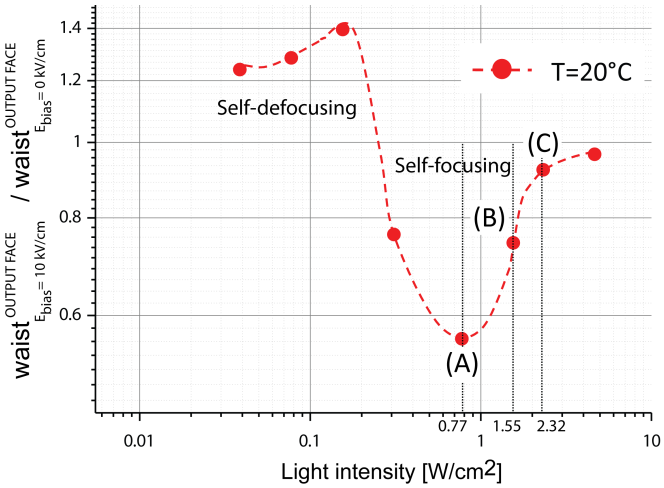

Figure 4.4: Self-focusing efficiency for the single beam for a fixed temperature of T = 20°C.

Two well defined regions can be identified: (a) for light intensities below 0.2W/cm^2, the beam self-defocuses when the bias field is applied; (b) for light intensities above 0.2W/cm^2, the beam self-focuses. The maximum self-focusing exists at about 0.77W/cm^2. The separation between these two regions, at 0.2W/cm^2, corresponds to a condition for which the application of the bias electric field does not influence at all linear diffraction (waist ratio equal to 1 in fig.4.4).

This curve could be in agreement with the theory according to which a resonant value exists for the induced space charge field, but the existence of such resonant condition (provided by an equal generation rates for electrons and holes, thermal and optical respectively) is not yet universally accepted [198]. It can thus be inferred that even if a real resonance cannot take place, a strong increasing for the space charge field is achieved as well, so to justify the maximum for self-focusing (point (A) in fig.4.4).

For different temperatures, this extremal point is expected to move.

A “resonant-like” behaviour has been demonstrated also for self-trapping in the CdZnTe semiconductor [15], but in this case carrier generation rules are opposite to what happens in InP:Fe.

In fig.4.5, a more detailed analysis about the transverse profiles of the input, the linearly diffracted and self-trapped beams is reported. It is interesting to note that self-trapping is not symmetric, it is negligible along the vertical direction (parallel to the light polarization oscillation) but efficient along the perpendicular one, the electric field application direction. When self-trapping is complete, the final dimension along it changes from about $w_{out}^{diff} = 52\mu m$ for the case of linear diffraction, to about $w_{out}^{E_{bias}} = 29\mu m$. So linear diffraction is not completely compensated.

When self-trapping approaches the steady-state regime, also a beam bending appears. According to the performed measurements and the optical regime, the beam moves along the bias electric field direction.

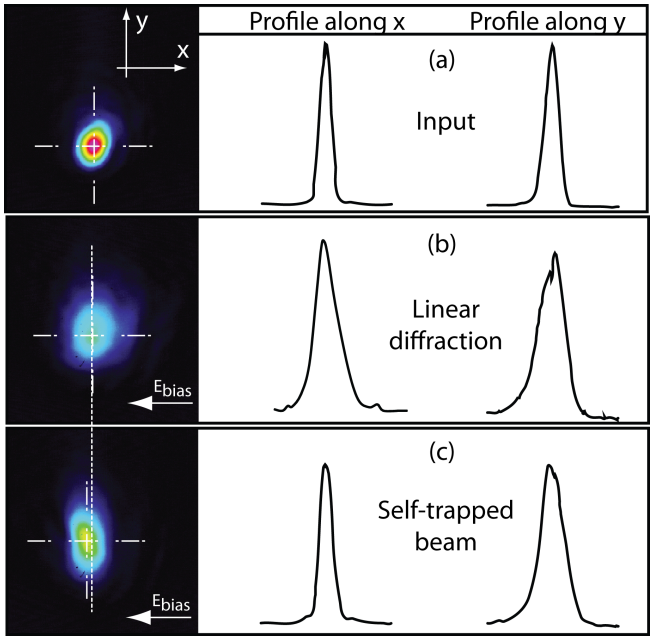

Figure 4.5: Beam transverse profiles (for $T = 20°C$, $I = 0.77 W\,cm^{-2}$, $w_{in} = 25\mu m$) at the input face (a) and the output face in the linear (b) and nonlinear regime (c), respectively. Upon the bias electric field application ($E_{bias} = 10 kV/cm$), self-confinement (c) is efficient along the x direction but negligible along the y one. Beam bending appears (c) along the same bias field direction.

If compared to lithium niobate, in which a typical self-trapped beam

size is in the order of 8μm, in indium phosphide the best self-confinement condition is found for an input waist of about 25μm. Smaller waists have been tried as well but, although a self-focused beam could be obtained, the final transverse profile was always accompanied by a lateral second peak. An experimental result is depicted in fig.4.6. It is relative to an input waist $w_{in} \simeq 19\mu$m and an intensity of 0.77W cm^{-2} which provides the strongest self-confined condition.

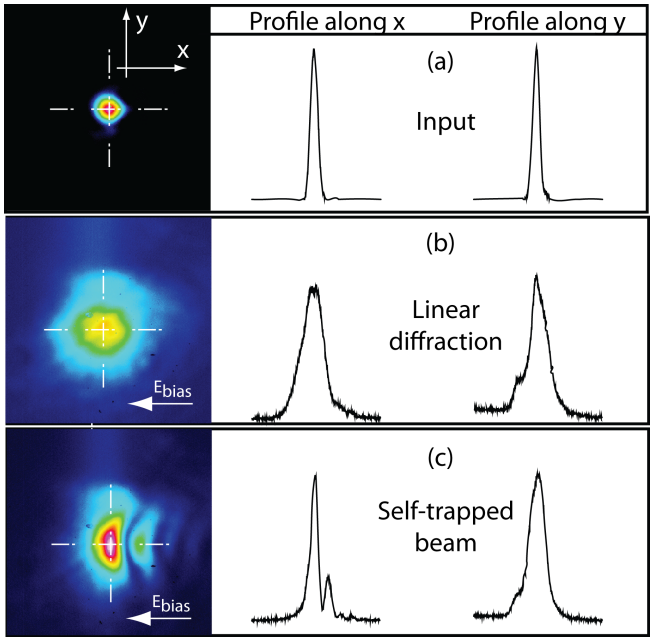

Figure 4.6: Beam transverse profiles (for T = 20°C, I = 0.77W cm^{-2}, $w_{in} = 19\mu$m) at the input face (a) and the output face in the linear (b) and nonlinear regime (c), respectively. Upon the bias electric field application ($E_{bias} = 10$kV/cm), self-confinement (c) occurs but a lateral second peak appears.

As beam waist reduction implies an increased linear diffraction, it might be inferred that the induced space charge field is not high enough to compensate for it. As a consequence, the whole injected light cannot be collected into the self-confined beam. This hypothesis can be further justified taking into account some of the numerical results proposed in [182]. According

to this numerical model, self-confinement is induced by the formation of a strong negative refractive index variation induced region that "pushes" the light into the positive and guiding one. In fig.4.7, the space charge field, the corresponding refractive index and the beam intensity profiles are reported for the steady state regime. Observing the transverse refractive index profile in fig.4.7 (c)-(d), two guiding regions (one much stronger than the other) surround the antiguiding one which completely separates them. The antiguiding region is characterized by a strong negative refractive index. Furthermore, the latter provides a curved shape for the guiding regions. All these elements are found in the proposed experimental measurements of fig.4.6.

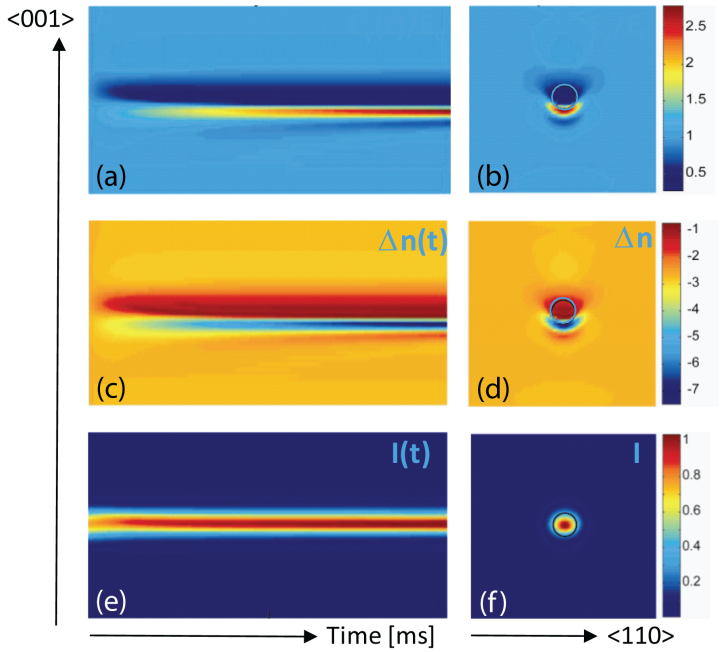

Figure 4.7: (Courtesy of Fabrice Devaux [182]) numerical description for the single beam self-confined condition at steady state. On the left side is reported the evolution in time along the light propagation direction, <001> for: space charge field (normalized to the bias one), induced refractive index and intensity profile. On the right one, the corresponding transverse profiles at the output face are depicted.

Going back to the second peak origin, if the nonlinearity is not strong enough to keep constant the transverse beam phase all along the propagation distance, then the negative refractive index region can actually separate the residual diffracted light from the main self-confined contribution. As further analysis, it has been verified that this secondary peak is neither introduced by additional interference patterns arising from the used optical components nor by a double reflection inside the sample. Its separation from the main contribution is also related to the temperature, but cannot be eliminated, at least within the used temperature range: 15°C and 25°C. Clearly, this beam configuration ($w_{in} = 19\mu m$) cannot be used to study collisions as it implies the interaction between four beams having different strengths.

Consequently, because of the electron-hole competition process and self-confinement dynamics, the refractive index variation is asymmetric with respect to the beam centre (fig. 4.7 (c)-(d)) and might be the "sparkle" for light bending. Also bending is mediated by the temperature/light intensity couple, but this aspect is still under investigation.

4.7 Collisions between co-propagating parallel beams

In the previous section, the best self-trapping conditions for one beam have been found: waist $w_{in} = 25\mu m$ and I=0.77 W cm^{-2} for a stabilized temperature of 20°C, condition (A) in fig. 4.4. Now, the simultaneous injection of two parallel and identical beams (light intensity and input waist) and the relative phase influence on their propagation is studied when the bias electric field ($E_{bias} = 10 kV\,cm^{-1}$) is applied. These interactions are coherent, so the relative phase difference existing between the beams drives them to fuse or repulse each other. At the same time, the relative phase itself represents a critic point for the measurements, as it will be shown further on.

The used laser beam coherence length is about twice the propagation distance inside the sample. Beams will remain coherent all along the whole propagation path and this has been verified by maximizing the interference fringe modulation amplitude in condition of linear diffraction.

If individually injected, the two beams will exhibit exactly the same self-trapping properties, like for example the same amount of bending, but if simultaneously launched, it will not remain the same. As the two beams are injected making them lie along a plane parallel to the bias electric field direction, they will not react to the applied electric field exactly in the same

way. This is consequence of the partial bias field screening that one of the two beams causes, thus slightly modifying self-trapping properties for the second one. Consequently, the relative phase difference cannot remain constant along the whole propagation path. Furthermore, as in this configuration all the generated carriers are driven by the bias field, the amount of screening will change in function of the temperature (electrons) and light intensity (holes) as well.

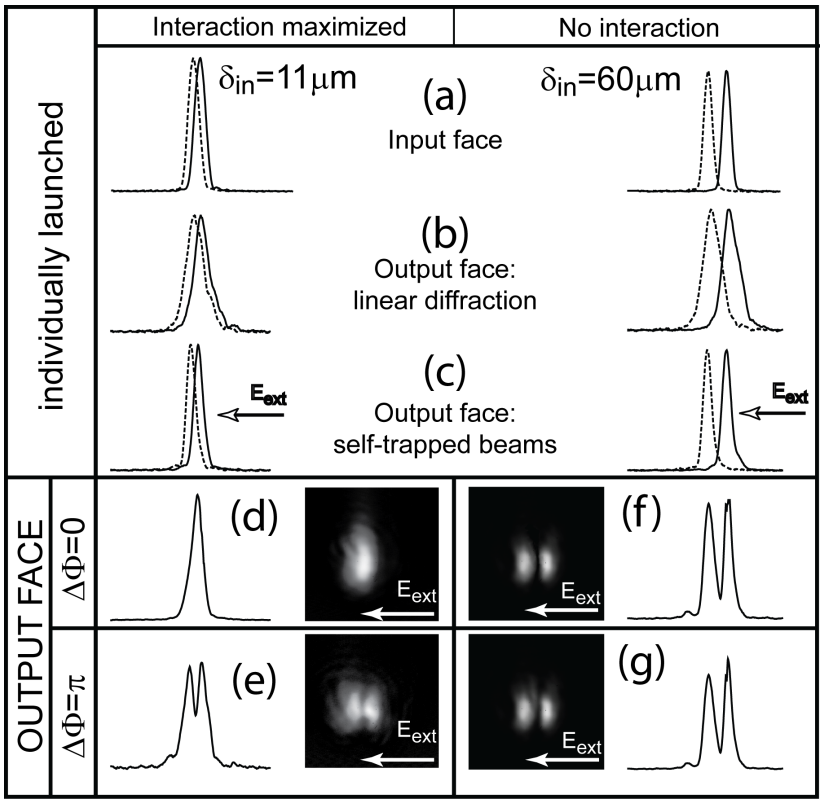

Figure 4.8: Limit interaction cases (maximal and no interaction) for two beams separated by a distance δ_{in}, at T = 20°C and injected with an intensity of 0.77W cm^{-2} each. Profiles are drawn along the $< 001 >$ direction. (a) (b) (c) are relative to the individually injected beams at the input and output face in linear and nonlinear condition ($\text{E}_{\text{bias}} = 10\text{kV cm}^{-1}$). From (d) to (g) the two simultaneously injected beam interaction result is reported in function of the relative phase difference existing between them $\Delta\phi = 0, \pi$.

Experimentally, the typical resulting collision effect is resumed in fig. 4.8. Fusion and repulsion cases fig. 4.8 (d)-(g) are depicted in terms of the two beam transverse profiles along the x axis, with reference to a temperature of 20°C. The collision behaviour corresponds to the beam configuration at the input fig. 4.8 (a) and output fig. 4.8 (b)-(c) faces of the sample. In details, the two limit situations are drawn: maximal interaction, occurring for an input separation of $\delta_{\text{in}} = 11\mu$m, and no interaction at all for $\delta_{\text{in}} \simeq 60\mu$m. The latter situation indicates that the two beams are too far one each other and so they behave like if individually injected, thus confirming the local nature of the photorefractive interaction. The interference induced refractive index variation in-between the beams is negligible in the last case, while is strongly enhanced in the other. The minimum separation value represents the limit for which the interference result can be distinguished in the repulsion case. This is consequence of the destructive interference that has a very wide fringe, ideally infinite for a perfect overlap of the two interacting beams. Both the cases, repulsion and fusion, have been investigated. The parameters that have been taken into account are: beam separation and thus their overlapping degree, light intensity and temperature. The latter is changed by $\pm 5°$ with respect to 20° C.

To perform this analysis, three light intensity values have been chosen in function of the single beam self-focusing efficiency, fig. 4.4: best self-focusing and two points corresponding to a lower and lower efficiency. In the picture fig. 4.4 they are labelled with (A), (B), (C) and the corresponding intensity values are: 0.77 W cm^{-2}, 1.55 W cm^{-2} and 2.32 W cm^{-2}, respectively.

In the following, experimental results for repulsion and fusion will be presented and discussed [199]. At the moment it is not yet possible to give an exhaustive explanation of the involved physical processes because of the lack of a model able to describe the microscopic charge behaviour. In collaboration with University of Besançon, a numerical model is being developed using the following experimental results as reference.

4.7.1 Out of phase ($\Delta\phi = \pi$) beams: repulsion

To describe this process, the parameter "repulsion efficiency" is defined. It represents the ratio between the two beam separation in nonlinear regime and the one in the linear diffraction condition. Repulsion efficiency is plot versus the input separation distance normalized to the input waist, for the three light intensity values. Experimental results for T=20° C are reported

in fig. 4.9 (A)-(B)-(C). In terms of charges and according to the previously described models, the light induced free hole generation rate is thus modified. As expected, in spite of the same input separation for the two

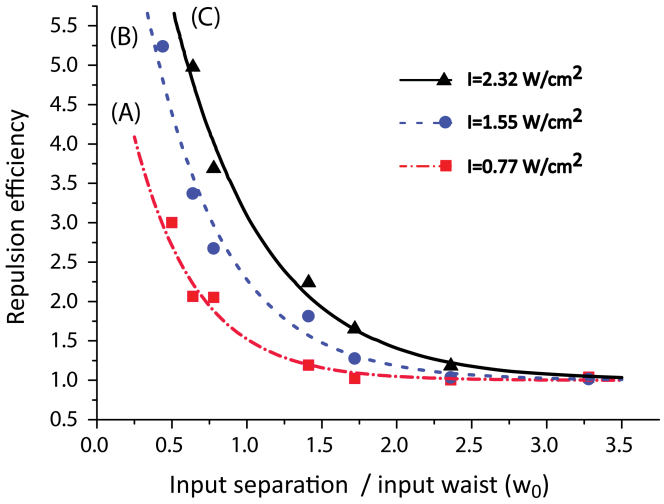

Figure 4.9: The ratio between the two beam separation in nonlinear and linear regime is plot versus the input separation normalized to the single input beam waist. This curve is relative to a temperature T = 20°C and the light intensity values correspond to the (A) (B) and (C) conditions of fig.4.4.

beams, repulsion efficiency is different for the three cases. It decreases from a maximum separation value of about $125\mu m \simeq 5w_{in}$ (for beams separated by $\delta_{in} \simeq 0.5w_{in}$), up to a distance identical to the individually launched beams one. This confirms that this process is strictly bound to the two beams induced refractive index overlapping degree. They stop interacting when separation between the beam centres is about $3w_{in} \simeq 75 \div 80\mu m$. This experimental set of points are found to be better described by an exponential trend than by a function related to the inverse of distance.

Qualitatively, it is found that in correspondence to the same beam relative distance, separation at the output increases moving from (A) to (C) in fig. 4.4. It increases moving from a condition of maximized diffraction compensation to a condition of more and more diffracted beams. A possible explanation for this behaviour can be inferred. As two diffracted beams

share a larger overlapping region than a self-trapped one, the destructive interference can dig a wider negative refractive index region. Furthermore, moving from (A) to (C) also light intensity on the beam tails is stronger, so the interference contrast increases and acts as if a stronger force was induced.

By changing the sample temperature, also the thermally generated electron rate can be modified. The procedure used to find the self-focusing region at 20° C is repeated for T = 15°C and T = 25°C. A variation of only ±5°C is applied to the reference temperature. In fig.4.10, single beam self-focusing behaviour is reproduced for both the cases in comparison to one at T = 20°C and waist values are not normalized. A self-focusing region follows a self-defocusing one and their boundaries change with temperature. Self-confined beam waist, for the three intensity values under investigation (I = 0.77; 1.55; 2.32W cm^{-2}), has been averaged over more measurements to get an high enough accuracy about the crossing points.

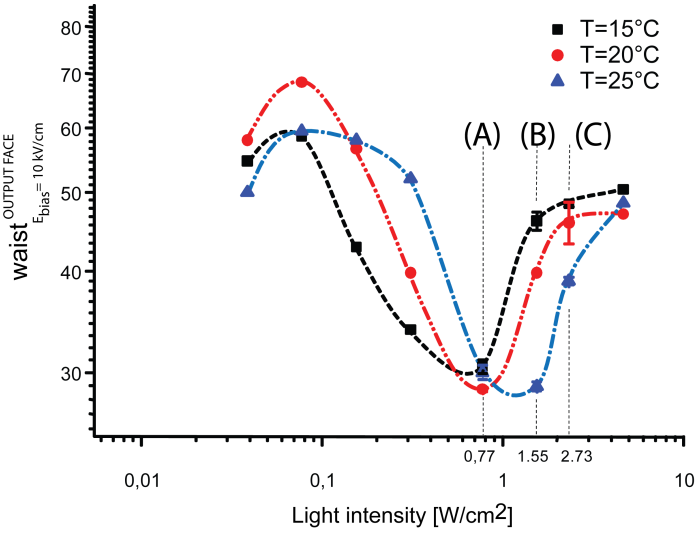

Figure 4.10: Single beam waists in nonlinear regime for T = 15°C, T = 20°C and T = 25°C.

For a temperature of T = 20°C, two repulsing beams exhibit three well distinguished trends and repulsion efficiencies, as in fig.4.9. This is in agreement with the fact that the considered self-focusing efficiencies are almost

equally separated among them: 0.56 in (A), 0.74 in (B) and 0.92 in (C) of fig.4.4.

Repeating the same analysis also for the other two temperatures, a strong correlation between repulsion and single beam self-focusing efficiency can be found. For a temperature of T = 15°C, for example, it might be expected to find a similar trend for repulsion in correspondence to the (B) and (C) conditions in fig.4.10. This as a consequence of the very close single, self-confined, beam waists: 46.1μm in (B) and 48.4μm in (C).

Because of the same reason, such a result should be obtained for the (A) and (B) conditions at T = 25°C. In this case, single beam waists are 30μm in (A) and 28.9μm in (B).

To verify this behaviour, the two beam separation at the output face and in nonlinear regime, is plot versus the one imposed at the input face and in function of light intensity. In this way, the hypothesized trends can be confirmed, fig.4.11 and fig.4.12. In fact, in the considered conditions, an almost perfect overlapping of the corresponding curves is found for all the considered initial separation values.

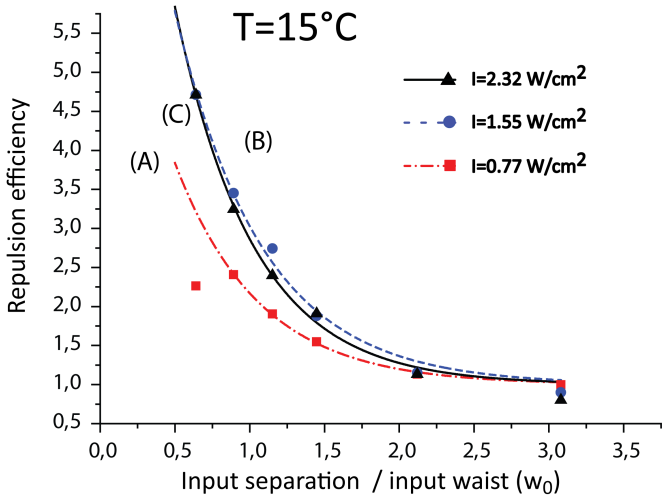

Figure 4.11: Repulsion efficiency for a temperature of T = 15°C in function of the input separation distance normalized to the single input beam waist. Almost complete overlapping for curves corresponding to the (B) and (C) conditions in fig.4.10 for the same temperature.

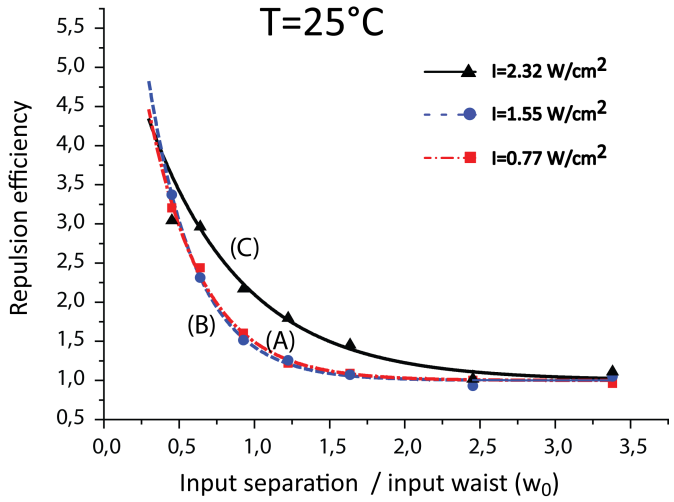

Figure 4.12: Repulsion efficiency for a temperature of T = 25°C in function of the input separation distance normalized to the single input beam waist. Almost complete overlapping for curves corresponding to the (A) and (B) conditions in fig.4.10 for the same temperature..

4.7.2 In-phase ($\Delta\phi = 0$) beams: fusion

When the two beams are in-phase ($\Delta\Phi = 0$) and simultaneously launched, an attraction between them can be forced. The bright fringe appearing in between them increases the local refractive index and the two beam energy can be guided into a unique beam. This resulting light induced structure can realize a Y-junction-like behaviour and so it could be employed as a coupler device.

As done for the case of repulsion, this phenomenon is studied in function of: sample temperature, light intensity and separation distance between the two beams.

The initial phase between them is chosen looking at the input face of the sample and maximizing the light intensity of the bright fringe appearing in the middle.

While the beam fusion has been achieved for all the performed measurements, it is interesting to investigate the final size of the resulting beam.

It is worth remembering that to achieve fusion it is fundamental to avoid beam injection with an angle in-between them. This would be responsible

for the appearing of angular momenta and thus for spiralling.

As it will be demonstrated, fusion depends on many parameters and the performed measurements still present some unclear aspects that must be deepened with further investigations.

As a general comment, it is expected that the local nature of this process limits it to occur only when a substantial beams overlapping is present, thus when each beam can feel the refractive index variation induced by the other. When launched along parallel directions and very close one each other, the induced bright fringe, that is supposed to drive the whole process, is larger than the single beam. Being fusion related to beam superposition, this fringe size is not expected to reduce in an appreciable way till when a critical beam separation is reached.

When the two individually launched self-trapped beams are made interact one-each-other in an in-phase configuration, each of them will bend towards the other one because of the increased refractive index region that is created in the middle. If each soliton is thought like an interacting particle, it can be inferred that, as a consequence of bending, each particle will acquire a transverse momentum, and thus a speed, that will induce an angle in the initially parallel propagation. Such an angle is expected to reduce the fringe dimension, and consequently the resulting collapsed beam waist size. By increasing the relative separation, each "particle" can propagate along a longer distance and thus increase its velocity under the effect of the transverse acceleration. The interacting angle will further increase until a critical separation is reached and so a *limit angle must exist*. Once the threshold separation distance is reached, corresponding to a no more enough beam overlapping and thus corresponding to an attractive force that starts reducing more and more, the final beam dimension should start increasing again.

In fig.4.13 - 4.15, the resulting fused beam waist is plot versus the two beam separation on the input face for the three considered temperature values. Some general trends can be inferred. For an imposed temperature of $T = 15°C$, fig.4.13, the final waist for all the three intensities attains a final value with a saturating trend. It is interesting to note that for the lowest light intensity value $I = 0.77 W\,cm^{-2}$ this trend is opposite to the other two, it increases instead of decreasing. When temperature is increased to $T = 20°C$, fig.4.14, the waist size for $I = 1.55 W\,cm^{-2}$ and $I = 2.73 W\,cm^{-2}$ decreases with the increasing separation up to a minimum value, correspondingly to an input separation of about 1.3 ± 1.4 times the input waist. This

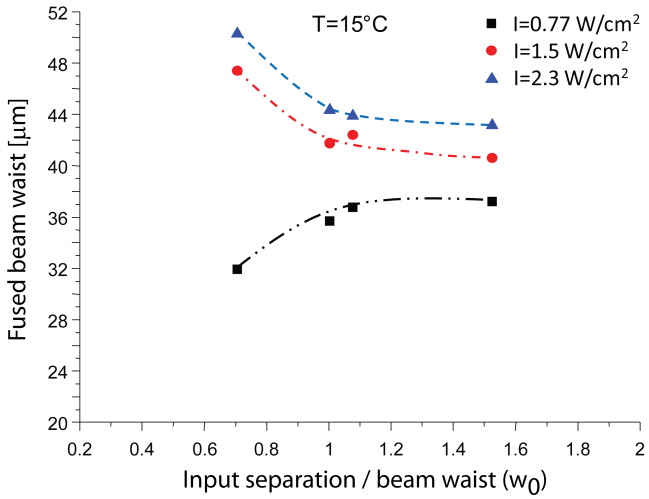

Figure 4.13: Fused beam waist for T = 15°C.

behaviour seems to justify the initial hypothesis about the relationship existing between the attractive force strength and the two beams separation. Conversely, the lower light intensity keeps a decreasing trend. Finally, taking the temperature to the maximum value analysed (T = 25°C), fig.4.15, a similar behaviour exists, no matter the light intensity value. After a monotonic decreasing, a common inversion value is found when the input separation is about 1.6 times the input one. According to the presented whole set of measurements about the fused beam waist, it looks that starting from the condition of maximum overlapping, the fused beam waist should decrease with the increasing of the input separation. This does not happen for T = 15°C and I = 0.77W cm^{-2}, condition for which the waist size increases. This result seems to imply the existence of several regimes in the electron-hole competition process, but the gathered informations are not enough to completely justify this hypothesis; so other measurements must be performed.

Furthermore, a direct comparison with the single beam waist does not fit the presented experimental results. This can be addressed to the in-phase sum of the two interacting electric fields. The additional term introduced by the constructive interference change the expected ratio electrons/holes and the thus the expected photorefractive response.

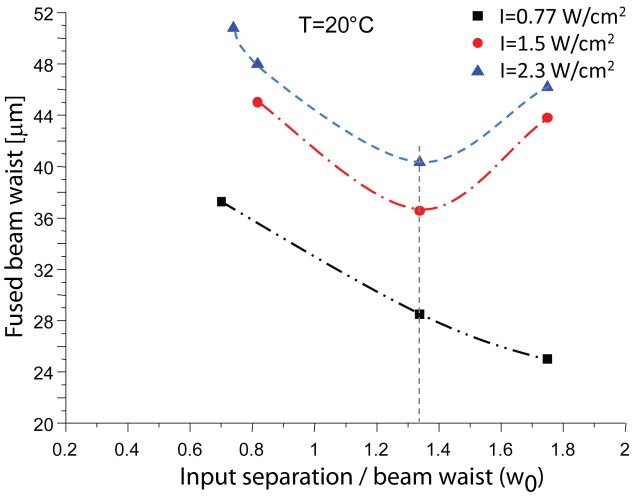

Figure 4.14: Fused beam waist for T = 20°C.

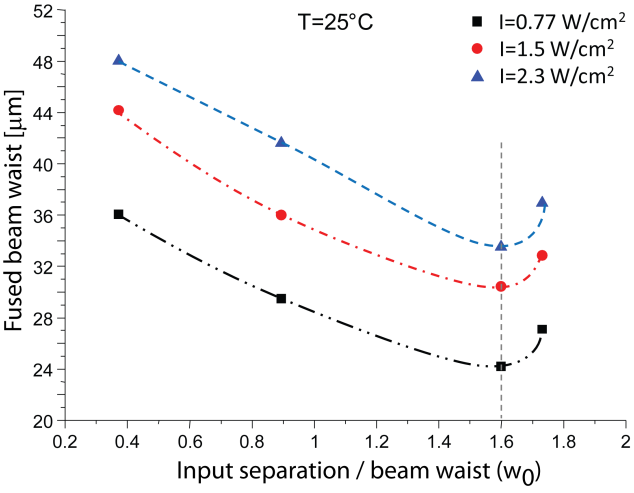

Figure 4.15: Fused beam waist for T = 25°C.

Conclusions

This thesis has been developed with the final aim of realizing an all-optical circuit having improved performances with respect to an electronic one. Solutions for interconnections, sources and an elaborating circuit (a switcher or a coupler) have been proposed. As a novelty element, nonlinear optics has been used to overpass all the limitations that the common technology offers when writing integrated optical interconnections (waveguides). In details, the physic phenomena originating bright photorefractive solitons and in turn photorefractive waveguides have been employed. In this way, the whole bulk became accessible for waveguiding with structures of reduced propagation losses. Soliton waveguiding advantages have been overworked by a proper choice of the photorefractive material: lithium niobate and iron doped indium phosphide. The first, owns a very high relaxation time thus allowing a stable guide even without having fixed it. The second instead, has a very short (micro-milliseconds) one thus allowing a dynamical waveguide reconfiguration.

Solitonic waveguides as optical 3D interconnections Whatever the aim, a good interconnection must grant that the signal transported inside it arrives to the endpoint keeping all its original properties. Because of this, at the very beginning of this thesis, great care has been devoted to create solitonic waveguides that resulted as robust as possible. The work described in this chapter takes into account also all the experimental measurements that I carried out during my master degree thesis where the influence of light intensity and wavelength in photorefractive solitons formation has been analysed in nominally undoped lithium niobate. To complete this work, the influence of light polarization on waveguide formation has been investigated in function of light propagation direction (so material anisotropy). The important result that arose from these measurements, is the higher space

charge field that an ordinary polarized light in the visible region can induce in the material with respect to an extraordinary one. Paying the price of a longer time required to write a waveguide, this configuration provides structures that efficiently trap the light injected inside them. This is a new result that has been explained also numerically by reducing the photovoltaic field contribution when an ordinary polarized light interacts with the lattice. Thus, it is provided the confirmation that this field contribution is less strong than the one along the $\hat{c}$ axis but not negligible; the tensorial nature of the photovoltaic field is demonstrated to play a role.

Solitonic waveguide-based active devices in lithium niobate The extremely low losses and the real 3D character of solitonic waveguides provide very favourable properties to realize an integrated waveguide lasing device. Nowadays technology requires infrared sources working in the third window for telecommunications and if lithium niobate is doped with erbium ions, a luminescence emission can be obtained exactly in this band, at $\lambda = 1530\text{nm}$. The self-confined nature of this waveguides makes it possible to have a constant emission all along the propagation path for the pump beam and in association to the low losses, it is possible to obtain lasing from a proper resonant cavity. As this doping element was never investigated before for the realization of spatial solitons, a characterization of its concentration influence in lithium niobate photorefractive properties (electro-optic coefficient r_{33}, photovoltaic field E_{PV} and self-trapping) has been performed. The injected radiation is not resonant with erbium absorption frequencies. All the parameters resulted influenced by this ions incorporation and a critical value has been found for $\rho_{Er} = 0.3\text{mol}\%$: a trend change for r_{33}, a minimum for the photovoltaic field and the fastest soliton formation time. As further prove for this measurement quality, all the final beam waists have been found to follow a single trend in function of the refractive index constrast calculated with the previously exerimentally determined parameters. A model that well explains changes in the investigated photorefractive parameters has been developped in function of doping concentration that can be considered small and thus justify the substitutional incorporation rule for erbium in lithium sites. As next step, the multistep absorption of a radiation, now resonant with an erbium absorption line, is demonstrated to be able to write a waveguide by means of the incoherent luminescence emitted by erbium ions. This luminescence acts both as background illu-

mination and waveguide writing beam. From numerical simulation, it has been seen that the pump beam and the generated luminescence one are quite well overlapped and that luminescence tails cover a wide region around the pump beam. This justify the high stability and bending absence in the formed waveguide. It is important to remark that in this way, a bending free waveguide for pump beam and the lasing candidate one, can be written at the same time. Finally, numerical simulations about population inversion and optical power requirement in function of the waveguide waist have been performed. Consequently, resonators have been built for the involved frequencies, but this aspect is still under investigations.

Second Harmonic Generation and solitonic waveguides The main aim of this research activity is the realization of an integrated source operating in the blue region. Taking advantage of self-diffraction compensation that a solitonic waveguide offers it is possible to optimize and make constant the second harmonic generation of a near infrared (fundamental) beam inside it. This investigation has been led on nominally undoped samples but in regime of extremely short (femtoseconds) duration light pulses. Different aspects have been investigated. Firstly, the existence of a second harmonic generated signal is demonstrated for an interaction type ee-e which is characterized by a huge phase mismatch and thus very disadvantaged. Then, the possibility of using this seed to write a waveguide in which also the fundamental beam can propagate undiffracted has been exploited, verifying the interplay between the quadratic and photorefractive effect. Finally, physical properties of this seed have been investigated in comparison to the fundamental ones.

Many results have been found. Solitonic behaviour can be achieved only in the modelocked regime and the consequent guide can efficiently trap also the fundamental beam. This process has been found to occur in the framework of an ee-e interaction and so, in spite of the huge phase mismatch that characterize it, it is possible to take advantage of the highest nonlinear coefficient offered by lithium niobate. Then, the nature of the second harmonic pulses has been studied, demonstrating that for each fundamental pulse, two second harmonic contributions are generated. They are not identical, one propagates experiencing the proper material dispersion law, while the other propagates exactly along the direction of the fundamental beam. Thus, in spite of the different wavelength of the two pulses; they feel the same refrac-

tive index. It has been demonstrated that these two pulses are locked both in terms of phase and group velocities. As expected, the photorefractive self-trapping for these two pulses has provided peculiar results. In fact a spatial diffraction compensated structure has been achieved, but the beams propagating inside are locked in time so they give rise to a "simulton". According to the injected power, different regimes have been found: twin-state propagation and filamentation. In a twin-state propagation, locked pulses self-trap as well as the unlocked one, they attract one each other but they never collapse. In the filamentation regime, single pulse identity is lost as they separates in multiple blue contributions and each of them generates a waveguide for the fundamental beam.

Photorefractive interactions in InP:Fe for all-optical telecommunication devices The principle of all-optical information processing has been investigated also by studying the interaction between coherent solitonic beams. Thanks to the high speed of space charge field building up, indium phosphide is a good candidate to realize waveguiding structures that can be quickly reconfigured in an all-optical way. The two beams have been forced to fuse (creating a Y junction) or repel one each other (so increasing their initial separation) simply changing their relative phase and thus the interference in-between them. This behaviour has been characterized in function of the relative distance between the beams and both the parameters that strongly influence photorefractivity inside it: light intensity and temperature. While other measurements and investigations are still necessary, promising results have been obtained.

Perspectives The realization of integrated photonic circuits based on solitonic waveguides seems indeed very promising. The results obtained during my PhD program opened new perspectives and investigations in different domains. The first, short-term, expectation is the analysis of permanent fixing of solitonic waveguides and consequently of solitonic circuits in lithium niobate. In fact we have seen that once formed, a solitonic waveguide can be used for long time thanks to the ultra long relaxation time of lithium niobate. In the laboratory a good efficiency of solitonic waveguides has been recorded after up to several months after writing. But for real commercial applications permanent structures must be obtained, capable to receive no-modifications with their use. For this reason permanent fixing of realized

guiding structures is indeed a challenging perspective that must be investigated in deep. Several techniques have been proposed in literature, like thermal or high-voltage treatments of the modified substrates, or the using of very high-intensity laser beams during the writing procedure. All these techniques will be compared in order to identify the best protocol to permanently fix the realized circuits. A second, short-term, expectation regards the optimization of the proposed devices. In fact during my PhD work I have started new devices, like the laser integrated inside a soliton waveguide, like a frequency converter or a signal processor via soliton interaction. All these devices need some further activities to reach an evolution level high enough to guaranty future commercial applications. A medium-term perspective can be identified in the capability of integrate together different technologies and materials according to the processing level that is needed. More specifically, I have shown that we might use lithium niobate substrates or indium phosphide ones depending on application: in lithium niobate we can realize permanent devices which might be externally modulated by means of the electro-optic effect. Thus, lithium niobate is indeed an excellent material to provide electro-optic devices. But its slow relaxation does not allow to realize all-optical and ultrafast devices: for this reason a much faster medium must be used, like for example indium phosphide. Can these different materials be integrated together to perform complex functions? Clearly the processing protocol would remain the propagation of spatial solitons. But to unify the same protocol within different material supports is indeed a challenging problem that, if solved, will push the activities and applications towards a complete all-optical circuit based on soliton technology. So, finally the long-term perspective is the realization of "complete" all-optical circuits. I have considered here different aspects of the integration, like light sources, frequency conversion, parallel and sequential interconnections and, last but not least, single-bit optical processing. Let's say that all such aspects have been considered from the "academic" point of view. I have investigated the physics of such devices and I have provided their experimental evidence. A big but intriguing challenge is their integration together in a complete all-optical processor. Since long time ago the prospective of an optical computing was pursuit with many efforts, even if real circuits never came out. Hopefully the soliton protocol could play the game and complete integrated processing circuits can be realized. Will they be all-optical or electro-optical? It is not clear at the moment, but probably a combination of the two would guaranty a better capability of performing

operations. In fact, as Latins were saying "IN MEDIO STAT VIRTUS"

Research activities out of the main thesis topic

During my PhD I collaborated to other research activities which are not directly related to spatial solitons and because of this corresponding published papers are just attached at the thesis end. They are related to the measurement of the Kerr refractive index in gallium nitride (GaN) and of the nonlinear abrsorption in zinc-phthalocyanines using the EZ-scan and Z-scan techniques respectively and have titles:

1. Measurement of pure Kerr nonlinearity in GaN thin films at 800nm by means of eclipsing Z-scan experiments. [200]

   Abstract:
   We report the measurement of Kerr nonlinearity of thin films of GaN by using the eclipsing Z-scan technique. The measurement was performed using 100 fs pulses at 800 nm.
   We measured a pure refractive signal, whose associated nonlinear Kerr coefficient was $n_2 = (-7.3 \pm 0.4) \times 10^{-14}\,cm^2\,W^{-1}$

2. Nonlinear optical absorption of zinc-phthalocyanines in polymeric matrix. [201]

   Abstract:
   We realized and investigated films of zinc - phtalocyanines into poly (methylmethacrylate) (PMMA) for optical limiting applications. The ratio by weight of the compound to the host polymer was 0.083% *and* 0.15%. *Linear optical characterization of films, performed by spectrophotometry, show a low degree of molecular aggregation of zinc-phtalocyanines in the polymeric matrix. Two different type of nonlinear optical investigation were performed separately on the obtained*

films. Measurements of nonlinear transmission were carried out using a ns Nd:Yag laser followed by OPO (532 nm) and a nonlinear response was observed. From the experimental data, the nonlinear absorption coefficient b was retrieved and found to be 29 and 43 cm/GW, respectively. The measurements of β was also performed via the z-scan technique on the same films, using 100 fs pulses at 800 nm. At this wavelength, the nonlinear absorption coefficient was evaluated to be 0.40 and 0.23 cm/GW.

List of Figures

Bibliography

[1] S. Fries, P. Hertel, and H. P. Menzler. Extraordinary versus ordinary refractive index change in planar $LiNBO_3$: Ti waveguides. *Phys. stat. sol. (a)*, 108:449–455, 1988.

[2] R. J. Holmes and D. M. Smyth. Titanium diffusion into $LiNbO_3$ as a function of stoichiometry. *J. Appl. Phys.*, 55:3531–, 1984.

[3] J. L. Jackel, C. E. Rice, and J. J. Veselka. Proton exchange in $LiNbO_3$. *Ferroelectrics*, 50:165–170, 1983.

[4] S. Mailis anc C. Riziotis, I. T. Wellington, P. G. R. Smith, C. B. E. Gawith, and R. W. Eason. Direct ultraviolet writing of channel waveguides in congruent lithium niobate single crystals. *Opt. Lett.*, 28:1433–1435, 2003.

[5] P. Ganguly, C. L. Sones, Y. Ying, H. Steigerwald, K. Buse, E. Soergel, R. W. Eason, and S. Mailis. Determination of refractive indices from the mode profiles of uv-written channel waveguides in $LiNbO_3$ - crystals for optimization of writing conditions. *J. Lightwave Technol.*, 27:3490–3497, 2009.

[6] R. Osellame, S. Taccheo, M. Marangoni, R. Ramponi, and P. LaPorta. Femtosecond writing of active optical waveguides with astigatically shaped beams. *J. Opt. Soc. Am. B*, 20:1559–1567, 2003.

[7] K. Minoshima, A. M. Kowalevicz, I. Hartl, E. P. Ippen, and J. G. Fujimoto. Photonic device fabrication in glass by use of nonlinear material processing with a femtosecond laser oscillator. *Opt. Lett.*, 26:1516–1518, 2001.

[8] M. Shih, P. Leach, M. Segev, M. H. Garrett, G. Salamo, and G. C. Valley. Two-dimensional steady-state photorefractive screening solitons. *Opt. Lett.*, 21:324–326, 1996.

[9] E. Fazio, F. Renzi, R. Rinaldi, M. Bertolotti, M. Chauvet, W. Ramadan, A. Petris, and V. I. Vlad. Screening-photovoltaic bright solitons in lithium niobate and associated single-mode waveguides. *Applied Physics Letters*, 85:2193–2195, 2004.

[10] E. Delre, M. Tamburrini, M. Segev, E. Rafaeli, and A. J. Agranat. Two-dimensional photorefractive spatial solitons in centrosymmetric paraelectric potasium-lithium-tantalate-niobate. *Appl. Phys. Lett.*, 73:16–18, 1998.

[11] S. Lan, Ming feng Shih, and M. Segev. Self-trapping of one-dimensional and two-dimensional optical beams and induced waveguides in photorefractive $KNbO_3$. *Opt. Lett.*, 22:1467–1469, 1997.

[12] J. A. Andrade-Lucio, M. D. Iturbe-Castillo, P. A. Marquez-aguilar, and R. Ramos-Garcia. Self-focusing in photorefractive $BaTiO_3$ crystal under external dc electric field. *Opt. Quant. Electron.*, 30:829–834, 1998.

[13] M. Chauvet, S. A. Hawkins, G. J. Salamo, M. Segev, D. F. Bliss, and G. Bryant. Self-trapping of two-dimensional optical beams and light induced waveguiding in photorefractive InP at telecommunication wavelengths. *Appl. Phys. Lett.*, 70:2499–2501, 1997.

[14] D. Wolfersberger, N. Khelfaoui, C. Dan, N. Fressengeas, and H. Leblond. Fast photorefractive self-focusing in InP:Fe semiconductor at infrared wavelengths. *Appl. Phys. Lett.*, 92:021106 1–3, 2008.

[15] T. Schwartz, Y. Ganor, T. Carmon, R. Uzdin, S. Shwartz, M. Segev, and U. El-Hanany. Phorefractive solitons and light-induced resonance control in semiconductor CdZnTe. *Opt. Lett.*, 27:1229, 2002.

[16] J. S. Aitchinson, A. M. Weiner, Y. Silberberg, M. K. Oliver, J. L: Jackel, D. E. Leaird, E. M. Vogel, and P. W. E. Smith. Observation of spatial optical solitons in a nonlinear glass waveguide. *Opt. Lett.*, 15:471–473, 1990.

[17] A. Barthelemy, S. Maneuf, and C. Froehly. Propagation soliton et auto-confinement de faisceaux laser par nonlinearité optique de Kerr. *Opt. Commun.*, 55:201–206, 1985.

[18] M. Hercher. Laser-induced damage in transparent media. *J. Opt. Soc. Am.*, 54:563–, 1964.

[19] P. L. Kelley. Self-focusing of optical beams. *Phys. Rev. Lett.*, 15:1005–1008, 1965.

[20] Pochi yeh. *Introduction to photorefractive nonlinear optics.* Wiley series in pure and applied optics, J.W. Goodman Editor, 1993.

[21] T. Brabec, Ch. Spielmann, P. F. Curley, and F. Krausz. Kerr lens mode locking. *Optics letters*, 17:1292–1294, 1992.

[22] J. Hermann. Theory of kerr-lens mode locking: role of self-focusing and radially varying gain. *J. Opt. Soc. Am. B*, 11:498–512, 1994.

[23] Y. N. Karamzin and P. Sukhorukov. Mutual focusing of high-power light beams in media with quadratic nonlinearity. *Sov. Phys. JETP*, 41:414, 1975.

[24] D. E. Pelinovsky, A. V. Buryak, and Y. S. Kivshar. instability of solitons governed by quadratic nonlinearities. *Phys. Rev. Lett*, 75:591–595, 1995.

[25] W. E. Torruellas, Z. Wang, D. J. Hagan, E. W. Van Stryland, G. I. Stegeman, L. Torner, and C. R. Menyuk. Observation of two-dimensional spatial solitary waves in a quadratic medium. *Phys. Rev. Lett.*, 74:5036–5039, 1995.

[26] R. Schiek, Y. Baek, and G. I. Stegeman. One-dimensional spatial solitary waves due to cascaded second-order nonlinearities in planar waveguides. *Phys. Rev. A*, 53:1138–1141, 1996.

[27] G. Assanto and G. I. Stegeman. Symple physics of quadratic spatial solitons. *Opt. Express*, 10:388–396, 2002.

[28] R. S. Weis and T. K. Gaylord. Lithium niobate: Summary of physical properties and crystal structure. *Appl. Phys. A*, 37:191–203, 1985.

[29] T. Volk and M. Wöhlecke. *Lithium niobate, defects, photorefraction and ferroelectric switching.* Springer, 2008.

[30] M. E. Lines and A. M. Glass. *Principles and applications of ferroelectrics and related materials.* Clarendon Press - Oxford, 1977.

[31] Y. S. Kuzminov. *Lithium niobate crystals.* Cambrige international science, 1999.

[32] J. Czochralski. *Z. Phys. Chem.*, 92:219–221, 1918.

[33] M. Thirumavalavan, S. Sitharaman, S. Ravi, L. Durai, N. L. Jagota, R. C. Narula, and R. Thyagarajan. Growth of large diameter lithium niobate single crystals by Czochralski method. *Ferroelectrics*, 102:15–22, 1990.

[34] K. Buse. www.photonik.uni-bonn.de/papers/talks/080624_buse.pdf.

[35] Y. Furukawa, M. Sato, K. Kitamura, and Y. Yajima. optical resistance and crystal quality of $LiNbO_3$ single crystals with various [Li]/[Nb] ratios. *J. Appl. Phys.*, 72:3250–3254, 1992.

[36] F. Jermann, M. Simon, and E. Krätzig. Photorefractive properties of congruent and stoichiometric lithium niobate at high light intensities. *J. Opt. Soc. Am. B*, 12:2066–2070, 1995.

[37] U. Scharb and K. Betzler. refractive indices of lithium niobate as a function of temperature, wavelength and composition: a generalized fit. *Phys. Rev. B*, 48:15613–15620, 1993.

[38] H. A. Eggert, B. Hecking, and K. Buse. Electrical fixing in near-stoichiometric lithium niobate crystals. *Opt. Lett.*, 29:2476–2478, 2004.

[39] J. Safioui, F. Devaux, and M. Chauvet. Pyroliton: pyroelectric spatial soliton. *Opt. Express*, 17:22209–22216, 2009.

[40] A. Yariv and P. Yeh. *Optical waves in crystals. Propagation and control of laser radiation.* Wiley International, 2003.

[41] A. M. Glass, D. von der Linde, and T. J. Negran. High-voltage bulk photovoltaic effect and the photorefractive process in $LiNbO_3$. *Appl. Phys. Lett.*, 25:233–235, 1974.

[42] V. I. Belinicher, I.F. Kanaev, V. K. Malinovskiĭ, and B. I. Sturman. Theory of photogalvanic effect in ferroelectrics. *Ferroelectrics*, 22:647–648, 1978.

[43] H. G. Festl, P. Hertel, E. Krätzig, and R. von Baltz. Investigations of the photovoltaic tensor in doped $LiNbO_3$. *Phys. Status Solidi (a)*, 113:157–164, 1982.

[44] M. Simon, St Wevering, K. Buse, and E. Krätzig. The bulk photovoltaic effect of photorefractive $LiNbO_3 : Fe$ crystals at high light intensities. *J. Phys. D: Appl. Phys*, 30:144–149, 1997.

[45] K. Buse. Light-induced charge transport processes in photorefractive crystals I: models and experimental methods. *Appl. Phys. B*, 64:273–291, 1997.

[46] F.Jermann and J. Otten. Light induced charge transport in $LiNbO_3 : Fe$ at high light intensities. *J. Opt. Soc. Am. B*, 10:2085–2092, 1993.

[47] M. Segev, B. Crosignani, and A. Yariv. Spatial solitons in photorefractive media. *Phys. Rev. Lett.*, 68:923–926, 1992.

[48] G. C. Duree, Jr. J. L. Shultz, G. J. Salamo, M. Segev, A. Yariv, B. Crosignani, P. Di Porto, E. J. Sharp, and R. R. Neurgaonkar. Observation of self-trapping of an optical beam due to the photorefractive effect. *Phys. Rev. Lett.*, 71:533–536, 1993.

[49] M. Segev, G. C. Valley, B. Crosignani, P. DiPorto, and A. Yariv. Steady-state screening solitons in photorefractive materials with external applied field. *Phys. Rev. Lett.*, 73:3211–3214, 1994.

[50] D. N. Christodoulides and M. I. Carvalho. Bright, dark, and grey spatial soliton states in photorefractive media. *J. Opt. Soc. Am. B*, 12:1628–1633, 1995.

[51] G. C. Valley, M. Segev, B. Crosignani, A. Yariv, M. M. Fejer, and M. C. Bashaw. Dark and bright photovoltaic spatial solitons. *Phys. Rev. A*, 50:R4457–R4460, 1994.

[52] M. Segev, G. C. Valley, M. C. Bashaw, M. Taya, and M. M. Fejer. Photovoltaic spatial solitons. *J. Opt. Soc. Am. B*, 14:1772–1781, 1997.

[53] M. Taya, M. C. Bashaw, M. M. Fejer, M. Segev, and G. C. Valley. Observation of dark photovoltaic spatial solitons. *Phys. Rev. A*, 52:3095–3100, 1995.

[54] M. Taya, M. C. Bashaw, M. M. Fejer, M. Segev, and G. C. Valley. Y junctions arising from dark-soliton propagation in photovoltaic media. *Opt. Lett.*, 21:943–945, 1996.

[55] W. L. She, K. K. Lee, and W. K. Lee. Observation of two-dimensional bright photovoltaic spatial solitons. *Phys. Rev. Lett.*, 83:3182–3185, 1999.

[56] L. Jinsong and L. Keqing. Screening-photovoltaic spatial solitons in biased photovoltaic-photorefractive crystals and their self-deflection. *J. Opt. Soc. Am. B*, 16:550–555, 1999.

[57] L. Keqing, T. Tiantong, and Z. Yanpeng. One-dimensional steady-state spatial solitons in photovoltaic photorefractive materials with an external applied field. *Phys. Rev. A*, 61:053822 1–5, 2000.

[58] A. A. Zozulya and D. Z. Anderson. Propagation of an optical beam in a photorefractive medium in the presence of a photogalvanic nonlinearity or an externally applied electric field. *Phys. Rev. A*, 1995:1520–1531, 51.

[59] M. Chauvet, V. Coda, H. Maillotte, E. Fazio, and G. Salamo. Large self-deflection of soliton beams in $LiNbO_3$. *Opt. Lett.*, 30:1977–1979, 2005.

[60] A. Ashkin, G. B. Boyd, J. M. Dziedzic, R. G. Smith, A. A. Ballman, J. J. Levinstein, and K. Nassau. Optically-induced refractive index inhomogeneities in $LiNbO_3$ and $LiTaO_3$. *Appl. Phys. Lett.*, 9:72–74, 1966.

[61] J. J. Amodei. Electron diffusion effects during hologram recording in crystals. *Appl. Phys. Lett.*, 18:22–24, 1971.

[62] N. V. Kukhtarev, V. B. Markov, S. G. Odulov, M. S. Soskin, and V. L. Vinetskii. Holographic storage in electrooptic crystals. I. steady state. *Ferroelectrics*, 22:949–060, 1979.

[63] N. Fressengeas, J. Maufoy, and K. Kugel. Temporal behavior of bidimensional photorefractive bright spatial solitons. *Phys. Rev. E*, 54:6866–6875, 1996.

[64] N. Fressengeas, D. Wolfersberger, J. Maufoy, and G. Kugel. Build up mechanism of (1+1)-dimensional photorefractive bright spatial quasi-steady-state and screening solitons. *Opt. Commun.*, 145:393–399, 1998.

[65] M. Chauvet. Temporal analysis of open-circuit dark photovoltaic spatial solitons. *J. Opt. Soc. Am. B*, 20:2515–2522, 2003.

[66] E. Fazio, M. Chauvet, V. I. Vlad, A. Petris, F. Pettazzi, V. Coda, and M. Alonzo. *Ferroelectric crystals for photonics applications: Including nanoscale fabrication and characterization techniques.* Series in material science. Springer, 2009.

[67] K. Kos, H. Meng, G. Salamo, M. Shih, M. Segev, and G. C. Valley. One-dimensional steady-state photorefractive screening soliton. *Phys. Rev. E*, 53:R4330–R4333, 1996.

[68] M. Alonzo. Master degree thesis: "solitoni ottici spaziali ad alta intensità in niobato di litio". *Sapienza, Universitá di Roma*, 2005.

[69] Crystal Technology. *http://www.crystaltechnology.com.*

[70] J. Safioui, M. Chauvet, F. Devaux, V. Coda, F. Pettazzi, M. Alonzo, and E. Fazio. Polarization and configuration dependence of beam self-focusing in photorefractive $LiNbO_3$. *J. Opt. Soc. Am. B*, 26:487–492, 2009.

[71] J. Safioui, M. Chauvet, F. Devaux, V. Coda, F. Pettazzi, M. Alonzo, and E: Fazio. Impact of tensorial nature of the electro-optic effect on vortex beam propagation in photorefractive media. *Opt. Express*, 16:7134–7141, 2008.

[72] F. Devaux, V. Coda, M. Chauvet, and R. Passier. New time-dependent photorefractive three dimensional model: application to self-trapped beam with large bending. *J. Opt. Soc. Am. B*, 25:1081–1086, 2008.

[73] R. Passier, F. Devaux, and M. Chauvet. Impact of tensorial nature of the electro-optic effect on vortex beam propagation in photorefractive media. *Opt. Express*, 16:7134–7141, 2008.

[74] B. Sturmann and V. I. Fridkin. *The photovoltaic and photorefractive effects in noncentrosymmetric materials.* Gordon and Breach Science Publishers, 1992.

[75] K. Hsu, C. M. Miller, J. T. Kringlebotn, E. M. Taylor, J. Townsend, and David N. Payne. Single-mode tunable erbium:ytterbium fiber Fabry-Perot microlaser. *Opt. Lett.*, 19:886–888, 1994.

[76] K. Hsu, C. M. Miller, J. T. Kringlebotn, and D. N. Payne. Continuous and discrete wavelength tuning in Er:Yb fiber Fabry-Perot lasers. *Opt. Lett.*, 20:377–379, 1995.

[77] J. L. Zyskind, J. W. Sulhoff, J. Stone, D. J. DiGiovanni, L. W. Stulz, H. M. Presby, A. Piccirilli, and P.E. Pramayon. Electrically tunable, diode pumped erbium-doped fibre ring laser with fibre Fabry-Perot etalon. *Electron. Lett.*, 27:1950–1951, 1991.

[78] G. A. Ball and W. W. Morey. Continuously tunable single-mode erbium fiber laser. *Opt. Lett.*, 17:420–422, 1992.

[79] R. Brinkmann, W. Sohler, and H. Suche. Continuous-wave erbium-diffused $LiNbO_3$ waveguide laser. *Elect. Lett.*, 27:415–417, 1991.

[80] P. Becker, R. Brinkmann, M. Dinand, W. Sohler, and H. Suche. Er-diffused $Ti : LiNbO_3$ waveguide laser of 1563 and 1576 nm emission wavelengths. *Appl. Phys. Lett.*, 61:1257–1259, 1992.

[81] H. Suche, L. Baumann, D. Hiller, and W. Sohler. Modelocked $Er : Ti : LiNbO_3$ waveguide laser. *Elect. Letters*, 29:1111–1112, 1993.

[82] Söchtig, R. Groβ, I. Baumann, W. Sohler, H. Schütz, and R. Widmer. DBR waveguide laser in erbium-diffusion-doped $LiNbO_3$. *Elect. Letters*, 31:551–552, 1995.

[83] Ch. Becker, A. Greiner, Th. Oesselke, A. Pape, W. Sohler, and H.Suche. Integrated optical $Ti : Er : LiNbO_3$ distributed bragg reflector laser with a fixed photorefractive grating. *Opt. Lett.*, 23:1194–1196, 1998.

[84] K. Schäfer, I. Baumann, W. Sohler, H. Suche, and S. Westenhöfer. Diode-pumped and packaged acoustooptically tunable Ti:Er:$LiNbO_3$ waveguide laser of wide tuning range. *IEEE J. Quantum Elect.*, 33:1636–1641, 1997.

[85] E. Fazio, M. Alonzo, F. Devaux, A. Toncelli, N. Argiolas, M. Bazzan, C. Sada, and M. Chauvet. Luminescence-induced photorefractive spatial solitons. *Appl. Phys. Lett.*, 96:091107 1–3, 2010.

[86] T. Fujiwara, M. Takahashi, M. Ohama, A. J. Ikushima, and Y. Furukawa nad K. Kitamura. Comparison of electro-optic effect between stoichiometric and congruent $LiNbO_3$. *Elect. Lett.*, 35:499–501, 1999.

[87] S. M. Kostritskii and O. G. Sevostyanov. Influence of intrinsic defects on light-induced changes in the refractive index of lithium niobate crystals. *Appl. Phys. B*, 65:527–533, 1997.

[88] X. He and D. Xue. Doping mechanism of optical damage resistant ions in lithium niobate crystals. *Opt. Commun.*, 265:537–541, 2006.

[89] M. Imlau. Defects and photorefraction: A relation with mutual benefit. *Phys. Stat. Sol. (a)*, 3:642–652, 2007.

[90] F. Abdi, M. Aillerie, M. Fontana, P. Bourson, T. Volk, B. Maximov, S. Sulyanov, N. Rubinina, and M. Wöhlecke. Influence of Zn doping on electrooptical properties and structure parameters of lithium niobate crystals. *Appl. Phys. B*, 68:795–799, 1999.

[91] K. Chah, M. D. Fontana, M. Aillerie, P. Bourson, and G. Malovichko. Electro-optic properties in undoped and Cr-doped $LiNbO_3$ crystals. *Appl. Phys. B*, 67:65–71, 1998.

[92] K. Chah, M. Aillerie, M. D. Fontana, and G. Malovichko. Electro-optic properties in Fe-doped $LiNbO_3$ crystals as a function of composition. *Opt. Commun.*, 176:261–265, 2000.

[93] Th. Gog, M. Griebenow, and G. Materlik. X-ray standing wave determination of the lattice location of er diffused into $LiNbO_3$. *Phys. Lett. A*, 181:417–420, 1993.

[94] I. Baumann, S. Bosso, R. Brinkmann, R. Corsini, M. Dinand, A. Greiner, K. Schäfer, J. Söchtig, W. Sohler, H. Suche, and R. Wessel. Er-doped integrated optical devices in $LiNbO_3$. *IEEE J. Sel. Top. Quant.*, 2:355–366, 1996.

[95] L. Rebouta, M. F. da Silva, J. C. Soares, D. Serrano, E. Diéguez, F. Agulló-Lopez, and J. Tornero. Nonaxial sites for Er in $LiNbO_3$. *Appl. Phys. Lett.*, 70:1070–1072, 1997.

[96] T. Bodziony and S. M. Kaczmarek. EPR study of low simmetry Er centers in congruent lithium niobate. *Phys. Stat. Sol. (b)*, 245:998–1002, 2008.

[97] S. M. Kaczmarek and T. Bodziony. Low symmetry centers in $LiNbO_3$ doped with Yb and Er. *J. Non-cryst. solids*, 354:4202–4210, 2008.

[98] P. Nekvindova, J. Cervena, P. Capek, A. Mackova, V. Perina, J. Schrofel, and J. Spirkova. Features of APE waveguides in different $Er : LiNbO_3$ and $(Er + Yb) : LiNbO_3$ cuts: electrooptical coefficient r_{33}. *Opt. Mat.*, 24:527–535, 2003.

[99] A. Petris, S. Heidari Bateni, V. I. Vlad, M. Alonzo, F. Pettazzi, N. Argiolas, M. Bazzan, C. Sada, D. Wolfersberger, and E. Fazio. The r_{33} electro-optic coefficient of $Er : LiNbO_3$. *J. Opt.*, 12:015205 1–5, 2010.

[100] P. Delaye and G. Roosen. Measuring low amplitude periodical pulse shift without set-up stabilization: effect characterization. *Opt. Commun.*, 214:199–206, 2002.

[101] M. Alonzo, F. Pettazzi, M. Bazzan, N. Argiolas, M. V. Ciampolillo, S. H. Batheni, C. Sada, D. Wolfersberger, A. Petris, V. I. Vlad, and E. Fazio. Self-confined beams in erbium-doped lithium niobate. *J. Opt.*, 12:015206 1–6, 2010.

[102] M. Nippus and R. Claus. The influence of photorefractive index change on raman scattering intensities in $LiNbO_3$. *Z. Naturforschung*, 33a:924–933, 1978.

[103] C. Anastassiou, Ming feng Shih, M. Mitchell, Z. Chen, and M. Segev. Optically induced photovoltaic self-defocusing-to-self-focusing transition. *Opt. Lett.*, 23:924–926, 1998.

[104] A. R. Denton and N. W. Ashcroft. Vegard's law. *Phys. Rev. A*, 43:3161–3164, 1991.

[105] S. C. Abrahams and P. Marsh. Defect structure dependence on composition in lithium niobate. *Acta Crystallogr., Sect. B: Struct. Sci.*, 42:61, 1986.

[106] P. Lerner, C. Legras, and J.P. Dumas. Stoechiométrie des monocristaux de métaniobate de lithium. *J. Cryst. Growth*, 3:231, 1968.

[107] N. Iyi, K. Kitamura, F. Izumi, J.K. Yamamoto, T. Hayashi, H. Asano, and S. Kimura. Comparative study of defect structures in lithium niobate with different compositions. *J. Solid State Chem.*, 101:340, 1992.

[108] N. Zotov, H. Boysen, F. Frey, T. Metzger, and E. Born. Cation substitution models of congruent $LiNbO_3$ investigated by X-ray and neutron powder diffraction. *J. Phys. Chem. Solids*, 55:145, 1994.

[109] A. P. Wilkinson, A. K. Cheetham, and R. H. Jarman. The defect structure of congruently melting lithium niobate. *J. Appl. Phys.*, 74:3080–3083, 1993.

[110] G. Malovichko, V. Grachev, and O. Schirmer. Intercorrelation of intrinsic and extrinsic defects - congruent, stoichiometric, and regularly ordered lithium niobate. *Appl. Phys. B*, 68:785–793, 1999.

[111] F. Abdi, M. D. Fontana, M. Aillerie, and P. Bourson. Coexistence of Li and Nb vacancies in the defect structure of pure $LiNbO_3$ and its relationship to optical properties. *Appl. Phys. A - Mater*, 83:427–434, 2006.

[112] G. G. DeLeo, J. L. Dobson, M. F. Masters, and L. H. Bonjack. Electronic structure of an oxygen vacancy in lithium niobate. *Phys. Rev. B*, 37:8394–8400, 1988.

[113] G.E. Peterson and A. Carnevale. ^{93}Nb NMR linewidths in nonstoichiometric lithium niobate. *J. Chem. Phys.*, 56:4848, 1972.

[114] H. Fay, W. J. Alford, and H. M. Dess. Dependence of second harmonic phase-matching temperature in lithium niobate crystals on melt composition. *Appl. Phys. Lett.*, 12:89–92, 1968.

[115] R. S. Quimby. Output saturation in 980-nm pumped erbium-doped fiber amplifier. *Appl. Optics*, 30:2546–2552, 1991.

[116] J. Amin, B. Dussardier, T. Schweizer, and M. Hempstead. Spectroscopic analysis of Er^{3+} transitions in lithium niobate. *J. Lumin.*, 69:17–26, 1996.

[117] M. Mitchell, Z. Chen, M. Shih, and M. Segev. Self-trapping of partially spatially incoherent light. *Phys. Rev. Lett.*, 77:490–493, 1996.

[118] M. Mitchell and M. Segev. Self-trapping of incoherent white light. *Nature*, 387:880–883, 1997.

[119] D. L. Veasey, J. M. Gary, J. Amin, and J. A. Aust. Time-dependent modeling of erbium-doped waveguide lasers in lithium niobate pumped at 980 and 1480nm. *IEEE J Qunatum Elect*, 33:1647–1662, 1997.

[120] S. Yamaga. Epitaxial ZnS MπS blue light emitting diode fabricated on n^+-GaAs by low-pressure metalorganic vapor phase epitaxy. *Japanese Journal of Applied Physics*, 30:437–441, 1991.

[121] L.C. Chao and A.J. Steckl. CW blue-green light emission from GaN and SiC by sum-frequency generation and second harmonic generation. *J. Electron. Mater.*, 29:1059–1062, 2000.

[122] I. Harrison, S. V. Novikov, T. Li, R. P. Campion, C. R. Staddon, C. S. Davis, Y. Liao, A. J. Winser, and C. T. Foxon. On the origin of blue emission from As-doped GaN. *Phys. Stat. Sol. (b)*, 228:213–217, 2001.

[123] Crystal Technology. Periodically poled lithium niobate (PPLN). *http://www.crystaltechnology.com.*

[124] E. J. Lim, M. M. Fejer, R. L. Byer, and W. J. Kozlovsky. Blue light generation by frequency doubling in periodically poled lithium niobate channel waveguide. *Elect. Lett.*, 25:731–732, 1989.

[125] G. W. Ross, M. Pollnau, P. G. R. Smith, W. A. Clarkson, P. E. Britton, and D. C. Hanna. Generation of high power blue light in periodically poled $LiNbO_3$. *Opt. Lett.*, 23:171–173, 1998.

[126] Y. Chen, R. Wu, X. Zeng, Y. Xia, and X. Chen. Type I quasi-phase-matched blue second harmonic generation with different polarizations in periodically poled $LiNbO_3$. *Opt. Laser Technol.*, 38:19–22, 2006.

[127] M. M. Fejer, G. A. Magel, D. H. Jundt, and R. L. Byer. Quasi-phase-matched second harmonic generation: tuning and tolerances. *IEEE J. Quantum Elect.*, 28:2631–2654, 1992.

[128] V. Gopalan, T. E. Mitchell, Y. Furukawa, and K. Kitamura. The role of nonstoichiometry in 180° domain switching of $LiNbO_3$ crystals. *Appl. Phys. Lett.*, 72:1981–1983, 1998.

[129] D. A. Bryan, R. Gerson, and H. E. Tomachke. Increased optical damage resistance in lithium niobate. *Appl. Phys. Lett.*, 44:847–849, 1984.

[130] S. Lan, Ming feng Shih, G. Mizell, J. A. Giordmaine, Z. Chen, C. Anastassiou, J. Martin, and M. Segev. Second-harmonic generation in waveguides induced by photorefractive spatial solitons. *Opt. Lett.*, 24:1145–1147, 1999.

[131] C. Lou, J. Xu, H. Qiao, X. Zhang, Y.Chen, and Z. Chen. Enhanced second-harmonic generation by means of high-power confinement in a photovoltaic soliton-induced waveguide. *Opt. Lett.*, 29:953–955, 2004.

[132] M. Domenech, R. E. Di Paolo, G. Lifante, and F. Cussó. Blue light by SHG in diode pumped $LiNbO_3$ waveguides. *Phys. Stat. Sol. (a)*, 192:135–138, 2002.

[133] A. Yariv. *Optical electronics in modern communications*. Oxford University press, 1997.

[134] N. Bloembergen. *Nonlinear optics*. World Scientific, 2005.

[135] J. A. Armstrong, N. Bloembergen, J. Ducuing, and P. S. Pershan. Interactions between light waves in a nonlinear dielectric. *Phys. Rev.*, 127:1918–1939, 1962.

[136] S. A. Akhmanov, V. A. Vysloukh, and A. S. Chirkin. Optics of femtosecond laser pulses. *American Institute of Physics, New York*, pages 140–141, 1992.

[137] S. M. Saltiel, K. Koynov, B. Agate, and W. Sibbett. Second-harmonic generation with focused beams under conditions of large group-velocity mismatch. *J. Opt. Soc. Am. B*, 21:591–598, 2004.

[138] N. Bloembergen and P. S. Pershan. Light waves at the boundary of nonlinear media. *Physical Review*, 128:606–622, 1962.

[139] M. Mlejnek, E. M. Wright, J. V. Moloney, and N. Bloembergen. Second harmonic generation of femtosecond pulses at the boundary of a nonlinear dielectric. *Phys. Rev. Lett.*, 83:2934–2937, 1999.

[140] P. D. Maker, R. W. Terhune, M. Nisenoff, and C. M. Savage. Effects of dispersion and focusing of the production of optical harmonics. *Phys. Rev. Lett.*, 8:21–22, 1962.

[141] W. N. Herman and L. M. Hayden. Maker fringes revisited: second harmonic generation from birefringent or absorbing materials. *J. Opt. Soc. Am. B*, 12:416–427, 1995.

[142] N. C. Kothari and X. Carlotti. Transient second harmonic generation: influence of effective group velocity dispersion. *J. Opt. Soc. Am. B*, 5:756–764, 1988.

[143] W. Su, L. Qian, H. Luo, X. Fu, H. Zhu, T. Wang, K. Beckwitt, Y. Chen, and F. Wise. Induced group velocity dispersion in phase matched second-harmonic generation. *J. Opt. Soc. Am. B*, 23:51–55, 2006.

[144] M. Scalora, G. D'aguanno, M. Bloemer, M. Centini, D. de Ceglia, N. Mattiucci, and Y. S. Kivshar. Dynamics of short pulses and phase matched second harmonic generation in negative index materials. *Opt. Express*, 14:4746–4756, 2006.

[145] E. Fazio, F. Pettazzi, M. Centini, M. Chauvet, A. Belardini, M. Alonzo, C. Sibilia, M. Bertolotti, and M. Scalora. Complete spatial and temporal locking in phase-mismatched second-harmonic generation. *Opt. Express*, 17:3141–3147, 2009.

[146] F. Pettazzi, M. Alonzo, M. Centini, A. Petris, V. I. Vlad, M. Chauvet, and E. Fazio. Self-trapping of low energy infrared femtosecond beams in lithium niobate. *Phys. Rev. A*, 76:063818 1–4, 2007.

[147] K. Buse, F. Jermann, and E. Krätzig. Infrared holografic recording in $LiNbO_3$: Fe and $LiNbO_3$: Cu. *Opt. Mater.*, 4:237–240, 1995.

[148] Y. Furukawa, K.Kitamura, A. Alexandrovski, R. K. Route, M. M. Fejer, and G. Foulon. Green induced infrared absorption in MgO doped $LiNbO_3$. *Appl. Phys. Lett.*, 78:1970–1972, 2001.

[149] M. L. Sundheimer, Ch. Bosshard, E. W. Van Stryland, and G. I. Stegeman. Large nonlinear phase modulation in quasi-phase-matched KTP waveguides as a result of cascaded second-order processes. *Opt. Lett.*, 18 (17):1397–1399, 1993.

[150] O. Ilday F, Kale Beckwitt, Yi-Fan Chen, Hyungsik Lim, and Frank W. Wise. Controllable raman-like nonlinearities from nonstationary, cascaded quadratic processes. *J. Opt. Soc. Am. B*, 21 (2):376–383, 2004.

[151] G. I. Stegeman, D. J. Hagan, and L. Torner. $\chi^{(2)}$ cascading phenomena and their applications to all-optical signal processing, mode-locking, pulse compression and solitons. *Optical and Quantum Electronics*, 28:1691–1740, 1996.

[152] G. Assanto and G. I. Stegeman. Simple physics of quadratic spatial solitons. *Opt. Express*, 10:388–396, 2002.

[153] Richard DeSalvo, Ali A. Said, David J. Hagan, Eric W. Van Stryland, and Mansoor Sheik-Bahae. Infrared to ultraviolet measurements of two-photon absorption and n_2 in wide bandgap solids. *IEEE J. Quantum Elect.*, 32 (8):1324–1333, 1996.

[154] E. Fazio, A. Belardini, M. Alonzo, M. Centini, M. Chauvet, F. Devaux, and M. Scalora. Observation of photorefractive simultons in lithium niobate. *Opt. Express. Accepted for pubblication*, 2010.

[155] M. Zitelli, E. Fazio, and M. Bertolotti. An all optical nor gate based on the interaction between cosine-shaped input beams of orthogonal polarization. *J. Opt. Soc. Am. B*, 16:214–218, 1999.

[156] M. Bertolotti, A. D'Andrea, E. Fazio, M. Zitelli, A. Carrera, G. Chiaretti, and N. G. Sanvito. Experimental observation of spatial soliton dragging in a planar glass waveguide. *Optics Commun.*, 168:399–403, 1999.

[157] E. Fazio, M. Zitelli, M. Bertolotti, A. Carrera, G. Chiaretti, and N. G. Sanvito. Solitonic waveguiding in planar glass structures. *Optics Commun.*, 158:331–336, 2000.

[158] F. Garcia, E. Fazio, and M. Bertolotti. Optical multifunction logic gate based on bso photorefractive crystal. *SPIE*, 4987:310–319, 2003.

[159] L. B. Ceipidor, A. Bosco, and E. Fazio. Logic functions, devices and circuits based on parametric nonlinear processes. *J. Lightwave Technol.*, 4987:310–319, 2008.

[160] T. Tanemura, M. Takenaka, A. Al Amin, K. Takeda, T. Shioda, M. Sugiyama, and Y. Nakano. Inp-InGaAsP integrated 1x5 optical switch using arrayed phase shifters. *IEEE Photonic Tech. Lett.*, 20:1063–1065, 2008.

[161] I. M. Soganci, T. Tanemura, K. A. Williams, N. Calabretta, T. de Vries, E. Smalbrugge, M. K. Smit, H. J. S. Dorren, and Y. Nakano. Test. *ECOC 2009 20-24 September Vienna - Austria*, 2009.

[162] J. Söchtig, H. Schütz, R. Widmer, R. Corsini, D. Hiller, C. Carmannini, G. Consonni, S. Bosso, and L. Gobbi. Monolithically integrated DBR waveguide laser and intensity modulator in erbium doped $LiNbO_3$. *Electron. Lett.*, 32:899–900, 1996.

[163] M. L. Masanovic, V. Lal, J. S. Barton, E. J. Skogen, L. A. Coldren, and D. J: Blumenthal. Monolithically integrated Mach-Zehnder interferometer wavelength converter and widely tunable laser in InP. *IEEE Photonic Tech. Lett.*, 15:1117–1119, 2003.

[164] K. J. Bachmann, E. Buehler, J. L. Shay, and A. R. Strnad. Liquid encapsulated Czochralski pulling of InP crystals. *J. Electron. Mater.*, 4:389–406, 1975.

[165] S. Kitazaki, M. J. Griffin, R. Fornari, E. Giglioli, A. Sentiri, A. Zappettini, G. Mignoni, and G. Zuccalli. Growth of semi-insulating InP with uniform axial Fe doping by a double-crucible LEC technique. *J. Cryst. Growth*, 179:57–66, 1997.

[166] T. Inada, T. Fujii, M. Eguchi, and T. Fukuda. Technique for the direct synthesis and grown of indium phosphide by the liquid phosphorus encapsulated Czochralski method. *Appl. Phys. Lett.*, 50:86–89, 1987.

[167] S. M. Sze. *Physics of semiconductor devices*. Wiley Int. Science, 1981.

[168] G. C. Valley. Simultaneous electron-hole transport in photorefractive materials. *J. Appl. Phys.*, 59:3363–3366, 1986.

[169] G. Picoli, P. Gravey, C. Özkul, and V. Vieux. Theory of two-wave mixing gain enhancement in photorefractive InP:Fe: A new mechanism of resonance. *J. Appl. Phys.*, 66:3798–3813, 1989.

[170] C. Özkul, S. Jamet, and V. Dupray. Dependence on temperature of two-wave-mixing in InP:Fe at three different wavelengths: an extended two-defect model. *J. Opt. Soc. B*, 14:2895–2903, 1997.

[171] L. Pavesi, F. Piazza, A. Rudra, J. F. Carlin, and M. Ilegems. Temperature dependence of the InP bandgap from a photoluminescence study. *Phys. Rev. B*, 44:9052–9055, 1991.

[172] D. C. Look. Model for Fe^{2+} intracenter-induced photoconductivity in InP:Fe. *Phys. Rev. B*, 20:4160–4166, 1979.

[173] G. C. Valley, S. W. McCahon, and M. B. Klein. Photorefractive measurement of photoionization and recombination cross sections in InP:Fe. *J. Appl. Phys.*, 64:6684–6689, 1988.

[174] F. P. Strohkendl, J. M. C. Jonathan, and R. W. Hellwarth. Hole-electron competition in photorefractive gratings. *Opt. Lett.*, 11:312–314, 1986.

[175] M. C. Bashaw, T. P. Ma, and R. C. Barker. Comparison of single- and two-species models of electron-hole transport in photorefractive media. *J. Opt. Soc. Am. B*, 9:1666–1672, 1992.

[176] G. Picoli, P. Gravey, and C. Özkul. Model for resonant intensity dependence of photorefractive two-wave mixing in InP:Fe. *Opt. Lett.*, 14:1362–1364, 1989.

[177] C. Özkul, S. Jamet, P. Gravey, K. Turki, and G. Bremond. Photorefractive effect in InP:Fe dominated by holes at room temperature: influence of the indirect transitions. *J. Opt. Soc. B*, 11:1668–1673, 1994.

[178] G. Bremond, A. Nouailhat, G. Guillot, and B. Cockayne. Deep level spectroscopy in InP:Fe. *Electron. Lett.*, 17:55–56, 1981.

[179] C. Özkul, G. Picoli, P. Gravey, and N. Wolffer. High gain coherent amplification in thermally stabilized InP:Fe crystals under dc fields. *Appl. Optics*, 29:2711–2717, 1990.

[180] R.S. Rana, D. D. Nolte, R. Steldt, and E. M. Monberg. Temperature dependence of the photorefractive effect in InP:Fe: role of multiple defects. *J. Opt. Soc. Am. B*, 9:1614–1625, 1992.

[181] P. Delaye, P. U. Halter, and G. Roosen. Thermally induced hole-electron competition in photorefractive InP:Fe due to the Fe^{2+} exited state. *Appl. Phys. Lett.*, 57:360–362, 1990.

[182] F. Devaux and M. Chauvet. Three-dimensional numerical model of the dynamics of photorefractive beam self-focusing in InP:Fe. *Phys. Rev. A*, 79:033823 1–7, 2009.

[183] N. Fressengeas, N. Khelfaoui, C. Dan, D. Wolfersberger, H. Leblond, and M. Chauvet. Roles of resonance and dark irradiance for infrared photorefractive self-focusing and solitons in bi-polar InP:Fe. *Phys. Rev. A*, 75:063834 1–6, 2007.

[184] M. Chauvet, S. A. Hawkins, G. J. Salamo, M. Segev, D. F. Bliss, and G. Bryant. Self-trapping of planar optical beams by use of the photorefractive effect in InP:Fe. *Opt. Lett.*, 21:1333–1335, 1996.

[185] H. Meng, G. Salamo, M. Shih, and M. Segev. Coherent collisions of photorefractive solitons. *Opt. Lett.*, 22:448–450, 1997.

[186] W. Krolikowski, C. Denz, A. Stepken, M. Saffman, and B. L.-Davies. Interactions of spatial photorefractive solitons. *Quantum Semiclass. Opt.*, 10:823–837, 1998.

[187] W. Krolikowski, B. L.-Davies, C. Denz, and T. Tschudi. Annihilation of photorefractive solitons. *Opt. Lett.*, 23:97–99, 1998.

[188] A. V. Mamaev, M. Saffman, and A. A. Zozulya. Phase-dependent collisions of (2+1)-dimensional spatial solitons. *J. Opt. Soc. Am. B*, 15:2079–2082, 1998.

[189] E. DelRe, S. Trillo, and A. J. Agranat. Collisions and inhomogeneous forces between solitons of different dimensionality. *Opt. Lett.*, 25:560–562, 2000.

[190] A. Stepken, M. R. belic, F. Kaiser, W. Krolikowski, and B. Luther-Davies. Three dimensional trajectories of interacting incoherent photorefractive solitons. *Phys. Rev. Lett.*, 82:540–543, 1999.

[191] C. Denz, W. Krolikowski, J. Petter, C. Weilnau, T. Tschudi, M. R. Belic, F. Kaiser, and A. Stepken. Dynamics of formation and interaction of photorefractive screening solitons. *Phys. Rev. E*, 60:6222–6225, 1999.

[192] A. Stepken, F. Kaiser, and M. R. Belic. Anisotropic interaction of three-dimensional spatial screening solitons. *J. Opt. Soc. Am. B*, 17:68–77, 2000.

[193] J. S. Aitchison, A. M. Weiner, Y. Silberberg, D.E. Leaird, M. K. Oliver, J. L. Jeckel, and P. W. E. Smith. Experimental observation of spatial soliton interactions. *Opt. Lett.*, 16:15–17, 1991.

[194] C. Rotschild, B. Alfassi, O. Cohen, and M. Segev. Long-range interactions between optical solitons. *Nature Physics*, 2:769–774, 2006.

[195] D. J. Mitchell, A. W. Snyder, and L. Poladian. Interacting self-guided beams viewed as particles: Lorentz force derivation. *Phys. Rev. Lett.*, 77:271–273, 1996.

[196] M. R. Belić, A. Stepken, and F. Kaiser. Spatial screening solitons as particles. *Phys. Rev. Lett.*, 84:83–86, 2000.

[197] L. Poladian, A. W. Snyder, and D. J. Mitchell. Spiralling spatial solitons. *Opt. Commun.*, 85:59–62, 1991.

[198] H. Leblond and N. Fressengeas. Theory of photorefractive resonance for localized beams in two-carrier photorefractive systems. *Phys. Rev. A*, 80:033837 1–6, 2009.

[199] M. Alonzo, C. Dan, D. Wolfersberger, and E. Fazio. Coherent collisions of infrared self-trapped beams in photorefractive InP:Fe. *Appl. Phys. Lett.*, 96:121111 1–3, 2010.

[200] E. Fazio, A. Passaseo, M. Alonzo, A. Belardini, C. Sibilia, M. C. Larciprete, and M. Bertolotti. Measurement of pure Kerr nonlinearity in GaN thin films at 800nm by means of eclipsing Z-scan experiments. *J. Opt. A: Pure Appl. Opt.*, 9:L3–L4, 2007.

[201] M. C. Larciprete, R. Ostuni, A. Belardini, M. Alonzo, G. Leahu, E. Fazio, C. Sibilia, and M. Bertolotti. Nonlinear optical absorption of zinc-phthalocyanines in polymeric matrix. *Photonic Nanostruct.*, 5:73–78, 2007.

Candidate publication list

Book chapters:

- E. Fazio, M. Chauvet, V. I. Vlad, A. Petris, F. Pettazzi, V. Coda, M. Alonzo. Ferroelectric crystals for photonics applications: Including nanoscale fabrication and characterization techniques. Chapter: Integrated optical microcircuits in lithium niobate written by spatial solitons. Pag:101-134. *Springer-Material science* 2009

Publication list:

- M. Alonzo, C. Dan, D. Wolfersberger and E. Fazio. Coherent collisions of infrared self-trapped beams in photorefractive InP:Fe. *Appl. Phys. Lett.*, 96:121111 1-3,2010.

- E. Fazio, A. Belardini, M. Alonzo, M. Centini, M. Chauvet, F. Devaux and M. Scalora. Observation of photorefractive simultons in lithium niobate. *Opt. Express*, Accepted for pubblication, 2010.

- E. Fazio, M. Alonzo, F. Devaux, A. Toncelli, N. Argiolas, M. Bazzan, C. Sada and M. Chauvet. Luminescence-induced photorefractive spatial solitons. *Appl. Phys. Lett.*,96:091107 1-3,2010.

- M. Alonzo, F. Pettazzi, M. Bazzan, N. Argiolas, M. V. Ciampolillo, S. Heidari Batheni, C. Sada, D. Wolfersberger, A. Petris, V. I. Vlad and E. Fazio. Self-confined beams in erbium-doped lithium niobate. *J. Opt.*,12:015206 1-6, 2010.

- A. Petris, S. Heidari Batheni, V. I. Vlad, M. Alonzo, F. Pettazzi, N. Argiolas, M. Bazzan, C. Sada, D. Wolfersberger and E. Fazio. The r_{33} electro-optic coefficient of Er : $LiNbO_3$. *J. Opt.*,12:015205 1-5, 2010.

- E. Fazio, F. Pettazzi, M. Centini, M. Chauvet, A. Belardini, M. Alonzo, C. Sibilia, M. Bertolotti and M. Scalora. Complete spatial and temporal locking in phase-mismatched second-harmonic generation. *Opt. Express*, 17:3141-3147, 2009.

- J. Safioui, M. Chauvet, F. Devaux, V. Coda, F. Pettazzi, M. Alonzo, and E. Fazio. Polarization and configuration dependence of beam self-focusing in photorefractive $LiNbO_3$. *J. Opt. Soc. Am. B*, 26:487-492, 2009.

- F. Pettazzi, M. Alonzo, M. Centini, A. Petris, V. I. Vlad, M. Chauvet and E. Fazio. Self-trapping of low-energy infrared femtosecond beams in lithium niobate. *Phys. Rev. A*, 76:063818 1-4, 2007.

- M. C. Larciprete, R. Ostuni, A. Belardini, M. Alonzo, G. Leahu, E. Fazio, C. Sibilia, M. Bertolotti. Nonlinear optical absorption of zinc-phthalocyanines in polymeric matrix. *Photonic Nanostruct.*, 5:73-78, 2007.

- E. Fazio, A. Passaseo, M. Alonzo, A. Belardini, C. Sibilia, M. C. Larciprete and M. Bertolotti. Measurement of pure Kerr nonlinearity in GaN thin films at 800nm by means of eclipsing Z-scan experiments. *J. Opt. A: Pure Appl. Opt.*, 9:L3-L4, 2007.

INSTITUTE OF PHYSICS PUBLISHING JOURNAL OF OPTICS A: PURE AND APPLIED OPTICS
J. Opt. A: Pure Appl. Opt. **9** (2007) L3–L4 doi:10.1088/1464-4258/9/2/L01

RAPID COMMUNICATION

Measurement of pure Kerr nonlinearity in GaN thin films at 800 nm by means of eclipsing Z-scan experiments

E Fazio[1], A Passaseo[2], M Alonzo[1], A Belardini[1], C Sibilia[1], M C Larciprete[1] and M Bertolotti[1]

[1] Dipartimento di Energetica, Università La Sapienza and CNISM, Via Scarpa, 16, I-00161 Roma, Italy
[2] National Nanotechnology Laboratory, INFM-Unità di Lecce, c/o Dipartimento di Ingegneria dell'Innovazione, Università di Lecce, Via Arnesano, I-70100 Lecce, Italy

E-mail: eugenio.fazio@uniroma1.it

Received 16 November 2006, accepted for publication 8 December 2006
Published 4 January 2007
Online at stacks.iop.org/JOptA/9/L3

Abstract
We report the measurement of Kerr nonlinearity of thin films of GaN by using the eclipsing Z-scan technique. The measurement was performed using 100 fs pulses at 800 nm. We measured a pure refractive signal, whose associated nonlinear Kerr coefficient was $n_2 = (-7.3 \pm 0.4) \times 10^{-14}$ cm^2 W^{-1}.

Keywords: GaN, thin films, Kerr nonlinearity, Z-scan experiment

In the last few years large bandgap group III-nitride semiconductors have been extensively investigated, due to their transparency over a large range of wavelengths, from the deep-UV to the mid/far-IR [1, 2]; moreover their non-centrosymmetric structure is responsible for a second-order nonlinear optical response ($\chi^{(2)}$) [3, 4], comparable with those of more conventional nonlinear crystals such as KTP or $LiNbO_3$. Thus, the simultaneous combination of transparency and nonlinearity make GaN one of the most interesting candidates for blue-UV light generation. Following such directions recently heterostructures, composed of AlN/GaN multilayer stacks [5] have been proposed to engineer the nonlinear response, taking advantage of field localization due to local resonances. However, such resonances might strongly depend on third-order nonlinear terms that could be excited too. Recently Sun *et al* [6, 7] experimentally analysed TPA and Kerr nonlinearities of GaN in the UV domain by means of Z-scan tests [8, 9], reporting very large nonlinear refraction of the order of 10^{-12} cm^2 W^{-1}. Third-order nonlinearities were also reported at 527 nm by Pacebutas *et al* [10], in terms of both two-photon absorption and refractive index change. From such measurements $n_2 = -(4 \pm 3) \times 10^{-12}$ esu was determined, which corresponds [11] in MKS to $n_2 = -(7 \pm 5) \times 10^{-15}$cm^2 W^{-1}. Both results were strongly affected by absorption [6, 7], being the nonlinear refraction influenced by free carriers too: thus, going below half of the gap (730 nm) this contribution should be avoided, obtaining a purely refractive nonlinearity. In the present paper, we perform eclipsing Z-scan analysis [12] of GaN thin films at 800 nm, in order to escape any two-photon absorption and monitor a pure refractive (Kerr) nonlinearity.

The AlN/GaN structures investigated in this work were grown on (0001) *c*-plane Al_2O_3 substrates in a horizontal low pressure MOCVD system (Aixtron AIX 200-RF), equipped with a rotating substrate holder. Trimethyl gallium (TMGa), trimethyl aluminium (TMAl) and pure ammonia (NH_3) were used as source materials for Ga, Al and N, respectively. Palladium purified hydrogen (H_2) was used as a carrier gas. The investigated AlN/GaN structure represents the elementary cell of a one-dimensional photonic crystal structure [5] designed for pump operation at a wavelength of 480 nm. The designed structure consists of a AlN/GaN couple with a nominal thickness of 76 nm for the AlN layer and 302 nm for the GaN layer. The AlN layer, grown at high temperature on a Al_2O_3 plate, is fundamental for inducing GaN nucleation free of defects at the interface caused by lattice mismatch [13]. The surface morphology of the AlN and GaN layers was examined by atomic force microscope (AFM) measurements.

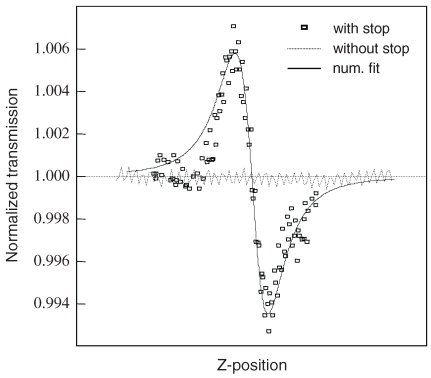

Figure 1. Experimental eclipsing Z-scan data with the numerical fit.

Two families of samples were realized: *reference substrates*, constituted by Al_2O_3 plates with thin AlN layers on top, and *GaN samples*, with GaN films grown on the reference substrates.

The EZ-scan experimental set-up adopted a fast scanning of the samples, at a frequency of about 5 Hz, around the focal point [14] of a laser beam coming from a Ti–sapphire laser, operating either in CW or in passive Kerr-lens mode-locking regime. In this last condition, 5 kW peak power pulses were generated, whose autocorrelation trace gave a time duration on the sample of the order of 100 fs. Four diffraction lengths after the focal point, a circular stop blocked the central part of the laser beam, containing about 65–70% of the total energy. Samples were tilted at about 25°–30° from the orthogonal direction in order to avoid Fabry–Perot-like interference.

First of all we performed EZ-scan measurements in the CW regime (10–40 mW) of reference substrates and GaN samples and no signal was observed, with and without the stop. Thus we conclude that no linear absorption, and consequently thermal nonlinearities, were present. In the mode-locked regime the average power was set exactly as in the CW regime, in order to avoid thermal nonlinearities here too. Nonlinear absorption was checked without the stop and no changes in the transmitted intensity were detected (dotted line in figure 1): as expected, nonlinear absorption at this wavelength is indeed absent. With the stop a change in the transmitted intensity of the order of 0.6% was recorded, as shown in figure 1 (squares). No signal was present in the reference samples. Thus, we concluded the experimental curve was caused by a pure refractive nonlinearity occurring in the GaN film.

The fitting of the experimental data has been performed using the ABCD matrix procedure [15], instead of the usual theory of Z-scan and EZ-scan measurements [7, 8, 16], in order to take into account the complex structure of the sample as well as the nonlinear translation of the sample (sinusoidal in space). Using such a numerical technique, we have fitted the experimental data with the continuous line. The only fitting parameter was the Kerr refractive index n_2:

$$n_2 = -(7.3 \pm 0.4) \times 10^{-14}\ \mathrm{cm}^2\ \mathrm{W}^{-1},$$

whose error was calculated according to the point scattering and samples statistics.

Such a result is one order of magnitude higher than what was obtained by Pacebutas *et al* [10]. Such a difference is mainly correlated to the use of thin films instead of bulk samples, whose field localization enhances the nonlinear response.

In conclusion, we have reported the measurement of the third-order nonlinearities of GaN thin films in the near-IR spectral region. No absorptive nonlinearity (TPA) was observable, while efficient refractive Kerr nonlinearity was recorded with $n_2 = -(7.3 \pm 0.4) \times 10^{-14}\ \mathrm{cm}^2\ \mathrm{W}^{-1}$.

References

[1] Razeghi M and Rogalski A 1996 *J. Appl. Phys.* **79** 7433
[2] Nakamura S, Mukai T and Senoh M 1994 *Appl. Phys. Lett.* **64** 1687
[3] Miragliotta J and Wickenden D K 1996 *Phys. Rev.* B **53** 1388
[4] Passeri D, Larciprete M C, Belardini A, Paoloni S, Passaseo A, Sibilia C and Michelotti F 2004 *Appl. Phys.* B **79** 611
[5] Larciprete M C, Centini M, Belardini A, Sciscione L, Sibilia C, Bertolotti M, Passaseo A, Potì B and Scalora M 2006 *Appl. Phys. Lett.* **89** 131105
[6] Sun C, Huang Y, Liang J, Wang J, Gan K, Kao F, Keller S, Mack M P, Mishra U and Denbaars S P 2000 *Opt. Quantum Electron.* **32** 619
[7] Sun C, Liang J, Wang J, Kao F, Keller S, Mack M P, Mishra U and Denbaars S P 2000 *Appl. Phys. Lett.* **76** 439
[8] Sheik-Bahae M, Said A A and Van Stryland E W 1989 *Opt. Lett.* **14** 955
[9] Sheik-Bahae M, Said A A, Wei T-H, Hagan D J and Van Stryland E W 1990 *IEEE J. Quantum Electron.* **26** 760
[10] Pacebutas V, Stalnionis A, Krotkus A, Suski T, Perlin P and Leszczynski M 2001 *Appl. Phys. Lett.* **78** 4118
[11] Gibbs H M 1985 *Optical Bistability: Controlling Light by Light* (New York: Academic) pp 375–6 appendix I
[12] Xia T, Hagan D J, Sheik-Bahae M and Van Stryland E W 1994 *Opt. Lett.* **19** 317
[13] Potì B, De Vittorio M, Tarantini I, Tagliente M A, Cingolani R and Passaseo A 2007 to be submitted
[14] Fazio E, Bevilacqua P and Bertolotti M 1996 *Proc. SPIE* **2775** 135
[15] Magni V, Cerullo G and DeSilvestri S 1993 *Opt. Commun.* **96** 348
[16] Hughes S, Burzler J M, Spruce G and Wherrett B S 1995 *J. Opt. Soc. Am.* B **12** 1888

Available online at www.sciencedirect.com
ScienceDirect
ELSEVIER
Photonics and Nanostructures – Fundamentals and Applications 5 (2007) 73–78
PHOTONICS AND NANOSTRUCTURES Fundamentals and Applications
www.elsevier.com/locate/photonics

Invited Paper

Nonlinear optical absorption of zinc-phthalocyanines in polymeric matrix

M.C. Larciprete *, R. Ostuni, A. Belardini, M. Alonzo, G. Leahu, E. Fazio, C. Sibilia, M. Bertolotti

Università degli Studi di Roma "La Sapienza", Dipartimento di Energetica, Via Antonio Scarpa 16, 00161 Roma, Italy

Received 30 January 2007; accepted 30 March 2007
Available online 5 April 2007

Abstract

We realized and investigated films of zinc-phtalocyanines into poly(methylmethacrylate) (PMMA) for optical limiting applications. The ratio by weight of the compound to the host polymer was 0.083% and 0.15%. Linear optical characterization of films, performed by spectrophotometry, show a low degree of molecular aggregation of zinc-phtalocyanines in the polymeric matrix.

Two different type of nonlinear optical investigation were performed separately on the obtained films. Measurements of nonlinear transmission were carried out using a ns Nd:Yag laser followed by OPO (532 nm) and a nonlinear response was observed. From the experimental data, the nonlinear absorption coefficient β was retrieved and found to be 29 and 43 cm/GW, respectively. The measurements of β was also performed via the z-scan technique on the same films, using 100 fs pulses at 800 nm. At this wavelength, the nonlinear absorption coefficient was evaluated to be 0.40 and 0.23 cm/GW.

PACS : 78.40.Me; 42.65.−k; 42.70.Jk

Keywords: Nonlinear optics; Molecular photonics

1. Introduction

An optical limiter is an optical device pertaining high transmission up to a certain input intensity while switches to low transmission above this threshold. This behaviour offer sensor and eye protection from laser radiation over a wide range of wavelengths, provided the wide range of existing laser wavelengths. Materials with strong nonlinear optical properties are extensively investigated and generally well suited for the realization of passive optical limiters, i.e. where the switching process between two different transmission regimes is determined only by the intensity of the incoming light. Nevertheless, the ideal material for an optical limiter must meet several specifications as a high optical nonlinearity, a broadband response, a high threshold for laser induced damage and a low intensity threshold to activate the nonlinear process. Finally, the linear absorption must meet a compromise between low value, to reduce losses, and high value to drive the nonlinear effect that provides the limiting action. As a consequence, the realization of an optical limiter with a single bulk material is still an open task.

In the last years, much interest has been devoted to some organic macromolecules, as phthalocyanines (Pc) and their metal complexes (M-Pc), showing nonlinear

* Corresponding author. Tel.: +39 0649916594; fax: +39 0644240183.
E-mail address: mariacristina.larciprete@uniroma1.it (M.C. Larciprete).

1569-4410/$ – see front matter
doi:10.1016/j.photonics.2007.03.002

optical properties of both second [1] and third order [2]. Their strong nonlinear optical properties are related to the system of delocalized π-electrons typical of their macrocyclic core, which gives rise to excited state absorption. Specifically, this accumulative nonlinearity is produced through the polarization of the electronic ground state and the successive absorption, from this polarized state, as determined by the intensity of the applied electric field. The mechanism of nonlinear absorption in these molecules, known as a reverse saturable absorption, can be described by a system possessing four relevant electronic energy levels [3,4].

The Pcs present the further advantage of a great structural flexibility and versatility since they can host different elements in their central site, thus offering a wide range of linear optical properties, related to the central atom nature. Specifically the presence of a heavy central atom, as a metal, has the effect to increase the optical nonlinearities [5].

On the other hand, the main limit to the use of these molecules is their low solubility in common solvents, which give rise to molecular aggregation both in solution and in the solid state, thus causing a drastic decay of their optical properties. In order to overcome the aggregation problem many solutions have been already proposed by introducing appropriate substituents into the cavity of the macrocycle or in the periphery [6], varying axial [7] and peripheral ligands and substituents [8], changing the symmetry of the macrocycle [9].

We introduced zinc-phthalocyanine (Zn-Pc) into a polymeric matrix and characterized the nonlinear optical behaviour of the obtained films. The investigated Zn-Pc has a planar structure, since the central zinc atom does not distort the phthalocyanine ring. Since the planarity of this structure may increase the undesired aggregation effects, in a previous work we characterized the spectral properties of both solutions and films at increasing concentration by a spectroscopic analysis. This preliminary study was crucial for the realization of films with the maximum allowed concentration of Zn-Pc, being the efficiency of the nonlinear absorption process directly proportional to the concentration of the nonlinear molecules. Molecular aggregation, in fact, is evidenced in the linear absorption spectra by a blue-shift and broadening of the Q-Band with respect to that of the monomeric species. For film realization, we entrapped Zn-Pc molecules in a poly(methyl methacrylate) (PMMA) matrix after stirring and heating of many different solutions [13]. Finally, two different types of nonlinear optical measurements were carried out on the realized samples, i.e. nonlinear optical transmission and z-scan, in order to characterize the nonlinear optical absorption coefficient of the films at the investigation wavelengths.

In what follows, we will firstly introduce the process of samples preparation and the corresponding linear optical characterization. Afterwards, we will describe the experimental setups employed for nonlinear optical measurements, together with the obtained results.

2. Sample preparation and linear characterization

The investigated Zn-Pc molecules (Sigma–Aldrich) have no peripheral substitutes and their molecular weight is 577.91 u. Toluene was used as a solvent, and homogeneous solutions of different Zn-Pc concentrations (in the range 1.73×10^{-5} to 2.60×10^{-4} M) were obtained, after stirring for several hours. In order to avoid molecular aggregation we analysed their linear optical properties by evaluating the solutions absorbance spectra in the visible range. Linear optical characterisation was carried out with a standard spectrophotometer, using a wide spectrum light source (QTH 250), and an optical spectral analyser. Transmittance spectra of different solutions in a 1 mm thick quartz cuvette, were carried out and the absorbance spectra were then retrieved, being the reflectance from the quartz cuvette neglectable.

The two absorption bands which are characteristics of these molecules, i.e. the B-band in the UV and the Q-band in the visible range, are evidenced in Fig. 1. In agreement with literature [14], the peak in the Q-band, corresponding to monomer species (680 nm), is slightly shifted to 671 nm. Two other peaks (641 and 606 nm)

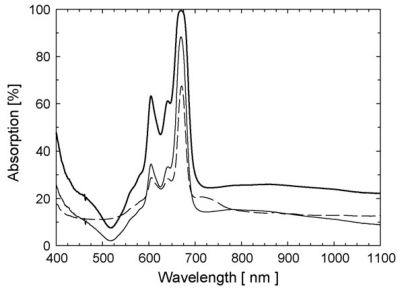

Fig. 1. Comparison between linear optical absorbance spectra of Zn-Pc/toluene solution 2.88×10^{-5} M in a 1 mm thick quartz cuvette (dashed line) and Zn-Pc polymeric films (continuous lines). The Zn-Pc to PMMA weight ratios in the films are 0.15% (thick solid line) and 0.083% (thin solid line).

corresponding to monomer overtones are also visible in the reported spectra. The reduced width of the main peak indicates the homogeneity and good solubility of the investigated solutions.

The solutions with PMMA, ZnPc and toluene were prepared and subsequently heated and stirred for some hours, in order to avoid molecular aggregation. The films were cast into Petri dishes and kept under thermal heating in order to evaporate the residual solvent.

The ratio by weight of the compound to the host polymer was chosen to be between 0.083% and 0.15%, in order to evaluate the relationship between Pc concentration and nonlinear absorption coefficient (β). Films thicknesses were measured with a profilometer and found to be 74 μm for sample A and 57 μm for sample B. The linear absorption spectra of different films are also reported in Fig. 1. The evident Q-band peak, at the same wavelength as for solutions, is an indication of a very low degree of aggregation, corresponding to a great majority of monomeric species entrapped in the polymeric matrix. The presence of the resonances, at the same wavelengths, in the Q-band, underlines the good maintenance of the linear properties of the solutions in the polymer matrix state.

3. Nonlinear optical transmission measurements

The transmission of a laser beam at different intensities through the obtained films, was measured, in order to evidence optical limiting effects in Zn-Pc entrapped into polymeric matrix related to molecule concentration. Linear optical absorption is given by the Beer–Lambert law:

$$\frac{I_{\text{out}}}{I_0} = \exp(-\alpha L) \tag{1}$$

where I_{out} and I_0 are the output and input laser intensities, respectively, α_0 the absorption coefficient (given in cm^{-1}), while L represents the sample thickness. When nonlinear absorption is taken into account, Eq. (1) is modified by including the light induced absorption changes, $\alpha = \alpha_0 + \beta I_0$, where α_0 is now the linear absorption coefficient and β is the nonlinear absorption coefficient (given in cm W^{-1}). For $\beta > 0$, the induced nonlinear absorption results in transmission decreasing with increasing input intensity.

Specifically, under excitation of a laser beam whose wavelength is lower than the Q-band peak, the nonlinear mechanism that takes place in this macromolecules is the so called reverse saturable absorption. This nonlinear absorption is consecutive to the excited triplet state absorption taking place when the laser pulse duration, τ, is longer than the intersystem crossing rate τ_{ISC} [15–17].

In order to measure the optical-limiting responses and then to obtain a β value, we performed the measurements with the experimental setup described elsewhere [18]. The beam was provided by the output of an OPO after a Nd:YAG laser, with a pulse width of 5 ns ($\tau > \tau_{\text{ISC}}$) and a repetition rate of 10 Hz. The selected wavelength was 532 nm, corresponding to the minimum value of nonresonant response for all the samples. After the Variable Attenuator (V.A.), a first beam splitter (BS_1) divided the beam: a part of it (4%) was focused onto a photodiode (Thorlab DET 210) (PD_1) by a lens, and the residual part (96%) was focused onto the sample after passing through a pinhole. The latter beam was sent to a second beam splitter (BS_2): the main part was sent to a beam stopper (BS) while the other part was focused onto a second identical photodiode (PD_2). Both detectors were connected with a 300 MHz digital phosphor oscilloscope while their saturation was prevented using a set of linear neutral density filters, whose transmittance value was taken into account in the data fitting process. An accurate set up calibration was performed by using a power-meter with a Helio-Neon laser as reference.

Both investigated films show a nonlinear response under increasing input intensity and the experimental data are reported in Fig. 2. In particular, at very low input incident intensity the transmission obeys to linear Lambert–Beer law, as evidenced by the lines included in Fig. 2 as an indication of linear sample transmittances. When the input intensity increases, we observed a

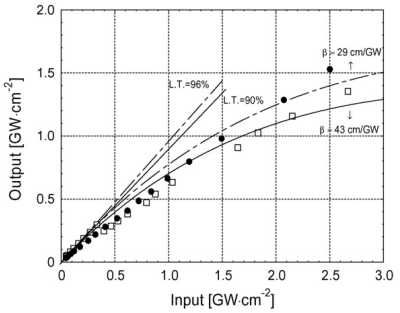

Fig. 2. Nonlinear transmission of film1 (0.15 wt%/□ mark) and film2 (0.083 wt%/● mark) measured for increasing incident intensity. The curve lines represent the best fit of experimental data. The straight lines represents the slopes of the fitting curves, corresponding to the linear transmission of both samples (respectively L.T. = 96%, L.T. = 90%).

Table 1
Films data together with measured linear and nonlinear optical properties, at 532 and 800 nm, respectively

Sample	Zn-Pc ratio in weight (%)	Thickness (μm)	λ = 532 nm			λ = 800 nm		
			Linear transmission (%)	α_0 (cm^{-1})	β (cm/GW)	Linear transmission (%)	α_0 (cm^{-1})	β (cm/GW)
A	0.15	74	90	19.46	43	76	54	0.40
B	0.083	57	96	5.28	29	87	19	0.23

deviation from the linear behaviour, more pronounced for the most concentrated sample. Since the film thickness was known and the linear absorption values could be retrieved from linear spectra, the experimental data were fitted assuming the only parameter to be the nonlinear absorption coefficient, β. From the experimental data, the nonlinear absorption coefficient β was retrieved and found to be 43 and 29 cm/GW for sample A and B, respectively. Sample data, together with the obtained results for β are summarized in Table 1.

4. *z*-Scan measurements

z-Scan [19,20] is a sensitive technique which is essentially a derivative of the input/output intensity measurements previously reported. It is based on the nonlinear transverse modification of the laser beam throughout its focal length, resulting in the intensity variation experienced by a sample which is translated around the focal point of the laser beam. Any optical nonlinearity in the sample would modify the beam profile and, as a consequences, in the far field the modified laser beam would present different spot size, curvature and intensity, determined by the nonlinear refractive and absorptive properties of the tested material. Specifically, when a small aperture is placed in front of the detector, this technique provide a measurement of the refractive nonlinearity while open aperture *z*-scan experiments are sensitive to intensity-dependent absorption, i.e. β coefficient.

The *z*-scan experimental set-up here employed was already described previously [21,22]. The laser source was a Ti–sapphire, in CW regimes, therefore thermal contributions to the nonlinear optical signal could eventually arise. In order to avoid these undesired effects, the sample was scanned around the focal point of a laser beam at a frequency of about 5 Hz and the transmitted signal was directly monitored on a scope. Furthermore, the power beam for all measurements was never exceeding 1 mW in CW. Four diffraction-lengths after the focal point, the laser beam was focused with a long-focal lens on the detector, thus excluding any nonlinearity arising from beam profile variation on the detector. Detector saturation was prevented by an accurate calibration with neutral density filters. Eventual Fabry–Perot like resonances due to multiple interference from film surfaces were avoided by tilting the sample from the orthogonal direction of about 20°, until the low intensity regime gave a completely flat response over the complete sample translation.

The measured transmittance as a function of sample position along the *z*-axis is shown in Figs. 3 and 4 for the

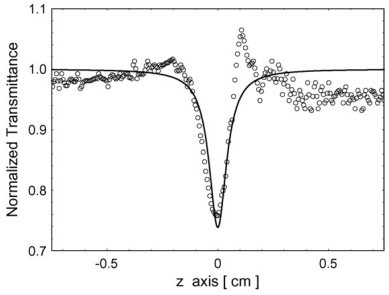

Fig. 3. Open aperture *z*-scan signal of sample A (0.15 wt%): measurements (○) and theoretical fit (solid line).

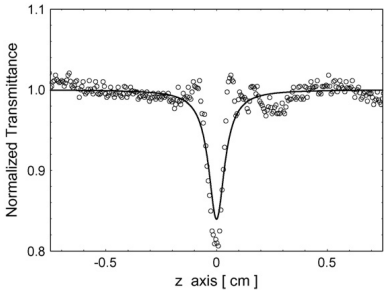

Fig. 4. Open aperture *z*-scan signal of sample B (0.083 wt%): measurements (○) and theoretical fit (solid line).

two samples, respectively. As expected, the effect of nonlinear absorption in the investigated samples is responsible for transmittance decreasing close to the beam focus. Transmittance reduction is more pronounced for sample A which is at the same tine thicker and has a higher weight ratio of nonlinear molecules.

From theoretical point of view, the normalized transmittance as a function of the z-axis coordinate in the open aperture z-scan measurements, can be written as [23]:

$$T(z) = \frac{\ln[1 + q_0(z)]}{q_0(z)} \tag{2}$$

being q_0 the adimensional parameter:

$$q_0(z) = \beta I_0 \frac{1 - e^{-\alpha_0 L}}{(1 + (z/z_0)^2)\alpha_0} \tag{3}$$

L is sample thickness, I_0 the peak beam intensity at the focus, w_0 the beam radio at focus, and z_0 is the Reyleigh length ($z_0 = \pi\omega_0^2/\lambda$). To interpolate the z-scan experimental curves according to Eqs. (2) and (3), the fundamental beam intensity term, I_0, was determined from the measurements of the beam power, 1 mW, and beam spot-size, ∼50 μm. The sample data which are necessary are the sample thickness ($L = 57$ and 74 μm, respectively) and the linear absorption coefficients at 800 nm. With the given data, which for simplicity are also reported in Table 1, the only fitting parameter is then reduced to the nonlinear absorption coefficient, β. We have therefore fitted the experimental data and obtained the solid curves shown in Figs. 3 and 4. The nonlinear parameter were found to be 0.40 cm/GW for sample A and 0.23 cm/W for sample B.

It is worth to note that the nonlinear absorption coefficient values obtained at 800 nm are quite lower, if compared to those obtained at 532 nm. As a matter of fact, the wavelength of investigation, 800 nm, is well above the Q-band. As a consequence the Zn-Pc molecules are not behaving as reverse saturable absorbers, thus the observed nonlinear absorption at the investigated wavelength is determined by a type of two-photon absorption rather than excited triplet state absorption followed by intersystem crossing. Investigation in the range of wavelengths above the Q-band peak will be object of further study, in order to better explain the mechanism of nonlinear absorption here evidenced.

5. Conclusions

Polymeric films containing Zn-Pc were realized by entrapping the molecules in a PMMA matrix by stirring and heating different starting solutions, obtained in toluene. The ratio by weight of the compound to the host polymer was 0.083% and 0.15% and the linear optical measurements of the samples underline the good optical quality of the films with a very low degree of aggregation.

Measurements of nonlinear optical transmittance were recorded at 532 nm in nanosecond regime, and optical limiting effects were observed for both samples. Theoretical fit of the experimental data, i.e. input versus output intensity, was obtained and the nonlinear optical coefficient, β, was calculated to be 29 and 43 cm/GW, respectively for film B and film A.

A second kind of nonlinear measurements via z-scan technique, were performed on same samples, using 100 fs pulses at 800 nm, thus showing transmittance decreasing around the focus, in the open aperture scheme. Following some theoretical considerations, the experimental data were fitted and the value of β at 800 nm was found to be reduced to 0.40 and 0.23 cm/GW, respectively for film A and film B.

In conclusion, the comparison between the nonlinear absorption coefficient of the films below, 532 nm, and above, 800 nm, the Q-band peak is evidence of the different nonlinear optical mechanisms which are activated depending on the spectral region which is investigated. Specifically, for wavelength <670 nm the strong effect of reverse saturable absorption typical of these molecules is active, while the weaker optical nonlinearity in the near infrared is ascribed to two photon absorption mechanism.

Acknowledgements

S. Macrì and G. Gambara are kindly acknowledged for help in chemical measurements and interesting comments. We acknowledge also M. Scalora, M.J. Bloemer and the Charles M. Bowden Research Center, Redstone Arsenal, Alabama, USA for their hospitality and helpful discussion, which are greatly appreciated. This work was supported by EU-NoE Phoremost.

References

[1] T. Yamada, T. Manaka, H. Hoshi, K. Ishikawa, H. Takezoe, J. Porphyrins Phtalocyanines 2 (1998) 133–137.
[2] M. Hanack, D. Dini, M. Barthel, S. Vagin, Chem. Rec. 2 (2002) 129–148.
[3] D. Dini, M. Barthel, M. Hanack, Eur. J. Org. Chem. 2001. 375923769.
[4] M. Calvete, G.Y. Yang, M. Hanack, Synth. Met. 141 (2004) 231–243.
[5] J.W. Perry, K. Mansour, S.R. Marder, K.J. Perry, D. Alvarez Jr., I. Choong, Opt. Lett. 19 (9) (1994) 625–627.

[6] X. Àlvarez Micó, S.I. Vagin, L.R. Subramanian, T. Ziegler, M. Hanack, Eur. J. Org. Chem. (2005) 4328–4337.
[7] H.-J. Kang, E.-H. Kang, S.-W. Park, J.-W. Lee, J.-K. Lee, Macromol. Symp. 235 (2006) 195–200.
[8] G. de la Torre, P. Vàzquez, F. Agullò-Lòpez, T. Torres, Chem. Rev. 104 (2004) 3723–3750.
[9] D. Dini, G.Y. Yang, M. Hanack, J. Chem. Phys. 119 (9) (2003) 4857–4864.
[13] A. Kost, L. Tutt, M.B. Klein, T.K. Dougherty, W.E. Elias, Opt. Lett. 18 (5) (1993) 334–336.
[14] S. Subbiah, R. Mokaya, J. Phys. Chem. B 109 (2005) 5079–5084.
[15] P. Zhu, P. Wang, W. Qiu, Y. Liu, C. Ye, G. Fang, Y. Song, Appl. Phys. Lett. 78 (10) (2001).
[16] Q. Gan, S. Li, F. Morlet-Savary, S. Wang, S. Shen, H. Xu, G. Yang, Opt. Express 13 (14) (2005) 5424–5433.
[17] D. Dini, Int. J. Mol. Sci. 4 (2003) 291–300.
[18] R. Ostuni, M.C. Larciprete, G. Leahu, A. Belardini, C. Sibilia, M. Bertolotti, Optical limiting behavior of zinc phthalocyanines in polymeric matrix, J. Appl. Phys. 101 (2007) 33116–33120.
[19] M. Sheik-Bahae, A.A. Said, E.W. Van Stryland, Opt. Lett. 14 (1989) 955.
[20] M. Sheik-Bahae, A.A. Said, T.-H. Wei, D.J. Hagan, E.W. Van Stryland, IEEE J. Quantum Electron. 26 (1990) 760.
[21] E. Fazio, P. Bevilacqua, M. Bertolotti, Proc. SPIE 2775 (1996) 135–139.
[22] E. Fazio, A. Passaseo, M. Alonzo, A. Belardini, C. Sibilia, M.C. Larciprete, M. Bertolotti, Measurement of pure Kerr nonlinearity in GaN thin films at 800 nm by means of eclipsing *z*-scan experiments, J. Opt. A: Pure Appl. Opt. 9 (2007) L3–L4. , doi:10.1088/1464-4258/9/2/L01.
[23] Chem. Phys. 324 (2006) 699–704.